Doctoral theses at NTNU, 2020:365

Simone Conta

Vibroacoustic analysis of the Woodsol timber frame building concept

Doctoral thesis

NTNU
Norwegian University of Science and Technology
Thesis for the Degree of
Philosophiae Doctor
Faculty of Engineering
Department of Civil and Environmental
Engineering

NTNU
Norwegian University of
Science and Technology

Simone Conta

Vibroacoustic analysis of the Woodsol timber frame building concept

Thesis for the Degree of Philosophiae Doctor

Trondheim, November 2020

Norwegian University of Science and Technology
Faculty of Engineering
Department of Civil and Environmental Engineering

NTNU
Norwegian University of
Science and Technology

NTNU
Norwegian University of Science and Technology

Thesis for the Degree of Philosophiae Doctor

Faculty of Engineering
Department of Civil and Environmental Engineering

ISBN 978-82-326-5076-7 (printed ver.)
ISBN 978-82-326-5077-4 (electronic ver.)
ISSN 1503-8181

Doctoral theses at NTNU, 2020:365

Printed by NTNU Grafisk senter

A Mamma e Papà,
che hanno gettato le fondamenta
perchè tutto ciò fosse possibile.
Ve ne sono infinitamente grato.

Summary

The segment of buildings with four to eight storey is a major share of the building construction market in urban areas. Despite the fact that building with timber has both economical relevance and environmental advantages, the use of timber for urban buildings is still limited to pilot projects. The main reason for this is the limited economical competitiveness of timber buildings due to the risk associated with a lack of knowledge and experience with timber design and construction, compared to the standard concrete and steel buildings. The Woodsol project aims at filling this knowledge gap by developing a timber building concept for urban buildings with a high degree of architectural flexibility. The concept is based on moment resisting timber frames and long-span floor elements. The work presented in this thesis addresses the acoustic aspects and focuses on four main areas of interest: i) the strategy to reliably and accurately determine the acoustic properties of the floor elements, ii) the verification and utilisation of vibration velocity measurement methods to determine the impact sound insulation, iii) the typical properties of the hollow-box floor elements and the influence of the moment resisting connections and iv) possible practical solutions. Low frequency impact sound determines to a large extent occupants' annoyance in lightweight buildings. At the same time, challenges exist in determining accurately the low frequency sound insulation properties of building elements. Therefore, throughout this work, I put a strong focus on the low frequency range.

I adopted a strategy based on experimental activities on prototype floor elements and a full scale system mock-up. I studied the modal behaviour of the floor elements by means of the Experimental Modal Analysis and determined the radiated sound power under impact excitation using the Integral Transform Method (ITM). I performed a parameter study to investigate the effect of the size and of the boundary conditions of the hollow-box floor elements on the modal behaviour and on the sound radiation. I observed a strong dependency of both aspects on the studied parameters at frequencies below 150 Hz. This highlighted some limitations of the standard laboratory measurement procedure according to ISO 10140-2 and ISO 10140-3 in the low frequency range.

The ITM is still a rather new method within building acoustics and therefore part of the activities was aimed at verifying the adequacy of the method for our purposes. I compared the ITM with other vibration velocity measurement methods and with the standard laboratory measurement procedures. I demonstrated the reliability of the ITM and showed how the ITM can overcome the highlighted limitations.
The airborne and impact sound insulation performance of the Woodsol floor element were included in a comparison of the properties of similar objects. The effect of the additional mass in the cavity or on top of the elements was investigated and we determined the effect of different floating floor solutions on top of the hollow-box. This allowed to identify the parameters governing the acoustic performance of this type of elements and their respective relationships.
Within the common flooring solutions in the Norwegian building industry, I identified the practical solutions that can fulfil acoustic requirements according to the Norwegian standard for office, residential and educational buildings, when used with the Woodsol floor elements. More advanced solutions were proposed to meet higher requirements.
Overall, within this work I was able i) to highlight the main parameters governing the acoustic behaviour of the hollow-box floor elements, ii) to identify and validate a measurement method that allows us to accurately measure the radiated sound power under impact excitation *in-situ*, iii) to describe the general airborne and impact sound insulation performance of hollow-box floor elements and iv) to finally suggest practical solutions that might fulfil the acoustic requirements according to the Norwegian standards.

The CVGS mock-up of the Woodsol system (photo credit: SINTEF).

Contents

List of the included papers

Paper #1 Conta, S. and Homb, A., *Experimental modal analysis on Woodsol hollow box floor elements.* Presented at the conference ICSV26, 26th International Conference on Sound and Vibration, Montreal and published in the conference proceedings (2019). *Peer reviewed.*

Paper #2 Conta, S. and Homb, A., *Challenges and limitations using the Integral Transform Method to obtain the impact noise level of timber floors.* Presented at Euronoise 2018, Creta and published in the conference proceedings.

Paper #3 Conta, S., Santoni, A. and Homb, A., *Benchmarking the vibration velocity-based measurement methods to determine the radiated sound power from floor elements under impact excitation.* Published in the journal Applied Acoustics (2020), volume 169, p. 107457.

Paper #4 Conta, S. and Homb, A., *Sound radiation of hollow box timber floors under impact excitation: An experimental parameter study.* Published in the journal Applied Acoustics (2020), volume 161, p. 107190.

Paper #5 Homb, A., Conta, S., Geyer C., Kumer N., *Sound insulation of timber hollow box floors. Collection of laboratory measurement and trend analysis.* Published in the journal Building Acoustics. October 2020. doi:10.1177/1351010X20966157.

Paper #6 Conta, S., Simon, U. and Homb, A., *Structural reverberation time measurements on WOODSOL prototype.* Presented at the ICA 2019, International Congress on Acoustics, Aachen and published in the conference proceedings. *Peer reviewed.*

Declaration of contributions

Paper #1
Conta proposed and wrote the paper. He performed the experimental activities and the analysis. Homb reviewed the experimental setup, the analysis results and the paper suggesting improvements. Conta presented at the conference.

Paper #2
Conta proposed and wrote the paper. He performed the experimental activities and the analysis. Homb reviewed the experimental setup, the analysis results and the paper suggesting improvements. Conta presented at the conference.

Paper #3
Conta proposed and wrote the paper. He performed the experimental activities, the numerical simulations and the analysis presented in the paper. He prepared the Matlab scripts for the Rayleigh Integral Method and the Integral Transform Method. Santoni provided the Matlab script for the Discrete Calculation Method. Santoni and Homb reviewed the paper and suggested improvements.

Paper #4
Conta proposed and wrote the paper. He performed the experimental activities and the analysis. Homb reviewed the experimental setup, the analysis results, the paper and provided feedback.

Paper #5
Homb proposed and wrote the paper. Conta provided the data for the WOODSOL floor element and contributed to the analysis of the data. Conta reviewed and actively contributed to the writing of the paper. Geyer and Kumer provided data and reviewed the paper.

Paper #6
Conta proposed and wrote the paper. Conta performed the experimental activities and the analysis. Homb reviewed the experimental setup, the analysis results, the paper and provided feedback. Simon is the author of the analysis software for the structural reverberation time. Simon provided software and analysis support, reviewed the paper and suggested improvements. Conta presented at the conference.

Publications not included in this thesis

During the work on this PhD thesis, I also contributed to following publications which are not included in this thesis:

Homb, A. and Conta, S., *Strategies to evaluate acoustic properties of timber hollow box floors.* Presented at the conference INTER-NOISE 2019, Madrid and published in the conference proceedings.

Homb, A. and Conta, S., *LYDISOLERING Woodsol dekker til kontorbygg*, WOODSOL Notat 01/19. 2019.

Conta, S. and Homb A., *The WOODSOL project: summary of the acoustic activities and preliminary results*. BNAM2020. Oslo. *This paper was submitted to the conference BNAM2020 scheduled for May 2020 in Oslo. The conference was postponed to 2021 because of the restrictions due to the COVID-19 pandemic.*

Acknowledgements

Despite all the statements that a PhD is fruit of independent research and the fact that a PhD comprises a good amount of solitary work, the whole process would not be possible without the contribution of a surprisingly high amount of people. I would like to name and sincerely thank at least a few of them: *Anders Homb*, my supervisor during this work. His help and guidance were very valuable. He gave me complete freedom but he always promptly prevented me from taking the wrong turns. *Kjell Arne Malo* at NTNU, the project leader. Besides many useful discussion, he taught me a lot about cross country skiing and motivated me to ski even in the most challenging phases of the project. *Petra Rüther* at SINTEF, the package leader for the "WP6 Prototype" which made the mock-up possible. She has been very helpful and supportive in the academic culture integration process. *Sveinung Nesheim* and *Aivars Vilguts*, my fellow PhD students in the Woodsol project. They were involved in the design of the Woodsol mock-up and in the hard construction work. *Leif Joar Lassesen* and the students at Charlottenlund Videregående skole in Trondheim (NO), who greatly supported us during the construction of the mock-up. *Kate Layton Matthews*, who provided language support and numerous great adventures in the nature. *Donal M. Evans*, who supported me with efficient and accurate technical proofreading and good hours around a bonfire, skiing and cycling. Some of the *colleagues at Müller-BBM* tried hard to keep me in Munich. Luckily not hard enough. Some of them reassured and motivated me to take this step and supported me in the process. Thank you all for both. I am grateful to *Aline*, who had the original idea to start this adventure and provided unconditioned support to all aspects of life.

I omitted a lot of you, who helped me along the way: I apologize for that. I am grateful to each of you, but trying to extend this list would only make things worse.

This work has been carried out within the Woodsol project, a project funded by The Research Council Of Norway and the consortium partners (full list available at www.woodsol.no). The project included research at NTNU and SINTEF Community and my PhD grant, which is gratefully acknowledged (15.04.2017 - 10.05.2020).

The assessment committee for this thesis was composed by:
Mohamed Hamdy Ph.D. Assoc. Prof., NTNU, Norway (Administrator).
Prof. Dr. Ulrich Schanda, Rosenheim Technical University of Applied Sciences, Germany (First opponent).
Catherine Guigou-Carter Ph.D., CSTB, France (Second opponent).

Symbols and abbreviations

AutoMAC	Auto-Modal Assurance Criterion
C	Clamped edge (boundary condition)
CVGS	Charlottenlund Videregående Skole
DCM	Discrete Calculation Method
DFT	Discrete Fourier Transform
EMA	Experimental Modal Analysis
F	Free edge (boundary condition)
FE	Finite Element
FRF	Frequency Response Function
FT	Fourier Transform
ITM	Integral Transform Method
JTM	Junction Transmission Measurements
LSFD	Least Squares Frequency Domain method
LVL	Laminate Veneer Lumber
MDOF	Multi-Degree Of Freedom system
MvMIF	Multivariate Mode Indicator Function

PTD	Polyreference Time Domain method
RIM	Rayleigh Integral Method
S	Simply supported edge (boundary condition)
SDOF	Single Degree Of Freedom system

$[\alpha]$	Receptance matrix	m/N
$[K]$	Stiffness matrix	N/m
$[M]$	Mass matrix	Kg
$\alpha(\omega)$	Receptance	s^2/kg
η_r	Structural damping loss factor for mode r	-
γ	Frequency step (ITM)	Hz
$\hat{v}$	Complex vibration velocity	m/s
$\hat{V}_n(k_x, k_y)$	Transformed complex normal vibration velocity	m/s
$\hat{v}_n(r_s)$	Complex normal vibration velocity at the position r_s	m/s
κ	Shear correction factor	-
λ	Eigenvalue (EMA)	-
λ	Wavelength	m
λ_L	Wavelenght of the longitudinal waves	m
λ_p	Dimensionless parameter	-
ν	Poisson's ratio	-
Ω	Surface	m^2
ω	Angular frequency	rad/s
ω_r	Natural frequency of mode r	rad/s
ρ	Density	kg/m^3
ρ_0	Density of air	kg/m^3

ρ_l	Mass per unit length	kg/m
σ	Standard deviation	-
σ_p	Dimensionless parameter	-
$\tilde{y}_p(x)$	Mode shape for a beam	m
$\tilde{z}_{pq}(x)$	Mode shape for a plate	m
ζ	Damping ratio	%
$\{\phi\}_r$	Mass-normalised mode shape vector for mode r	-
$\{\psi\}_r$	Mode shape vector for mode r	-
A	Acceleration (amplitude)	m/s^2
$A(\omega)$	Accelerance	1/kg
a, b	Plate dimensions	m
A_{jkr}	Residue	-
B_b	Bending stiffness for a beam	Nm^2
B_p	Bending stiffness per unit width for a plate	Nm
c	Damping	-
c_0	Speed of sound in air	m/s
$c_{B,b}$	Phase velociy of bending waves in beams	m/s
$c_{B,eff}$	Phase velociy of effective bending waves in plates	m/s
$c_{B,p}$	Phase velociy of bending waves in plates	m/s
$c_{L,b}$	Phase velociy of quasi-longitudinal waves in beams	m/s
$c_{L,p}$	Phase velociy of quasi-longitudinal waves in plates	m/s
c_T	Phase velociy of transversal shear waves	m/s
E	Young's modulus	N/m^2
F	Force (amplitude)	N
f	Frequency	Hz

$f(t)$	Time varying excitation force	N
F_r	Reaction force of the fluid medium on the moving source	N
f_s	Cross-over frequency between thin and thick plates (bending waves)	Hz
G	Shear modulus	N/m^2
h	Thickness of the plate	m
I	Area moment of inertia	m^4
I	Sound intensity	W/m^2
j	Imaginary unit $j = \sqrt{-1}$	-
k	Stiffness	N/m
k	Wavenumber	rad/m
k_0	Wavenumber for waves in air	rad/m
L	Length	m
L_n	Normalized impact sound pressure level, defined in ISO10140-3	dB
L_w	Radiated sound power level	dB re 10^{-12} W
$L_{n,w}$	Weighted normalized impact sound pressure level, defined in ISO717-2	dB
m	Mass	kg
m'	Mass per unit area	kg/m^2
m_r	Modal mass	-
N	Number of measurement points	-
p	Sound pressure	Pa
$P(k_x, k_y, z)$	Transformed pressure in the wavenumber domain	Pa
p, q, r	Indices	-
Q_r	Modal scaling constant	-

R	Position vector of a point in space	m
r	Distance	m
r_s	Position vector on the surface of a plate	m
RT	Reverberation time	s
S	Surface of the plate	m^2
t	Time	s
V	Displacement (amplitude)	m
V	Velocity (amplitude)	m/s
W	Sound power	W
x	X-coordinate	m
y	Y-coordinate	m
$Y(\omega)$	Mobility	s/Kg
$Y(x,t)$	Total transverse deformation (beam)	m
z	Z-coordinate	m
$Z(x,y,t)$	Total transverse deformation (plate)	m
Z_r	Radiation impedance	Ns/m
z_{pp}	Self radiation impedance for the piston p	Ns/m
z_{pq}	Mutual radiation impedance between piston p and q	Ns/m

Chapter 1

Introduction

1.1 The context

The research work presented in this thesis was entirely carried out within the Woodsol project. Woodsol is a research project funded by the Norwegian Research Council with the main goal to develop industrialized structural solutions, based on rigid wooden frames, for use in urban buildings. The project comprises of several work packages covering the four main subjects: i) Production and assembly of structural system and components, ii) moment resisting frames, iii) flooring systems and iv) acoustics. The work in this thesis relates to the work package acoustics. The main task was to investigate the acoustic properties of the structural solutions and develop acoustic solutions to meet sound insulation requirements for several different purposes, e.g. office, residential and educational.
The framework of the Woodsol project had a strongly applied character with clear goals and tasks to be accomplished within the acoustics work package. Nevertheless it offered the opportunity to investigate at a deeper level selected aspects which should be relevant to the broader acoustic community.
The construction system selected within the Woodsol project set specific acoustic challenges. We had to understand and characterize the acoustic behaviour of the stiff, long-span floor elements. Also the interaction between the columns and the floor elements through the special connecting elements had to be investigated. Furthermore the structure-borne sound transmission across the building elements had to be assessed. Throughout the work, we considered two main aspects: i) the more practical task described by the question "How can we fulfil given sound insulation requirements with the Woodsol building system" and ii) to use this opportunity to produce more general acoustic knowledge and contribute to its progress.

1.2 The Woodsol project

1.2.1 Background, aim and concept

While I am writing this thesis, Norway proudly hosts the tallest timber building in the world: Mjøstårnet in Brumunddal, opened in March 2019. It is an 18-storey, 85.4 m high building with mixed use including a hotel, apartments, offices, a restaurant, a swimming pool and a rooftop terrace. Currently, the Swedish municipality of Skellefteå is building their new cultural centre in timber, Sara Cultural Centre, which is expected to be completed within 2021. It will stand 69 m tall and host a 19-storey hotel on top of a theatre. It will also include a museum, an art gallery and the city library. Despite these pilot projects, the use of timber as a construction material is only common in buildings of up to 5 storeys and is still rather limited in taller buildings. Considering that the 4 - 8 storeys segment is a major share of the building construction market in urban areas, there is a large potential for increasing the use of timber construction.
An increased use of timber in the building sector is desired for both economical and environmental aspects ([1] citing [2, 3]). In the Nordic countries, the main reason for the limited used of timber in urban buildings seems to be that timber structural bearing systems are not economically competitive with concrete or steel buildings. High-rise timber buildings are associated with a higher risk due to the lack of experience working with timber, compared to conventional building systems using concrete and steel ([1] citing[4]). Woodsol aims at filling this gap by developing a well documented structural solution.
Woodsol focuses on urban buildings with 5 - 10 storeys. It aims at a large architectural flexibility to achieve a competitive solution that is attractive for investors, project developers and entrepreneurs. The Woodsol building concept is based on a moment resisting frame with long-span floor elements. Moment resisting frames reduce the need for bracing, thereby reducing the constraints on the building façade. Moreover, floor elements can span longer with the same cross section when installed with a moment resisting connection [5]. Long span floors increase the spacing between the columns reducing the constraints in the building interior and allowing to increase the flexibility in the space layout. Woodsol aims at industrialized production of the building elements. Prefabricated elements will allow for rapid assembly on site, fully exploiting the advantages of timber building technology. In order to facilitate this, the load bearing structure should primarily be based on grids and repetitions, which also allows for a versatile system of any size. The three key elements of the system are i) the floor elements, ii) the connector and iii) the use of threaded rods to install the connectors.

1.2.2 The Woodsol building system

Figure 1.1 gives a general overview of the Woodsol building system and its components: the system features glulam vertical columns, long-span floor elements and moment resisting connections between columns and floor elements.

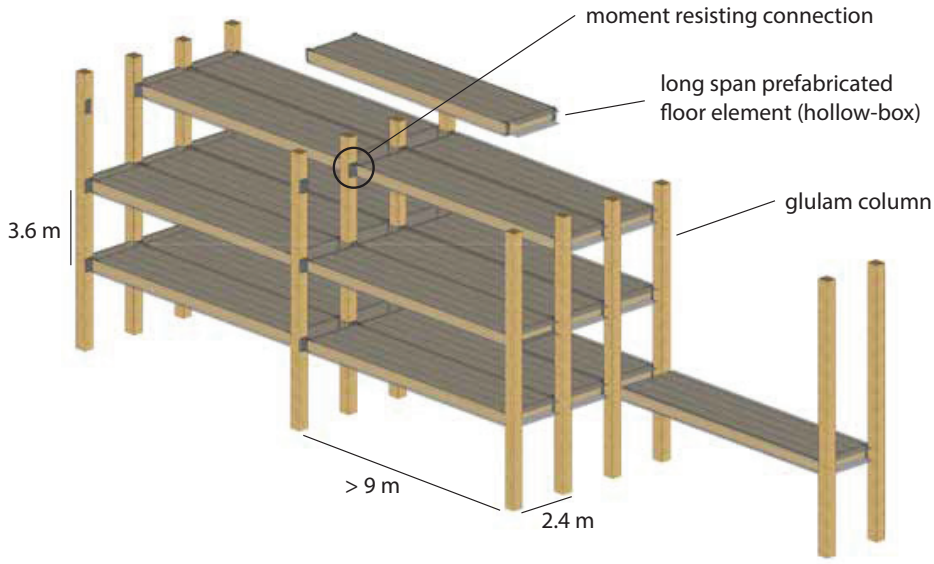

Figure 1.1. Concept of the Woodsol building system (Diagram adapted from SINTEF/ Woodsol material).

In the first phase of the project, different floor solutions were evaluated regarding their adequacy to fulfil the structural and architectural requirements of the Woodsol building system. It was found that stiff floor elements of type hollow-box were best suited [6]. Therefore, further project activities focused on this type of solution. Figure 1.2 shows the current geometry of the floor elements. According to the structural requirements, the height of the cross section is 0.5 m for a span length of about 10 m. The standard width is set to 2.4 m according to transportation requirements.

The top and bottom plates are laminated veneer lumber (LVL). We use KERTO-Q plates from MetsäWood with thickness of 43 mm and 61 mm respectively. The thickness of the bottom flange is designed to be the first fire safety layer. The stringers are glulam. The plates are screwed and glued to the vertical elements to improve the composite effect of the cross section. The weight of the floor element with empty cavity is 1300 kg for an element length of 4.7 m. The cavity filling can be chosen according to the acoustic requirements. In our activities, we used either

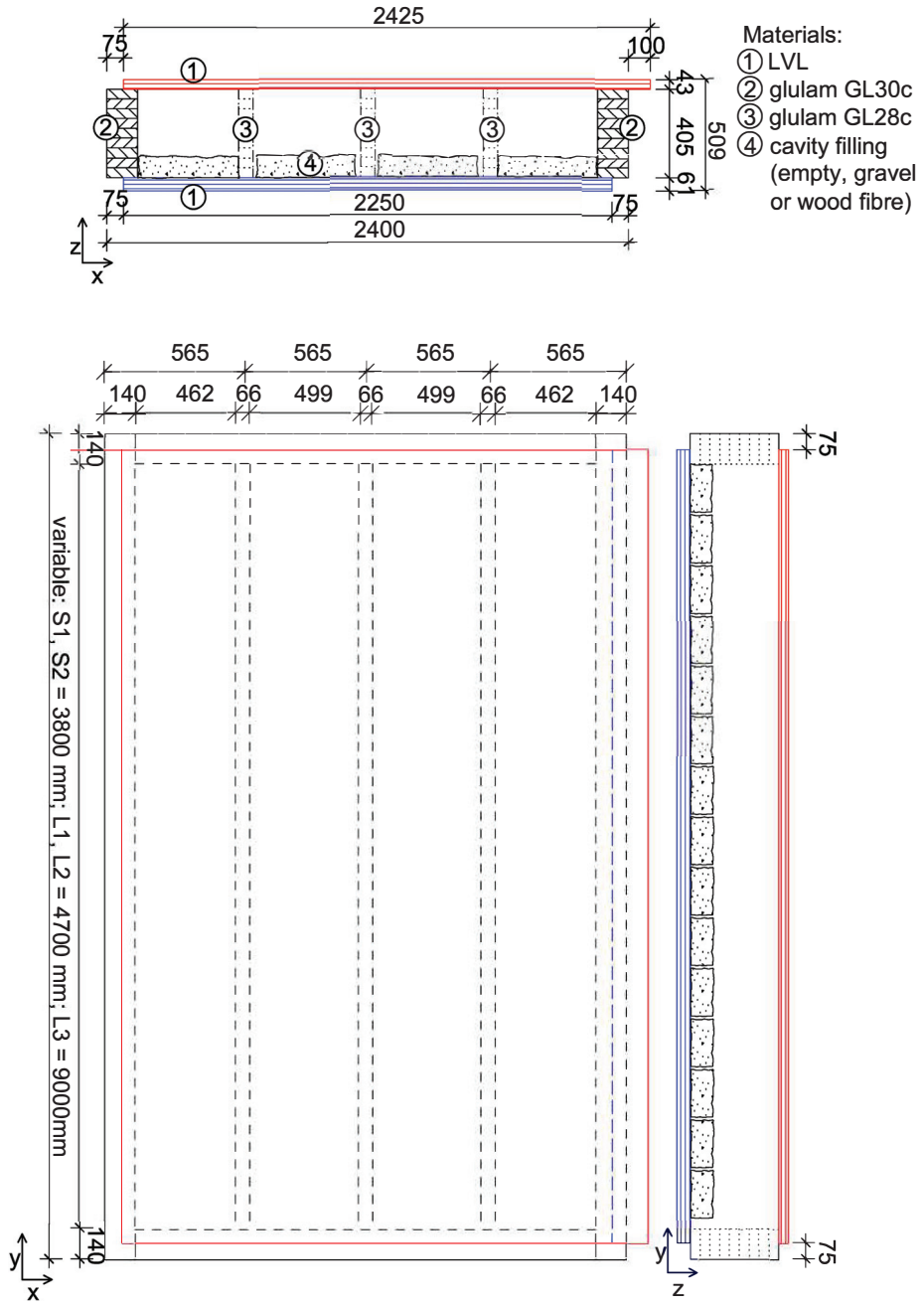

Figure 1.2. Geometry of the Woodsol hollow-box floor element. All dimensions are given in mm. Adapted from [7].

gravel (100 kg/m^2, element total weight: 2600 kg) or wood fibre (13 kg/m^2).
The floor elements are mounted to the columns by means of a special connector at each corner. The connection and the floor elements establish a moment resisting connection between the floor itself and the column [8] with target rotational stiffness 8000 kNm/rad < K_Θ < 13500 kNm/rad [9]. The version of the connector used in our experimental setup is shown in figure 1.3 along with a schematic of the principle. It is based on steel brackets connected by friction bolts.

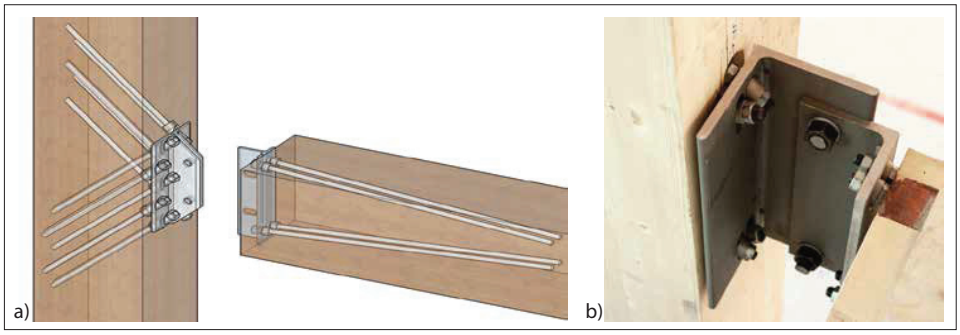

Figure 1.3. a) Woodsol connection concept [9]. b) Picture of the prototype connector used in the CVGS mock-up (Photo: SINTEF).

1.3 Low frequencies and lightweight constructions

The WOODSOL building systems belongs to the lightweight construction category. Lightweight constructions tend to exhibit higher impact sound levels at low frequencies, i.e. below 100 Hz, compared to traditional concrete buildings. This can lead to an increased annoyance of the building's occupants [10, 11]. The traditional building acoustics frequency range of interest includes the 1/3 octave bands from 100 Hz to 3150 Hz and building regulations were defined accordingly. The single value number describing impact sound levels is the weighted normalized impact sound pressure level, $L_{n,w}$ and is defined over the limited frequency range indicated above. Recent research [10–14] shows that $L_{n,w}$ correlates poorly with the perceived sound insulation and explains the observed higher occupants' annoyance in lightweight buildings. To improve this correlation, it is necessary to extend the considered frequency range to lower frequencies, i.e. down to 50 Hz or even 20 Hz and to take into account the correction values to the single value number, e.g. $L_{n,w} + C_{I,50-2500}$ and $L_{n,w} + C_{I,20-2500}$ respectively. Building regulations are being updated accordingly (see the overview of the regulations in some European countries given in *paper #5*).
Unfortunately measuring airborne and impact sound insulation at low frequencies

presents a few challenges. Building acoustic measurements according to standard procedures, e.g. ISO 10140-2 [15] and ISO 10140-3 [16], are based on the assumption of a diffuse sound field both in the sending room, in the case of airborne sound insulation, and in the receiving room. At low frequencies and in relatively small rooms, this assumption is not valid and the measurement uncertainty increases. This is mainly due to the modal character of the sound field, but challenges also arise in the measurement of the reverberation time. Possible strategies to reduce uncertainty and increase repeatability of the measurements include increasing the number of measurement positions and defining more precisely measurement locations, e.g., including the corners. The challenges with the reverberation time are also due to the filter bandwidth and might require performance of the measurements in octave bands instead of 1/3 octave bands [17]. Alternative methods, such as vibration velocity based measurement methods, are not affected by these issues and are valid alternatives to overcome these challenges ([18, 19], see also *paper #3*). However, they are not yet commonly used and are not yet considered by the standards. Sound intensity measurements could also be used, but they pose higher requirements to the sound field in the receiving room [20, 21].
Following the considerations above, all investigations presented in this thesis were performed including the frequencies down to the 20 Hz 1/3 octave band. A large part of the work was dedicated to the Integral Transform Method (ITM), which is one of the vibration velocity based measurement methods and that allowed the measurements to be performed *in-situ* and to obtain accurate data down to the 20 Hz 1/3 octave band (see *paper #3 and #4*).

1.4 The research questions, aims and limitations

Sound transmission in a building involves both direct and flanking sound transmission. Both mechanism have to be addressed considering both airborne and impact sound. At the beginning of this work, I first focused on the modal behaviour of the floor elements and on the direct sound transmission of impact sound at low frequencies. When looking at possible practical solutions, I then included airborne sound and the full building acoustics frequency range. The tasks to be accomplished lead to following questions:

Q1. How to assess modal behaviour and direct sound transmission?
The Woodsol floor elements have standard dimensions of 2.4 m x 9 m and are mounted on a moment resisting frame. However standard transmission suites in acoustic laboratories have a typical opening size of 3 m x 4 m. *Can we characterize the floor elements in a standard acoustic laboratory?*
The experience with lightweight timber buildings shows that impact sound insula-

tion is the most challenging aspect when assessing sound insulation. In addition, we know that the impact sound at low frequencies determines annoyance in lightweight buildings. Large elements might be more prone to produce high sound pressure levels at low frequencies. *Will the size of the element affect the sound radiation properties of the floor elements? How?*
Woodsol uses a clamped connection at the corners to support the floor elements. The boundary conditions affect the dynamic properties of the floor elements. *How will these boundary conditions affect the sound radiation properties?*

Q2. Are vibration-velocity based measurement methods a suitable tool?
To answer the previous question, we need a tool that overcomes the practical limitations of a standard acoustic laboratory and allows using the full size of the element and the correct boundary conditions. Vibration-velocity based measurement methods as the Integral Transform Method (ITM), the Rayleigh Integral Method (RIM) and the Discrete Calculation Method (DCM) are gaining popularity in building acoustics. *Can we exploit these methods to answer the questions of this project? What are the advantages and drawbacks of these methods? What are the similarities and differences between them? Do they perform in a similar way?*

Q3. What are the typical properties of the Woodsol floor elements?
To answer this question, we need to determine the modal behaviour of the floor elements and assess their airborne sound insulation and impact sound levels. We decided to approach this question by means of experimental setups and measurements. Experimental modal analysis was used to determine the modal properties and collect verification data for the numerical models, which were developed in parallel within the project. Vibroacoustic measurements addressed the direct sound transmission and the flanking sound transmission.
The cavity filling of the floor elements can be exploited to improve the acoustic performance of the elements and fulfil given requirements. *Which materials can be used? What is their respective performance?* Additional mass, e.g. gravel, is a traditional solution to improve sound insulation. It is typically used on top of a floor. With hollow-box floor elements, it would be more convenient to use the space in the cavity for this purpose and so reduce the total construction height. *Is this an effective strategy? How does it affect the sound radiation properties?*

Q4. What would a practical solution look like?
The Woodsol project shall deliver verified practical solutions for the Norwegian building industry. *What are the typical floor solutions in Norway that are used to fulfil the Norwegian requirements? Can these solutions also be used with the Woodsol building system? How do they perform? Is there room for improvement?*

Within the scope of this thesis, I had to set flanking sound transmission on a lower priority. However, the experimental activities did include vibration transmission measurements which allow an assessment of the flanking sound transmission. The analysis of the results was left as *further work* (see section 5.2).

1.5 Outline of the work

This thesis is of type ”collection of article” and as such is composed by the introductory part and the included papers. The introductory part comprises of the following chapters: the *Introduction* chapter (1), where I introduce the context of this thesis, present the Woodsol project, provide background information and ask the research questions with the corresponding aim and limitations. The *Methods* chapter (2), where I describe the approach I chose to answer the research questions and present the experimental setups that I used. The *Fundamental theory* chapter (3), where I summarize selected topics of the fundamental theory that was used in the included papers. References to broader literature and detailed theory are provided. The *Summary of the included papers* chapter (4), where I describe the included papers and present the main results. The *Major contributions and further research* chapter (5), where I summarize the major results and delineate the further work.
The included papers are presented in a logical order rather than a chronological one. *Paper #1* presents the basic setup for the experimental modal analysis and preliminary results. *Paper #2, #3, #4* introduce, verify and apply the Integral Transform Method as a tool to measure impact sound insulation. *Paper #5* presents a review of the sound insulation properties of commercially available hollow-box floor elements, including the Woodsol element, and introduces possible practical solutions. *Paper #6* presents the results of structural reverberation times measurements and while completing the characterization of the floor elements, it is the first step towards the determination of flanking sound transmission.
Figure 1.4 presents an overview of the papers, how they relate to the research questions and the reference to the corresponding fundamental theory section in this thesis.

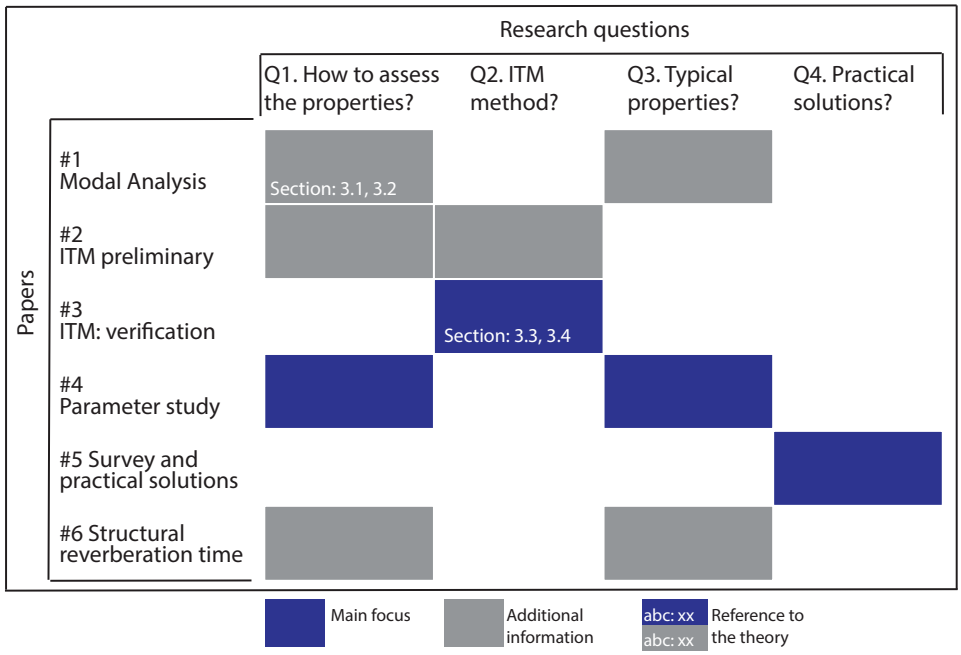

Figure 1.4. Overview of the included papers, the research questions and the corresponding reference to theory section of this thesis.

Chapter 2

Methods

2.1 Strategy

I choose an experimental approach to answer the research questions formulated in section 1.4. There were two main motivations for this choice: the first one was the complexity of the investigated objects. We are dealing with highly inhomogeneous elements built with different orthotropic materials, i.e., a combination of different engineered wood products. The second one was related to the innovative aspects in the structural solution, e.g. the moment resisting frames including metal brackets and threaded rods. These aspects required to build a knowledge base, before reliable numerical models can be developed. The approach was based on three main steps: i) assess the basic vibrational behaviour of the floor elements, ii) investigate how this affects the direct sound transmission and iii) take flanking transmission into consideration [22]. I discuss each step in section 2.1.1, 2.1.2 and 2.1.3, respectively.

2.1.1 Modal behaviour

I investigated the modal behaviour of the floor elements by means of Experimental Modal Analysis (EMA). The details of the method are presented in section 3.2. Two different experimental setups were considered. The first one implemented free-free boundary conditions (see section 2.2.1). The aim was to describe the basic modal properties of the floor elements and to collect data that could be used for the validation of finite element (FE) models. The second one implemented the specific boundary conditions of the Woodsol system (see section 2.2.2). It was aimed at understanding the effect of the boundary conditions on the modal behaviour and, in the next step, on the sound radiation. *Paper #1* and *Paper #4* present in detail the activities and the results obtained within this step.

2.1.2 Direct sound transmission

The investigation of the direct sound transmission through the hollow-box floor elements focused on impact excitation at low frequencies. Experience shows that once the impact sound level has been addressed properly, the airborne sound insulation requirements are mostly fulfilled. In addition, as discussed in section 1.3, low frequency impact sound levels determine to a large extent annoyance in lightweights building and must then be specifically considered.
We wanted to understand how the size of the element and the boundary conditions affect sound radiation. Measurements in a standard sound transmission facility were not suitable because of the fixed, limited size and because of the given boundary conditions. We found an alternative suitable method in the Integral Transform Method (ITM). This is an advanced measurement method that delivers the radiated sound power from a planar object based exclusively on vibration velocity measurements. It comprises of three steps: i) the measurement of the vibration velocity on the sound radiating surface over a dense grid of points, ii) a two-dimensional Fourier transform converting the data in the wavenumber domain and iii) the calculation of the radiated sound power in the wavenumber domain [23, 24]. The measurement method is based on the concept of a plane radiator considered as a sum of plane waves. The related theory is presented in section 3.3. Figure 2.1 presents schematically the measurement setup: the floor element is excited as usual with e.g., a standard tapping machine and the vibration velocity is measured on the bottom surface by means of, e.g., accelerometers.
Investigation of the impact sound level at low frequencies constitutes the core of this thesis. Methods and results were discussed in the three papers: *paper #2* featuring preliminary considerations about the measurement method, *paper #3* featuring detailed analysis and benchmarking of the measurement method with similar methods and *paper #4* featuring a parameter study on the floor elements.

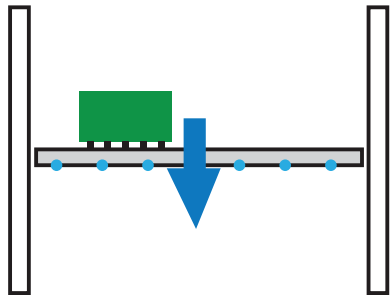

Figure 2.1. Measurement of the impact sound insulation with ITM (concept): excitation by tapping machine (green) and measurement of the vibration velocity on the bottom plate (blue dots).

2.1.3 Flanking sound transmission

In the complete documentation of the building solution, flanking sound transmission needs to be considered. The vibration transmission between floor elements, through the support elements and between floor elements and columns, are two key aspects. They can be assessed by measuring the vibration-level difference across selected junctions, under consideration of the structural reverberation time. Figure 2.2 shows schematically the measurement concept. The CVGS mock-up (see section 2.2.2) was used for this purpose. The vibration transmission was measured as vibration level difference between two elements or between one element and one column under constant excitation. However, the results could not be included in this thesis. The structural reverberation time was used to quantify the losses in the system. The measurement procedure was based on ISO 10848-1 [25]. The structural reverberation time measurements are documented in *paper #6*.

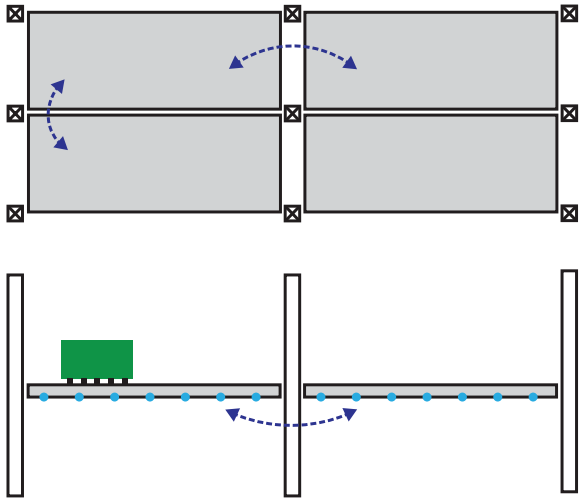

Figure 2.2. Measurement of the flanking sound transmission (concept): excitation by e.g., tapping machine (green) and measurement of the vibration velocity on the bottom plate (blue dots) of two adjacent floor elements.

2.2 Experimental setups

I used several different setups to accomplish the tasks described in the previous sections: the free-free (FF) boundary conditions setup (section 2.2.1), the CVGS mock-up (section 2.2.2) and the transmission suite at SINTEF (section 2.2.3). Across the setups we used the prototype floor elements that were built during the project. The elements were produced in three different lengths: one in full length of 9 m (L3), two in 4.7 m length to fit the space available for the mock-up (L1, L2) and two in 3.8 m length to fit the opening size of the transmission suite at the Sintef laboratory in Oslo (S1, S2). All elements had the same cross section (figure 1.2) for ease of comparison of the data. In table 2.1, I present an overview of the element variants that I investigated and the measurements that I performed. In the table, the measurement setups used are abbreviated respectively with *FF*, *Mock-up* and *Standard*. The abbreviation ISO indicates measurements according to the standards ISO10140-2 [15] and ISO10140-3 [16] .

Table 2.1. Overview of the measurements performed (only direct sound transmission).

Element	Length	Cavity	FF		Mock-up		Standard		
			EMA	ITM	EMA	ITM	EMA	ITM	ISO
L3	9 m	empty	x	x					
L1	4.7 m	empty	x	x	x	x	x		
		gravel	x	x	x	x	x		
S1	3.8 m	empty	x	x	x	x	x	x	x
		gravel	x	x	x	x	x	x	x
		wood fibre							x

2.2.1 Free-free boundary conditions

This setup was designed with the main scope of performing experimental modal analysis on the floor elements and produce the data for the validation of FE models. Free-free boundary conditions are best suited for modal validation because they can easily be implemented in an FE model and uncertainties due to different restraints are avoided.

Free-free boundary conditions are achieved experimentally by suspending the object of interest in a way that the natural frequencies of the rigid body motions are well below the first natural frequency of the object. In our case, the floor element was mounted on four air bellows (Parker removable air bellows – 9109 series, Type 6" x 1). The bellows were installed on top of 0.8 m heigh *lecablocco* pillars filled with concrete to give access to the bottom side of the element (figure 2.3). The

bellows were inflated to a pressure of 6.5 bar. The corresponding height of the air bellows was 95 mm, which according to the data-sheet provides a stiffness of 2.7×10^5 N/m. This lead to a natural frequency of the first rigid body motion between 3 Hz and 5 Hz, which was about four times lower than the first mode of the floor element. The details of the experimental procedure and data analysis are given in *Paper #1* and *Paper #4*.

Figure 2.3. Experimental setup with free-free boundary conditions. a) 9 m floor element on air bellows. b) Detail of the air bellows.

2.2.2 The CVGS mock-up

I leaded the design and construction of the system mock-up which was built by the students of Charlottenlund Videregående Skole (CVGS, project partner) to allow for our experimental investigations. The mock-up was built as the smallest unit of the building system to allow for measurements of both the direct impact sound transmission and the flanking sound transmission through the connectors and the columns. The CVGS students built in total four floor elements for the mock-up (L1, L2, S1, S2) which were used in the different measurement setups. Figure 2.4 shows a picture of the mock-up with two 4.7 m long elements (L1 and L2) mounted side by side on total six columns.

Figure 2.4. Woodsol mock-up at CVGS.

The material for the columns was glulam. The columns had dimensions of 0.40 m x 0.45 m x 5.20 m, which is the size determined by the structural and fire safety requirement for an 8 - 10 storey building. The columns were installed on the floor with a pin connection allowing rotation in the plane of the moment resisting connection. The heads of the columns were connected to each other by aluminium profiles to reduce the free vibrations of the columns. The floors were mounted with the bottom flange at 2 m above the floor of the lab. The column height was designed to have the possibility of mounting the floor elements as a two storey building and investigate the vertical flanking transmission. The details of the experimental procedure and the results are described in *Paper #1* and *#4* for the modal behaviour and the direct sound transmission respectively. The characterization of the elements on the mock-up was completed by the structural reverberation time

measurements described in *Paper #6*. In addition, I performed junction transmission measurements to investigate the flanking transmission on this mock-up but the analysis and presentation of the results is left as *further work* (section 5.2).

2.2.3 Measurement in a standard transmission suite

I performed these measurements in the transmission suite of the SINTEF acoustic laboratory in Oslo with one small element (S1, 3.7 m x 2.4 m x 0.5 m). These measurements had two main purposes. The first was to validate the measurement procedure based on the ITM to determine the impact sound level. The procedure and the results are described in *Paper #3*. The second was to test various practical solutions for the Norwegian market according to ISO10140-2 [15] and ISO10140-3 [16].

The lab opening has dimensions 2.8 m x 3.7 m. The element was installed with the two short edges resting on the lab structure with interposed resilient layer. The two long edges were free. The element was positioned in the middle of the laboratory opening and the remaining area was closed by means of concrete elements. All the spaces between the element and the surrounding construction were filled with mineral wool and sealed with soft modelling clay. The resulting boundary conditions might be seen as close to to simply supported at the two ends. All the measurements and the installation of additional floating floors were performed on the element surface. The area of the element with 8.9 m^2 did not fulfil the standard's requirement of a minimum sample area of 10 m^2. This was due to the fixed width (2.4 m) of the WOODSOL element, determined by the transport requirements of the prefabricated element and it demonstrates an existing challenge when applying the current standards. It is not straightforward to predict the effect of not meeting the size requirement on the measured airborne sound insulation and impact noise level. However, in this case, this is expected to have less influence on the results as compared to changing the geometry of the sample.

The tested solutions were aimed at fulfilling the requirements for different purposes, including office, residential and educational buildings. Figure 2.5 summarizes the tested configurations. We chose to investigate a range of solutions ranging from simple to advanced and including typical Norwegian build-ups. The tested solutions were: bare floor with varying filling inside the cavity (empty, wood fibre, gravel 100 kg/m2), a single layer of vinyl flooring, chipboard on wood fibre plates, plasterboard and chipboard on mineral wool panels and flooring system based on battens and Sylodyn pads. The results are partially presented in *Paper #5*.

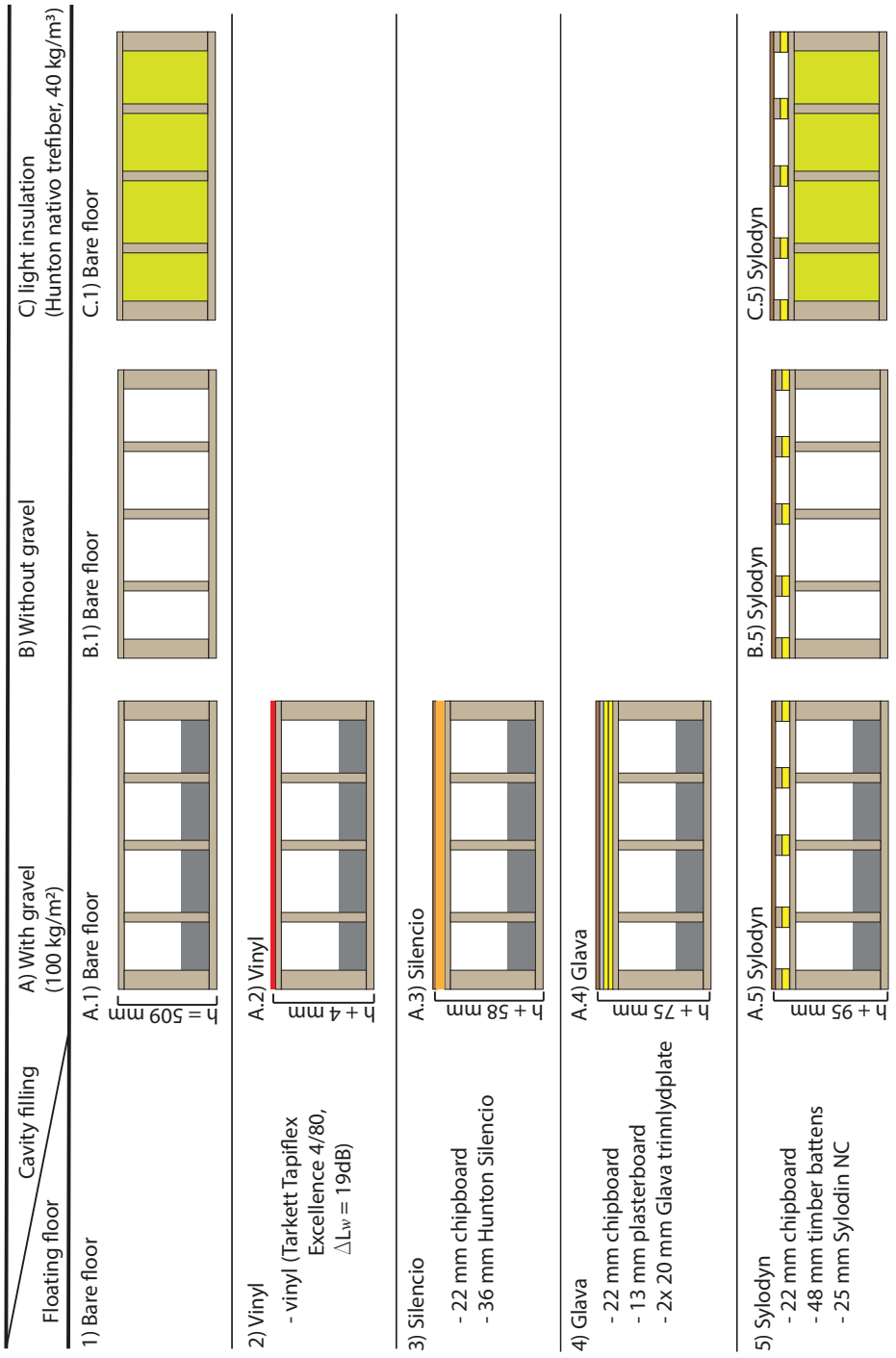

Figure 2.5. Configurations measured in the standard transmission suite.

2.2.4 Excitation sources

Across the experimental setups we used different excitation sources according to the purpose of the measurements. Figure 2.6 show a overview of them.
I used the ISO tapping machine when investigating the direct sound transmission. I was explicitly interested in comparing the floor elements impact sound levels with data from similar objects available in the literature and with standard laboratory measurements. Two types of sources are common to measure the impact sound level: the ISO standard tapping machine (figure 2.6a, to the left) and the ISO rubber ball. In addition, the bang machine exists but its use is limited to Japan and Korea [26]. The tapping machine is the traditional excitation and is the most used excitation both in the laboratory and in the field. It has the advantage of being straightforward to use, high repeatability and has a wide frequency range of excitation. The main drawback is that its excitation spectrum differs strongly from that of real sources, in particular when looking at heavy impacts. In that case, the rubber ball might be more suitable. The rubber ball also offer the advantage of a higher signal at lower frequencies but shows the major drawback of an excitation frequency range limited to around 200 Hz [14, 21, 27]. However, the amount of data available with tapping machine excitation is largely dominant and we therefore decided to use the tapping machine.
Electrodynamic shaker (figure 2.6c) and impact hammer (figure 2.6b) were both used to measure the structural reverberation time. *Paper #6* describes in detail the advantages of each and discuss the challenges related with the two different types of excitations, including the effect of non-linearities.
The shaker and the tapping machine were also used in the junction transmission measurements on the CVGS mock-up.
Finally, I used a semi-dodecahedron (figure 2.6a, to the right) to estimate the airborne excitation on the floor element bottom plate due to the noise radiated by the tapping machine acting on the top plate (details provided in the appendix of *Paper #4*).

Figure 2.6. Excitation sources. a) Tapping machine and semi-dodecahedron. b) Impact hammer with acquisition system. c) Shaker with impedance head.

Chapter 3

Fundamental theory

3.1 Waves and natural vibration modes in beams and plates

3.1.1 Structural waves

In solids, a number of mechanical waves can propagate. In building acoustics, the focus lies on three type of waves: bending waves, which are out-of-plane waves, and two types of in-plane waves, i.e., quasi longitudinal and transverse shear waves. While bending waves dominate the sound radiation, the latter play mainly a role in the structure-borne sound transmission. All three types are needed to fully describe the vibroacoustic behaviour of a structure. Both Hopkins [21] and Cremer [28] provide a detailed survey over the structural waves and their acoustic effects. Following these two references, I will provide here only the most relevant equations for this thesis. I also highlight the PhD thesis of Winter [29] as a reference, which provides a compact overview of the topic with clear illustrations. To keep things tidy, I will presents only the equations for isotropic materials, although this assumption is not valid for timber.

Longitudinal waves propagates in the same direction as the particle motion. When the wavelength of the longitudinal wave is comparable to the dimensions of the structure, then they are referred to as quasi-longitudinal wave. Quasi-longitudinal waves causes longitudinal and lateral strains. However, these lateral strains produce only small displacement, so that they do not contribute significantly to sound radiation, compared to bending waves. The phase velocity for quasi-longitudinal

waves is:

$$\text{for beams} \qquad c_{L,b} = \sqrt{\frac{E}{\rho}} \tag{3.1a}$$

$$\text{for plates} \qquad c_{L,p} = \sqrt{\frac{E}{\rho(1-\nu^2)}} \tag{3.1b}$$

where E is the Young's modulus, ρ is the density of the material and ν is the Poisson's ratio. These relations are non-dispersive and are valid under the assumption that the wavelength of the longitudinal wave λ_L is much greater than the thickness h, i.e., $\lambda_L > 3h$.

Transverse shear waves oscillate perpendicularly to their direction of propagation with motion in the plane tangential to the adjacent air. For this reason, they cannot radiate, nor be excited by, airborne sound, but they are relevant for structure-borne sound transmission. Transverse shear waves are non-dispersive and their phase velocity is given by:

$$c_T = \sqrt{\frac{G}{\rho}} = \sqrt{\frac{E}{2\rho(1+\nu)}} = c_{L,p}\sqrt{\frac{1-\nu}{2}} \tag{3.2}$$

where $G = E/[2(1+\nu)]$ is the shear modulus. Equation 3.2 is valid for plane transversal waves in solids which are large compared to the wavelength in all three dimensions and in plates if the directions of propagation and displacement are parallel to the free surface. If the displacement is perpendicular to the beam axis, or the free surface of the plate, then the phase velocity depends on the dimensions of the cross section and is given by following equation ([29] citing [30]):

$$c_T = \sqrt{\frac{\kappa G}{\rho}} \tag{3.3}$$

where κ is the shear correction factor. For a rectangular cross section κ assumes the value $\kappa = \frac{5}{6}$.

Bending waves oscillate perpendicular to their direction of propagation and cause both rotation and displacement of the material. The displacement towards the surrounding medium is relatively large and thus bending waves play a major role in the sound radiation. To determine their phase velocity, a distinction must be made between thin and thick plates. In [28], a plate is considered thin when the bending wavelength λ_B is much longer than the plate thickness: $\lambda_B > 6h$. Winter [29] introduces a much lower limit, the energetic thin plate limit, corresponding to $f_{limit} = f_s/4$ based on the cross-over frequency f_s:

$$f_s = c_T^2 \frac{1}{2\pi}\sqrt{\frac{m'}{B_p}} \tag{3.4}$$

where m' is the mass per unit area and B_p the bending stiffness per unit width of the plate.
For thin bodies, the bending wave phase velocity is given by:

$$\text{for beams} \qquad c_{B,b} = \sqrt[4]{\frac{B_b \omega^2}{\rho_l}} \tag{3.5a}$$

$$\text{for plates} \qquad c_{B,p} = \sqrt[4]{\frac{B_p \omega^2}{m'}} \tag{3.5b}$$

where B_b is the bending stiffness of the beam, ρ_l is the mass per unit length and $\omega = 2\pi f$ is the angular frequency.
For thick plates, the *effective bending waves* need to be considered. They are a combination of bending waves and transversal shear waves and their phase velocity is given by:

$$c_{B,eff} = \left[\frac{1}{2} \left(\frac{\rho h^3}{12 B_p} + \frac{\rho}{\kappa G} \right) + \frac{1}{2} \sqrt{\left(\frac{\rho h^3}{12 B_p} + \frac{\rho}{\kappa G} \right)^2 + 4 \frac{\rho h}{B_p \omega^2} - 4 \frac{\rho^2 h^3}{12 B_p \kappa G}} \right]^{-\frac{1}{2}} \tag{3.6}$$

As we see from e.g., equation 3.6, the dispersion curves of structural waves are strongly related to the material properties. Several methods exist to determine dispersion curves experimentally, including the ITM method and the Inhomogeneous Wave Correlation method IWC [31, 32]. Santoni shows in [33] how to determine the elastic and stiffness characteristics of a material from flexural wave velocity measurements. Hambric shows in an early chapter of his book a procedure to determine the resonance frequency of a mode based on a wavenumber versus frequency diagram [30]. Using the ITM method, we can have direct access to these kind of diagrams and gain important information about the structure and the material properties (see e.g. *paper #4*).

3.1.2 Flexural modes

The modal description of the vibration field of a structure is very practical, especially at low frequencies. In this section, I will provide the fundamental equations both for beams and plates, with different boundary conditions.
At low frequencies, the floor element considered in this thesis can be conveniently described as a beam, when the focus lie on its modal behaviour (see *p*aper #1 and #4). However, a description in terms of the plate theory becomes necessary when we consider sound radiation.

I will use the following notation for the boundary conditions: C for clamped edge, S for simply supported edge and F for free edge. Considering the floor element as a beam, the most relevant boundary condition for the purpose of the current work are S-S, C-C and F-F. The beams installed on a moment resisting system will experience a condition in between S-S and C-C, controlled by the rotational stiffness of the support. In [5], Malo shows the dependency of the first natural frequency on the rotational stiffness of the end restraint. The equivalent conditions for a plate are S-F-S-F and C-F-C-F. The floor elements could also be additionally supported or clamped in the other directions, then the boundary conditions would be S-S-S-S and C-C-C-C, respectively.
The main equations for an isotropic thin beam as given by [34] are:

$$\text{Total transverse deformation} \qquad Y(x,t) = \sum_{p=1}^{N} A_p \tilde{y}_p(x) \sin(2\pi f_p t + \phi_p) \tag{3.7a}$$

$$\text{Natural frequency} \qquad f_p = \frac{\lambda_p^2}{2\pi L^2} \left(\frac{EI}{\rho_l} \right)^{\frac{1}{2}} \tag{3.7b}$$

where x is the position along the beam and t the time, p is the index of the vibrational mode and N the number of modes considered, A_p is a constant with the units of length, $\tilde{y}_p(x)$ is the mode shape and ϕ_p is the phase. A_p and ϕ_p depend on the excitation. λ_p and σ_p are dimensionless parameters determined by the boundary conditions, L is the length of the beam and I is the area moment of inertia. The corresponding mode shapes are given in table 3.1. Note that, while the mode shape changes between C-C and F-F, the first natural frequency remains equal.

Table 3.1. Mode shapes and λ for an isotropic thin beam [34].

S-S	$\tilde{y}_p(x)$	$\sin \frac{p\pi x}{L}$
	λ_1	π
	σ_1	-
C-C	$\tilde{y}_p(x)$	$\cosh \frac{\lambda_p x}{L} - \cos \frac{\lambda_p x}{L} - \sigma_p \left(\sinh \frac{\lambda_p x}{L} - \sin \frac{\lambda_p x}{L} \right)$
	λ_1	4.73
	σ_1	0.98
F-F	$\tilde{y}_p(x)$	$\cosh \frac{\lambda_p x}{L} + \cos \frac{\lambda_p x}{L} - \sigma_p \left(\sinh \frac{\lambda_p x}{L} + \sin \frac{\lambda_p x}{L} \right)$
	λ_1	4.73
	σ_1	0.98

The corresponding equations for an isotropic thin plate are [34]:

$$\text{Total transverse deformation} \qquad Z(x,y,t) = \sum_p \sum_q A_{pq}\tilde{z}_{pq}\sin(2\pi f_{pq}t + \phi_{pq}) \tag{3.8a}$$

$$\text{Natural frequency} \qquad f_{pq} = \frac{\lambda_{pq}^2}{2\pi a^2}\left(\frac{Eh^3}{12m'(1-\nu^2)}\right)^{\frac{1}{2}} \tag{3.8b}$$

The dimensionless frequency parameter, λ_{pq}, depends on the boundary conditions, the aspect ratio a/b of the plate and, in general, on the Poisson's ratio ν of the plate's material. The only case, where it is possible to provide a simple, close-form solution for the natural frequencies and the mode shapes of a plate is the simply supported case S-S-S-S:

$$\text{Mode shape} \qquad \tilde{z}_{pq}(x,y) = \sin\frac{p\pi x}{a}\sin\frac{q\pi y}{b} \qquad p,q = 1,2,3,... \tag{3.9a}$$

$$\text{Natural frequency} \qquad f_{pq} = \frac{C_{B,p}}{2}\sqrt{\left(\frac{p}{a}\right)^2 + \left(\frac{q}{b}\right)^2} \tag{3.9b}$$

This equation is based on a one-term modal expansion, which is valid in the cases with two opposite sides simply supported and elementary boundary conditions (C, S or F) on the other two sides. The corresponding mode shapes have similar form, but the amplitudes might vary. In the cases where two opposite sides are not simply supported, the one-term modal expansion is not accurate and higher order terms are required. For a F-F-F-F plate, $p = 1$, $q = 3$ and $p = 3$, $q = 1$ following relationships hold:

$$\text{Mode shape} \qquad \tilde{z}_{13}(x,y) = \cos\frac{\pi x}{a}\cos\frac{3\pi y}{b} - \cos\frac{3\pi x}{a}\cos\frac{\pi y}{b} \tag{3.10a}$$

$$\tilde{z}_{31}(x,y) = \cos\frac{3}{\pi x}a\cos\frac{\pi y}{b} + \cos\frac{3\pi x}{a}\cos\frac{\pi y}{b} \tag{3.10b}$$

In general, the exact values of the dimensionless frequency parameter have to be calculated with numerical techniques. Approximate formulas are available but rather lengthy to be reproduced here (see [34] for details). Leissa [35, 36] provides tabulated data for a selection of modes and aspect ratios. For $a/b = 0.4$, $\nu = 0.3$ [36]:

$$\lambda_{13}^2 = 3.4629 \tag{3.11}$$

The indices p and q can be associated with the number of half-waves in the plate in the x and y direction respectively. While it is easy to count the half- waves on a beam, this is not the case for a plate. It might be easier to describe the modes in term of nodal lines, at least for aspect ratios that clearly differ from $a/b = 1$.

For instance, for the case $p = 1$, $q = 3$, the mode on the rectangular plate shows $p - 1 = 0$ nodal lines in x direction and $q - 1 = 2$ in y direction for a rectangular plate. The nodal lines are almost parallel to the plate's edges for large or small aspect ratios and converge to the two diagonals for the case $a/b = 1$. A clear representation of this is given in [37].

3.2 Experimental Modal Analysis

I used EMA as a tool to understand the dynamic behaviour of the floor elements and to provide data to verify the FE models elaborated by the colleagues in the Woodsol project. I relied on the knowledge gained in a course held by A. Brandt at SDU and his MATLAB toolbox *abravibe* [38]. For the sake of completeness, I present in this section the fundamental equations and concepts which are the basis of EMA and highlight a few aspect that complement the results presented in *Paper #1* and *#4*. For further reference, two works are worth mentioning: the book from A. Brandt, which gives a detailed theoretical treatment of the topic of signal analysis with a focus on its experimental applications [39] and the book from D. J. Ewins, which presents the topic of modal testing, with a strong focus on the practical aspects [40].
Before introducing the fundamental equations, it is helpful to have a look at figure 3.1. In the diagram, I present the basic concepts of vibration analysis and show the two different perspectives of the theoretical and the experimental approaches. A dynamic system can be described in terms of i) a *spatial model*, i.e., the equations of motion with the corresponding mass, damping and stiffness information, ii) a *modal model*, i.e., in terms of the eigenvalues (natural frequencies) and the eigenvectors (mode shapes) or iii) a *response model*, i.e., the impulse responses or frequency responses. The theoretical approach starts from the spatial model to eventually calculate the responses of the system. The experimental approach measures the responses to build the models. EMA is a technique that allows to extract the modal model parameters from measured system responses. On the opposite side, FE software builds mass and stiffness matrices to determine a spatial model.

3.2.1 Fundamental equations

Single degree of freedom system
In this brief section, I will omit the treatment of damping for the sake of brevity and clarity, and refer to [39] and [40] for a thorough discussion about the topic. Following [40], I will start from the simplest case: an undamped single degree of freedom system (SDOF), described by a mass m on a spring k. m and k fully

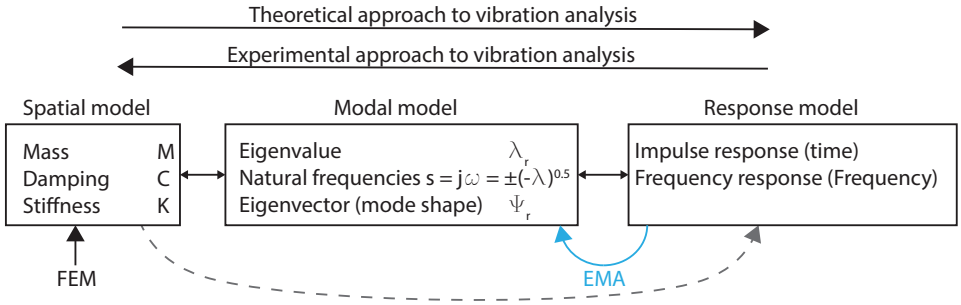

Figure 3.1. Elements in the theoretical and experimental approach to vibration analysis. The role of FE models and EMA is highlighted. Inspired by [40].

determine the *spatial model* of the SDOF system. By writing the equation of motion and looking for its solutions we can obtain the *modal model*. Assuming free vibrations, i.e., exciting force $f(t) = 0$, we can write the equation of motion as:

$$m\ddot{x} + kx = 0 \tag{3.12}$$

where x is the displacement. We are looking for solutions with the form $x(t) = Xe^{j\omega t}$, where X is the amplitude, ω is the angular frequency and t is the time. By substitution, we obtain:

$$k - \omega^2 m = 0 \tag{3.13}$$

This equation has a single solution with a natural frequency $\omega_0 = \sqrt{k/m}$. This solution corresponds to the single mode of vibration of the system and represents our *modal model*.

The next step is to investigate the frequency response. In this case, we have to consider an excitation $f(t) = Fe^{j\omega t}$ and assume a solution of the form $x(t) = Xe^{j\omega t}$. $X = x_0 e^{j\phi_x}$ and $F = f_0 e^{j\phi_f}$ are in this case complex and contain amplitude and phase information. By substitution into 3.12, we obtain:

$$(k - \omega^2 m)Xe^{j\omega t} = Fe^{j\omega t} \tag{3.14}$$

The frequency response function is then:

$$\alpha(\omega) = \frac{X}{F} = \frac{1}{k - \omega^2 m} \tag{3.15}$$

Equation 3.15 shows the response function in the form of a receptance, i.e., the displacement X divided by the force F. Alternatively, the response function can be expressed as mobility, i.e. the velocity $V = v_0 e^{j\phi_v}$ divided by the force F:

$$Y(\omega) = \frac{V}{F} = i\omega\alpha(\omega) \tag{3.16}$$

or as accelerance $A(\omega)$, i.e., the acceleration $A = a_0 e^{j\phi_a}$ divided by the force F:

$$A(\omega) = \frac{A}{F} = -\omega^2 \alpha(\omega) \tag{3.17}$$

In EMA, the form of accelerance is more common while in building acoustics, mobility is mostly used.

Multi-degree of freedom system

The extension from a SDOF system to a multi-degree of freedom system MDOF with N degrees of freedom is relatively straightforward. We rewrite the equation of motion 3.12 in matrix form, this time including the excitation term and using the parentheses to distinguish between scalar, vectors and matrices:

$$[M]\{\ddot{x}(t)\} + [K]\{x(t)\} = \{f(t)\} \tag{3.18}$$

where $[M]$ and $[K]$ are the $N \times N$ mass and stiffness matrices respectively and $\{x(t)\}$ and $\{f(t)\}$ are $N \times 1$ vectors of time-varying displacements and forces.
In the case of free vibrations, the trial solution will be of the form $\{x(t)\} = \{X\}e^{j\omega t}$, where $\{X\}$ is a $N \times 1$ vector of time-independent amplitudes so that $\{\ddot{x}(t)\} = -\omega^2\{X\}e^{j\omega t}$. We are then left to solve:

$$\left([K] - \omega^2[M]\right)\{X\}e^{j\omega t} = 0 \tag{3.19}$$

The ω values corresponding to non-trivial solutions can be found by solving:

$$\det\left|[K] - \omega^2[M]\right| = 0 \tag{3.20}$$

We will obtain N roots, representing the N *natural frequencies* ω_r^2 of the system, with $r = 1, 2, ...N$. By substituting any one of these solutions in 3.18 and letting $\{f(t)\} = 0$, we can solve the equation for $\{X\}$. This will result in a $1 \times N$ set of relative values for $\{X\} = \{\psi\}_r$. $\{\psi\}_r$ is the *mode shape* of the system for the mode r with natural frequencies ω_r^2. A mode shape represents the relative displacement between the masses of the system and is arbitrarily scaled. The complete solution is then expressed by the $N \times N$ diagonal matrix of natural frequencies $[\omega_r^2]$ and the $N \times N$ matrix of the mode shapes $[\psi]$.
We can calculate the frequency response directly from the equation of motion, as we did for the SDOF system, obtaining:

$$\alpha_{jk}(\omega) = \left(\frac{X_j}{F_k}\right)|_{F_q=0, k\neq q} \tag{3.21}$$

where α_{jk} is the $N \times N$ receptance matrix, the subscripts j, k indicates the response and excitation point respectively and the expression $F_q = 0, k \neq q$ states that the force is zero except at the excitation point.

Alternatively, we can use the modal properties to obtain the frequency response. Using the receptance matrix $\alpha(\omega)$, we can rewrite equation 3.18 as:

$$[K] - \omega^2[M] = [\alpha(\omega)]^{-1} \tag{3.22}$$

We pre- and post-multiply both sides of the equation with the mass-normalised mode shape matrix $[\phi]$ and its transpose $[\phi]^T$:

$$[\phi]^T \left([K] - \omega^2[M]\right)[\phi] = [\phi]^T[\alpha(\omega)]^{-1}[\phi] \tag{3.23}$$

Due to the orthogonality properties of the modal model (see [39] or [40] for more details), we obtain:

$$(\omega_r^2 - \omega^2) = [\phi]^T[\alpha(\omega)]^{-1}[\phi] \tag{3.24}$$

or

$$[\alpha(\omega)] = [\phi](\omega_r^2 - \omega^2)^{-1}[\phi]^T \tag{3.25}$$

Equation 3.25 describes the receptance matrix based on the modal properties. It is a symmetric matrix, leading to the reciprocity principle and its implication that:

$$\alpha_{jk} = \frac{X_j}{F_k} = \alpha_{kj} = \frac{X_k}{F_j} \tag{3.26}$$

This shows that switching the excitation and the response point, the transfer function remains unvaried. EMA makes often use of this principle, both in the implementation of the algorithms and in the data verification.
From equation 3.25, we obtain:

$$\alpha_{jk}(\omega) = \sum_{r=1}^{N} \frac{\phi_{jr}\phi_{kr}}{\omega_r^2 - \omega^2} = \sum_{r=1}^{N} \frac{\psi_{jr}\psi_{kr}}{m_r(\omega_r^2 - \omega^2)} = \sum_{r=1}^{N} \frac{A_{jkr}}{\omega_r^2 - \omega^2} \tag{3.27}$$

where we used the modal mass m_r:

$$m_r = \{\psi\}_r^T[M]\{\psi\}_r \tag{3.28}$$

and the residue A_{jkr}:

$$A_{jkr} = Q_r \frac{1}{m_r}\psi_{jr}\psi_{kr} = \frac{1}{m_r}\psi_{jr}\psi_{kr} \tag{3.29}$$

where Q_r is the modal scaling constant for the mode r to be set according to the chosen scheme, e.g. *unity modal mass* or *unity length* (see [39] for the details) and ψ_{jr}, ψ_{kr} the mode shape coefficients for the mode r at the point j and k respectively.
Equation 3.27 is called *modal superposition equation* and it is the foundation of

experimental modal analysis linking the measured frequency response $\alpha_{jk}(\omega)$ to the modal parameters poles and mode shapes, i.e., ω_r^2 and $[\psi]_r$. It also shows that any MDOF system can be described as a sum of SDOF systems.
For further reference, I introduce now the modal superposition equation including the damping factor [40]:

$$\alpha_{jk}(\omega) = \sum_{r=1}^{N} \frac{A_{jkr}}{\omega_r^2 - \omega^2 + j\eta_r\omega_r^2} \tag{3.30}$$

where we introduced the structural damping loss factor η_r of the r^{th} mode . Note that now ω_r is a complex quantity and is linked to the eigenvalues λ_r as $\lambda_r^2 = \omega_r^2(1 + j\eta_r)$. The eigenvectors ψ_r and thus the residues A_{jkr} are also complex quantities.

3.2.2 EMA procedure

In section 3.2.1, I presented the fundamental equations for the modal analysis in their most simple form, i.e., for the undamped case (eq. 3.27) and presented their form for the general case of hysteretic damping (eq. 3.30). Here, we shall see how these equations can be used to obtain the modal parameters from measured frequency response functions FRFs, which is the very task of EMA.
The first step in our basic procedure is to measure the FRFs. One FRF corresponds to α_{jk}. We will see that we have to measure at least one driving point FRF α_{kk} and the transfer FRFs α_{jk} to the other points of interest.
The most basic method to extract ω_r and the damping η_r is the so-called *peak picking* method. It assumes that the full response is completely determined by one single mode and that effects from any other mode can be ignored. It also requires that the structure is lightly damped, so that the peak in the FRF is evident but not too difficult to estimate [40]. The method is applied as follow:

1. Identify the peak in the FRF and read the natural frequency of that mode ω_r.
2. The local maxima of the peak gives the amplitude $|\alpha_{jk}(\omega_r)|$.
3. The damping information can be extracted from the -3dB bandwidth of the peak by using $\eta_r \cong \Delta\omega/\omega_r$.
4. Substituting $|\alpha_{jk}(\omega_r)|$, ω_r, η_r in equation 3.30 and considering only one mode, one can solve for the residue A_{jkr} at $\omega = \omega_r$:

$$A_{jkr} = \frac{\alpha_{jk}(\omega_r)}{\eta_r\omega_r^2} \tag{3.31}$$

5. The mode shape can now be obtained from the measured driving point FRF:

$$A_{kkr} = \psi_{kr}\psi_{kr}, \qquad \psi_{kr} = \sqrt{A_{kkr}} \tag{3.32}$$

where we assumed unity modal mass as scaling. The other points will then be scaled to the driving point by:

$$\psi_{jr} = \frac{A_{jkr}}{\psi_{kr}} \tag{3.33}$$

The practical EMA procedure follows the steps described above, but makes use of more advanced techniques. The collection of available methods and techniques is vast and builds its own discipline, far beyond the scope of this thesis. I shall therefore provide below only an outline of the methods I used.
I used the roving hammer technique to record the impact force at all measurement locations and the acceleration at 7 reference positions. The data was then analysed in a post-processing procedure based on the abravibe toolbox in Matlab [38]. After windowing the input signals, FRFs were calculated and their quality checked examining the coherence and the reciprocity at selected positions. Then, we used the Poly-reference Time Domain Method (PTD) to extract the poles and modal participation factors from the impulse responses calculated from the measured FRFs. This method requires the user to select a set of poles from a stabilization diagram. To guide the choice of the poles, Mode Indicator Functions (MIF) are displayed in the diagram. We used the multivariate MIF, which returns a plot scaled from 0 to 1 and dips at the natural frequencies. The Least Squares Frequency Domain method (LSFD) was used to estimate the mode shapes. The quality of the results was assessed by comparing the measured FRFs with those synthesised with the extracted modal parameters and by means of the Auto-Modal Assurance Criterion (AutoMAC). These methods and several other alternatives are described in detail in [39], [40] and in the technical notes of the abravibe toolbox documentation [38], where further references to the specific literature are provided.

3.3 Sound radiation from plates

In the previous section, we have learned how a structure vibrates and how we can determine experimentally their modal behaviour. In this section, I will present how vibrations and sound radiation are linked. We shall consider the theory of sound radiation from plates under three different perspectives: i) plane radiator as the sum of point sources, ii) plane radiator as the sum of plane waves and iii) radiation impedance of a plane radiator. These three approaches are at the basis of the three measurements methods Rayleigh Integral Methods (RIM), Integral

Transform Method (ITM) and the Discrete Calculation Method (DCM). The ITM was the main tool of the experimental work presented in this thesis. In paper #3, we presented a benchmarking of the three methods when applied to determining the impact sound insulation. I refer to that paper for the numerical implementation of the methods and the discussion of their validity limits.

3.3.1 Plane radiator as the sum of point sources

The description of the baffled plane radiator as the sum of point sources is the concept at the base of the calculation of the sound radiation by the RIM.
The method was described by Lord Rayleigh in his "*The Theory of Sound*" [41] in 1877. The surface S of the radiating plane is divided into small sources of area dS, each having a complex normal surface velocity $\hat{v}_n(r_s)$ and position r_s. If the vibrating plane is baffled, the sound pressure p at a point R and a time t can be calculated with following relation:

$$p(R,t) = j\frac{\rho_o c_0 k_0}{2\pi} \oint_S \frac{\hat{v}_n(r_s) \cdot e^{j(\omega t - k_0 r)})}{r}\, dS \tag{3.34}$$

where ρ_0 is the density of air, c_0 is the speed of sound in air, $k_0 = 2\pi/\lambda_0$ is the wavenumber of the sound waves in air and $r = |R - r_s|$. We can now use equation 3.34 to calculate the sound pressure over a sphere of surface Ω centred around the vibrating surface. Under the approximation of a locally plane wave, we can calculate the sound intensity I:

$$I = \frac{1}{2}\frac{p^2}{\rho_0 c_0} \tag{3.35}$$

Intregating I over the sphere, we obtain the radiated sound power W [42]:

$$W = \oint_\Omega I \cdot n \, d\Omega = \oint_\Omega \frac{\tilde{p}^2}{\rho_0 c_0}\, d\Omega \tag{3.36}$$

where n denotes the unit vector normal to an element of the surface $d\Omega$ and $\tilde{p}$ denotes the root mean square sound pressure.

3.3.2 Plane radiator as the sum of plane waves

An alternative approach describes the vibration field in the baffled plate as the sum of plane waves [28]. This is the approach that builds the basis of the ITM. It is worth noting that these very same equations are also at the base of the generalised acoustic holography and many practical issues are shared between ITM and

acoustic holography [43, 44]. I will summarize the main concepts of this approach following [45].
The main tool that we shall use is the Fourier transform, which in the two dimensional case has the form:

$$F(k_x, k_y) = \int_{-\infty}^{+\infty}\int_{-\infty}^{+\infty} f(x, y)\, e^{j(k_x x + k_y y)}\, dx\, dy \tag{3.37a}$$

$$f(x, y) = \frac{1}{2\pi^2}\int_{-\infty}^{+\infty}\int_{-\infty}^{+\infty} F(k_x, k_y)\, e^{-j(k_x x + k_y y)}\, dk_x\, dk_y \tag{3.37b}$$

where $f(x, y)$ is a generic function defined over the x, y space and $F(k_x, k_y)$ is its transform in the wavenumber domain k_x, k_y. Using this equation we can transform a vibration field from the space domain to the wavenumber domain in a similar manner as we transform signals from the time domain to the frequency domain.
Starting from the Helmholtz equation in air:

$$(\nabla^2 + k_0^2)p(x, y, z) = 0 \tag{3.38}$$

where ∇^2 is the Laplacian operator and $p(x, y, z)$ is the complex pressure in a three-dimensional harmonic sound field, the spatial Fourier transform can be applied to obtain its transformed version ([45] referring to [46]):

$$(k_0^2 - k_x^2 - k_y^2 + \frac{\delta^2}{\delta z^2})P(k_x, k_y, z) = 0 \tag{3.39}$$

where $P(k_x, k_y, z)$ is the transformed pressure in the wavenumber domain. The solution to this equation is a plane wave propagating in the positive z-direction with the wavenumber k_z:

$$P(k_x, k_y, z) = Ae^{-jk_z z} \tag{3.40}$$

with:

$$k_z = \sqrt{k_0^2 - k_x^2 - k_y^2} \tag{3.41}$$

and A is an arbitrary constant. Considering that the plane wave propagates only if k_z is real, this equation provides an important information: the condition $k_x^2 + k_y^2 < k_0^2$ must be fulfilled to have a propagating wave. In the opposite case, the wave will decay exponentially.
The second step in this approach includes transforming the boundary conditions from the spatial to the wavenumber domain. In the case of acoustic radiation from

a plane surface, conservation of momentum requires that the following condition is fulfilled:

$$j\omega\rho_0\hat{v}_n(x,y) + \frac{\delta p(x,y,z)}{\delta z} = 0 \tag{3.42}$$

where $\hat{v}_n(x,y)$ is the complex normal vibration velocity of the surface. Fixing $z = 0$, we can express this condition in the wavenumber domain as:

$$j\omega\rho_0\hat{V}_n(k_x,k_y) + \frac{\delta P(k_x,k_y,z)}{\delta z} = 0 \tag{3.43}$$

where $\hat{V}_n(k_x,k_y)$ is the transformed complex normal vibration velocity in the wavenumber domain. The use of this condition, allows us to determine the constant A by substitution of equation 3.40 in 3.43:

$$A = \frac{\omega\rho_0\hat{V}_n(k_x,k_y)}{k_z} \tag{3.44}$$

We now have an equation that relates the vibration velocity of the plate to the pressure field in the wavenumber domain:

$$P(k_x,k_y,z) = \frac{\omega\rho_0\hat{V}_n(k_x,k_y)}{k_z}e^{-jk_z z} \tag{3.45}$$

and applying an inverse Fourier transformation (eq. 3.37b), we can obtain the complex pressure field:

$$p(x,y,z) = \frac{\omega\rho_0}{2\pi^2}\int_{-\infty}^{\infty}\int_{-\infty}^{\infty}\frac{\hat{V}_n(k_x,k_y)e^{-j(k_x x+k_y y)}}{k_z}e^{jk_z z}\,dk_x\,dk_y \tag{3.46}$$

We have now obtained a description of the sound field based on the sum of plane waves in the vibrating plate. We can use equation 3.46 to calculate the radiated sound power from a baffled planar plate. We start with integrating the acoustic intensity over the plate:

$$\begin{aligned} W &= \iint_S I(x,y)\,dx\,dy = \frac{1}{2}\mathrm{Re}\left[\iint_S p(x,y,0)v^*(x,y)\,dx\,dy\right] \\ &= \frac{1}{2}\mathrm{Re}\left[\int_{-\infty}^{\infty}\int_{-\infty}^{\infty} p(x,y,0)v^*(x,y)\,dx\,dy\right] \end{aligned} \tag{3.47}$$

where the extension of the integration to infinity is possible because outside the vibrating plate the vibration velocity is zero and * denotes the complex conjugate.

By applying Parseval's formula:

$$\int_{-\infty}^{\infty}\int_{-\infty}^{\infty} p(x,y,0)v^*(x,y)\,dx\,dy = \frac{1}{4\pi^2}\int_{-\infty}^{\infty}\int_{-\infty}^{\infty} P(k_x,k_y)\hat{V}_n^*(k_x,k_y)\,dk_x\,dk_y \tag{3.48}$$

and inserting equation 3.45, we can rewrite the equation 3.47 as:

$$W = \frac{\omega\rho_0}{8\pi^2}\mathrm{Re}\left[\int_{-\infty}^{\infty}\int_{-\infty}^{\infty}\frac{|\hat{V}_n^*(k_x,k_y)|^2}{\sqrt{k_0^2-k_x^2-k_y^2}}\,dk_x\,dk_y\right] \tag{3.49}$$

We obtained an expression relating the sound power radiated by a planar baffled plate to the normal vibration velocity of the plate. Analogously to the observation regarding propagating plane waves, we observe here that k_z is only real for:

$$k_0 \geq \sqrt{k_x^2+k_y^2} \tag{3.50}$$

This means that only the wavenumber components within the radiation circle with radius k_0 contribute to the sound radiation.

3.3.3 Radiation impedance of a plane radiator

The DCM relies on the concept of radiation impedance. In this section, we shall recall this concept and and apply it to a baffled radiating piston following the approach of Vigran [42].
The radiation impedance Z_r is defined as the ratio between the reaction force F_r of the fluid medium on the moving source and the source velocity v:

$$Z_r = \frac{Z_r}{v} = R_r + j\cdot X_r \tag{3.51}$$

with R_r and X_r respectively the real part and the imaginary part of the radiation impedance. The relation between the radiation impedance and the power radiated by a source is:

$$W = \frac{1}{2}\mathrm{Re}\{F_r\cdot v^*\} = \tilde{v}^2\cdot R_r \tag{3.52}$$

where $\tilde{v}$ is the RMS value of the vibration velocity.
In the case of a baffled piston, the radiation impedance $Z_{r,piston}$ is (from [42] citing [47]):

$$Z_{r,piston} = \rho_0 c_0 S\left[1-\frac{2J_1(k_0a)}{k_0a}+j\frac{2H_1(k_0a)}{k_0a}\right] \tag{3.53}$$

where J_1 is a Bessel function of order one, H_1 is a Struve function of order one and a is the radius of the piston. Hashimoto in [19] calls this self radiation impedance $Z_{r,piston} = z_{pp}$. Hashimoto uses equation 3.53 to calculate the increment in impedance due to the effect of others pistons on the plate, which he calls mutual radiation impedance z_{pq} . Following [19], the radiated sound power from a baffled planar source can be expressed in terms of the vibration velocities of the p-th element and the corresponding self z_{pp} and mutual radiation impedance z_{pq} by:

$$W = \sum_p W_p = \sum_p \left(\mathrm{Re}(z_{pp})|\tilde{v}_p|^2 + \sum_j \mathrm{Re}(z_{pq}\tilde{v}_p\tilde{v}_q^*) \right) \tag{3.54}$$

Equation 3.54 is the fundamental equation of the DCM.

3.4 The Fourier Transform

The Fourier Transform (FT) is a mathematical tool widely used in many scientific and engineering disciplines. I will refer to [39] for a thorough treatment of the FT and recall here just a few selected topics, which are helpful in the implementation, understanding and usage of the ITM method. We presented the equations for the two dimensional FT already in section 3.3.2, equations 3.37. In the following, I will consider the one dimensional case for the sake of clarity. The extension to the two dimensional case is straightforward.
In my application, I am using the FT on a finite vibration velocity field sampled at discrete locations, i.e. on the measurement grid. It is more common to think of the FT applied to time signals and converting them from the time domain to the frequency domain. Therefore, in table 3.2, I present the correspondence between the key quantities.

Table 3.2. Comparison of the key quantities in the FT transform for the time / frequency and the space / wavenumber case.

Time / Frequency		Space / Wavenumber	
Signal length	T	Object length	L
Frequency resolution	$\Delta f = \frac{1}{T}$	Wavenumber resolution	$\Delta k = \frac{2\pi}{L}$
Sampling interval	Δt	Grid spacing	Δx
Sampling frequency	$f_s = \frac{1}{\Delta t}$	Sampling wavenumber	$k_s = \frac{2\pi}{\Delta x}$
Shannon-Nyquist criterion:			
Maximum frequency	$f_{max} = \frac{f_s}{2}$	Maximum wavenumber	$k_{max} = \frac{k_s}{2} = \frac{\pi}{\Delta x}$

If we now consider the complex vibration velocity field $\hat{v}(x_i)$ measured on a one

dimensional grid of length L at N discrete locations with position x_i, equally spaced with $\Delta x = \frac{L}{N}$, we can write the Fourier transform using its discrete formulation (DFT) as:

$$\hat{v}(k_x) = \frac{1}{N} \sum_{i=1}^{N} \hat{v}(x_i) e^{-ik_x x_i} \tag{3.55}$$

As we know, FT assumes that the measured field is periodic. In our application, we measure the field at discrete positions on a finite grid, implicitly assuming that the field is 0 outside the considered region. This has the effect that a wave with wavenumber k_x, which should appear in the k-space as a Dirac function in the case of infinite extension, appears as a cardinal sine shape in our case considering only a finite region. Next to the peak of the function at k_x, several sides lobes appear. If the resolution is not high enough, the amplitude of the peak can be considerably underestimated since the energy spills over to the side lobes. This effect is known as *leakage*. In our application, the resolution is fixed by the dimensions of the sample. Here, the technique called *zero padding* can be used to increase the resolution: zeros are appended to the measured data, thus artificially increasing the sample size, consequently increasing resolution and reducing leakage.
Leakage is particularly relevant for our application, specially when the wavenumber for the bending waves is larger than the radiation circle and the radiated sound power is entirely determined by the amplitude of the side lobes. Figure 3.2 visualize this concept. It presents the wavenumber spectrum calculated for a one dimensional vibration velocity field with only one wave with $k = 1$ rad/m. The sample has $L = 4.7$ m and the grid spacing is $\Delta x = 0.3$ m. The spectrum is presented in the double-sided form as it is usual in the related literature. Four curves are presented in the diagram: the one calculated with the original resolution $\Delta k = \frac{2\pi}{L}$ and three curves calculated with increasing resolution by adopting zero padding, i.e. $z_p = 2$ padding the measured signal with zeros so to achieve a double signal length and hence $\Delta k = \frac{2\pi}{2 \cdot L}$, $z_p = 5$ providing $\Delta k = \frac{2\pi}{5 \cdot L}$ and $z_p = 10$ providing $\Delta k = \frac{2\pi}{10 \cdot L}$respectively. We see that the amplitudes of the main peaks and of the side lobes is estimated with increasing accuracy. However, we observe almost no difference between $z_p = 5$ and $z_p = 10$, indicating that the achieved resolution is sufficient to describe the features of this particular spectrum. The side lobes, that we see now, are due to the finite size of the sample and are a physical effect and not just an effect of the truncation of the signal as we would expect in the common FT of time signals. Further increasing the resolution will not reduce the side lobes.

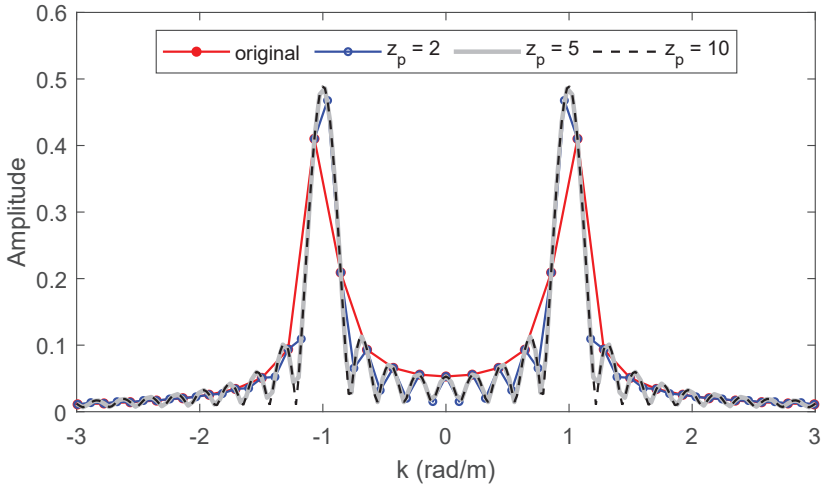

Figure 3.2. Typical features of a wavenumber spectrum and influence of zero padding on the leakage.

Chapter 4

Summary of the included papers

4.1 Paper #1, #2, #3 and #4

Paper #1: Experimental modal analysis on Woodsol hollow box floor elements.
Paper #2: Challenges and limitations using the Integral Transform Method to obtain the impact noise level of timber floors.
Paper #3: Benchmarking the vibration velocity-based measurement methods to determine the radiated sound power from floor elements under impact excitation.
Paper #4: Sound radiation of hollow box timber floors under impact excitation: an experimental parameter study.

Paper #1, #2, #3 and #4 build upon each other and their results can be best presented in a coherent discussion.
Paper #1 and *Paper #2* are conference papers written in an early stage of the project and are included in this thesis for two main reasons: i) they provide some details of the experimental setups that were not included in the later papers and ii) they document the learning process I went through with this PhD work. We prepared *Paper #1* after completing the first set of the EMA measurements, which were focused on the global modal properties of the floor elements. The measurement were aimed at collecting data for model validation. The results allowed additionally to start investigating the effect of the floor element size and of the boundary conditions on the modal behaviour of the floor elements. The paper describes the measurement setup and the adopted EMA procedure. The measurement program included activities on the free-free setup (section 2.2.1) and CVGS mock-up (section 2.2.2). The measurements with free-free boundary conditions provided an accurate description of the dynamic behaviour of the floor elements at low frequency. The measurements on the CVGS mock-up showed the necessity of improving the mock-up to obtain better data. The modal behaviour of the undamped pinned columns dominated the dynamic behaviour of the system be-

low 40 Hz, hiding the lowest vibrational modes of the floor elements. This lead to an upgrade of the mock-up, i.e., to the relative stabilisation of the heads of the columns with aluminium profiles. The data obtained with the upgraded mock-up were included in *Paper #4*.

Paper #2 documents our familiarization process with the ITM and investigates how it could be applied to our project to obtain the impact noise level of timber floors. It provides all necessary equations to implement the ITM method and discusses some of the most important parameters, e.g., grid size and zero padding. It also provides a basic relation to convert the radiated sound power into impact noise level. It presented preliminary results and a basic analysis but it did lack of a validation of the method for the purpose of measuring impact sound levels. All aspects were deepened in the later work and presented in a more mature way in paper #3.

Paper #3 represents the most important part of this work with respect to the adopted measurement method to determine the radiate sound power from the floor elements under impact excitation. The paper presents the three methods RIM, ITM and DCM and compare their results as a validation procedure. The methods applied to the determination of airborne sound insulation are well documented in literature so that we focused on impact excitation and on the aspects that seemed most critical for our application, i.e. various type of boundary conditions and excitation by a tapping machine at several locations. The results in the paper provide a validation of the methods to determine the radiated sound power under impact excitation. The results demonstrate that DCM, ITM and RIM can be used with the ISO tapping machine excitation and extend the application of this methods from airborne sound insulation to include impact sound insulation.

Paper #4 paper builds on the previous papers and presents the answers to both the first and the second research question. By combining the EMA and ITM results, it presents a detailed description of the vibroacoustic behaviour of the floor elements. The focus is on the global dynamic behaviour and the sound radiation from the floor elements. The paper presents an investigation on how these two aspects depend on selected governing parameters, i.e., the boundary conditions, the size and the additional mass (gravel) in the cavity. In the paper's appendix, I present the investigation of two specific questions related to the experimental setup: is the airborne excitation generated by the noise emitted by the tapping machine acting on the upper plate a limitation for the validity of the results? Can we use symmetry properties of the floor elements to shorten the measurement time?

In the following, I highlight the main findings from these papers, grouping them into 6 main topics: i) measurement method, ii) floor element general behaviour, iii) size effect, iv) additional mass effect, v) effect of mounting to the columns and vi) bending wave dispersion curves.

Measurement method

The combination of EMA and ITM proved to be a powerful tool to investigate in detail the vibroacoustic behaviour of the floor elements. There is of course some redundancy in the information obtained: the mode shapes and the natural frequencies can be obtained by both EMA and ITM. However, EMA is a specialised tool for modal analysis and offers ready to use advanced algorithms that may be helpful in challenging situations, as e.g. when two natural frequencies are very close to each other. EMA algorithms deliver directly damping information and the results format is well suited to be used with the model validation techniques.
We demonstrated and validated that ITM is a suitable tool to investigate impact sound levels *in-situ*. DCM and RIM are alternative methods, which give comparable quality of the results, when the respective requirements are fulfilled. ITM is a rather advanced measurement method and some experience is required to apply it properly. The ITM delivers the following results within the same analysis procedure: radiated sound power, radiation factor, structural waves dispersion curve and even the supersonic intensity. Compared to the standard laboratory methods, the ITM offers advantages that are critically relevant when considering frequencies in the low frequency range, i.e., between 20 Hz and 150 Hz. Standard laboratories measurements imposes constraints to the size of the specimen and to the boundary conditions. Since ITM can be used *in-situ* it overcomes these limitations and delivers more accurate data. In addition, the effects due to the sound field in the receiving room not being diffuse at low frequencies are avoided by using ITM. In our case, the measurement results obtained with the ITM methods were not affected by the direct airborne excitation when investigating impact sound. This means that the method can be successfully used in an industrial hall and makes possible accurate measurements of the impact sound level *in-situ*. Compared to other measurement methods, e.g., sound intensity, the ITM method poses less requirements on the measurement environment and can therefore be very advantageous.
However, there are limitations also on the ITM method. The requirements on the measurement grid size depends both on the wavelength of the bending waves in the material and on the boundary conditions. This can be a challenge and requires accurate planning of the experiment. The measurement time can be longer compared to the standard measurement methods. In our case, the measurement time for one floor element with 4 tapping machine positions was 2 hours while the standard measurement takes probably less than one hour. Using a scanning laser vibrometer could increase the efficiency of the measurement procedure by reducing the time where human interaction is required to the placement of the tapping machine. Unluckily, symmetry properties of the measurement object cannot generally be exploited to reduce the measurement time. Deviations that arise by measuring only a portion of the specimen and then converting to the total area by symmetry con-

siderations are most pronounced at very low frequencies, in our case below 50 Hz. With increasing modal density, these deviations become less and less significant.

Floor element general behaviour

The measurements on the floor element allowed the identification of three frequency ranges where the vibratory behaviour assumes different characteristics: i) below 150 Hz, the elements shows a lumped behaviour and the vibrational properties can be described by homogenized material properties; ii) a transitions zone from 150 Hz up to 500 Hz; iii) above 500 Hz, the single components of the floor element behaviour dominate the sound radiation, e.g., the bottom plate. In the frequency range below 150 Hz, we observed stronger effects of the size and the boundary conditions. This fits well with the statement from Hopkins [21] that indicates the 10^{th} local mode as an approximate limit between two ranges: the range below it with low modal density and the range above it with high modal density, where it is reasonable to adopt a statistical approach to the prediction of sound transmission. In the upper range, the statistical modal density is not significantly affected by the boundary conditions and sample size. Consequently, the sound radiation properties are less affected by the frequency distribution of the vibrational modes with increasing frequency.

Effect of the floor element size on modal behaviour and sound radiation

In the low frequency range, i.e., below 150 Hz, the effects of the element's size is most evident. The effect on the impact noise level is up to 10 dB. Surprisingly, the radiated sound power in the low frequency range decreased with increasing length (4.7 m element compared to 9 m element). This is linked to the vibrational modes distribution and the combination of stiffness and length of the elements.

Effect of additional mass in the cavity of the floor element

The mass and damping introduced by means of the gravel in the cavity effectively reduce the radiated sound power for frequencies above approximately 50 Hz. With 100 kg/m^2 gravel, we achieved a radiated sound power reduction that largely exceeded 10 dB over wide frequency ranges. The results from *Paper #5* show that this effect is limited to approximately 1250 Hz. For frequencies below 50 Hz, the effect of gravel is limited and some modes (e.g., torsional) might not be affected at all by the additional mass.

Effect of the moment resisting connection on the modal behaviour and on the sound radiation

When comparing free-free boundary conditions with the elements mounting on the columns, we observed three main effects: i) the amplitude of torsional modes is dramatically reduced, ii) the natural frequencies of the longitudinal modes are shifted towards higher frequency, iii) modal damping is increased on selected modes. The cumulated result of these effect is a reduction of the radiated sound power of up to 3 dB in the low frequency range. The actual effect depends strongly on the modal distribution and on the modal properties, imposing strong requirements on the boundary conditions of a measurement setup.
In the CVGS measurement setup, the columns were only lightly damped and the effect of their behaviour could be clearly recognised in the FRFs. This slightly influences the results in the frequency range around 20 Hz. We expect this feature to be different in a complete building and might be a limitation of the achieved results. It would be interesting to understand the behaviour of the columns in a complete building or at least in a two storey mock-up as originally planned.
The measurements also showed a rigid body motion of the floor elements on the supporting bracket in vertical direction at frequencies between 20 Hz and 30 Hz. When considering the full length of the elements, i.e. double mass, this might be relevant for the comfort properties and the serviceability criteria but the topic is outside the scope of this thesis.

Bending wave dispersion curves

For ease of reference, I reproduce in figure 4.1, figure 12 from *paper #4*. The figure shows the measured wavenumber spectrum of a Woodsol floor element. In the diagram, the magnitude of the velocity is normalized at its maximum in each frequency step. The normalization is very effective for the visualization of the dispersion curves. However, it has the drawback of hiding the frequency dependency of the amplitude and the actual contributions to sound radiation. The high intensity trace (yellow colour) describes the dispersion curve of the bending waves. The trend is articulated and reflects the complexity of the floor elements: we are dealing with an object composed by several orthotropic elements (both the glulam stringer and the LVL plates are orthotropic) and a highly inhomogeneous cross section with periodic elements (the stringers). We attempted to identify the link between the features of the dispersion curves and the components of the floor elements starting from the approach presented in [33], which is based on an equivalent elliptical model of the orthotropic material properties. Some rough engineering approximations were additionally made: at low frequencies, I assumed that a description

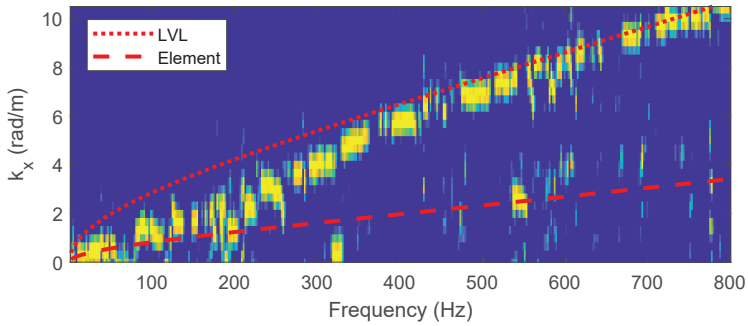

Figure 4.1. Figure 12 from *paper #4* showing the measured wavenumber spectrum of a Woodsol floor element in longitudinal direction with overlaid bending wave speed dispersion curves.

based on the lumped properties measured by means of deflection measurements might be satisfactory. At high frequency, I assumed that the LVL plate would be dominant. We focused only on the longitudinal direction of the element and performed the analysis as if the properties were isotropic. The curves *Element* and *LVL* in the figure were calculate using equation 3.6, with following quantities: for both curves, h was taken as the physical height of the element $h = 509$ mm, and the density ρ was calculated as the element total volume divided by the element total weight. For the curve *Element*, experimental values obtained from deflection measurements were used for the bending stiffness, as described in *paper #4*. For the curve *LVL*, following relation was used to calculate the bending stiffness:

$$B_p = E_{LVL,y} \frac{W_E h_{LVL}^3}{12(1 - \nu_{LVL}^2)} \tag{4.1}$$

where the LVL Young's modulus for the longitudinal direction $E_{LVL,y}$ is taken from the datasheet (Metsä Wood Kerto-Q), W_E is the width of the element, $h_{Kerto} = 63$ mm is the thickness of the LVL bottom plate and the Poisson's ratio $\nu_{Kerto} = 0.6$ is also from the datasheet. The obtained curves seems to confirm my assumptions: we observe three regions in the diagram. In the lower frequency range, the trace is closer to the curve *Element*. In the upper frequency range, the trace is closer to the curve *LVL* while in between there is a transition region.
An additional analysis of the vibroacoustic features of the Woodsol floor element could focus on the periodic properties of the elements, following for instance the approach presented in [32]. This might reveal properties linked to the quantity $k = 2\pi/D$ with $D = 565$ mm distance between the stringers. However, with the utilised setup, this analysis was not possible since the corresponding value $k = 11.1$ rad/m is beyond k_{max}. The corresponding features are expected above 800 Hz.

4.2 Paper #5

Paper #5: Sound insulation of timber hollow box floors. Collection of laboratory measurements and trend analysis.

The results presented in *Paper #5* allow an assessment of the overall acoustic performance of the floor element, both in terms of airborne and impact sound insulation. By comparing similar objects and a range of solutions, we could study the effect of various parameters and identify trends with respect to stiffness properties, mass, resonance frequencies and properties of the involved resilient products. The paper investigates the performance of the bare floor with different cavity filling and the improvement that can be achieved with various types of floating floor. Results are presented both frequency-dependent and as single-number quantities. Here, I will summarize only the results relating to the single number quantities and refer to the paper for more details. For ease of reference, I recall in table 4.1 the requirements for dwellings and offices according to NS 8175:2019 [48], class C . In table 4.2, I list a selection of solutions that we tested with the Woodsol floor

Table 4.1. Acoustic requirements according to NS 8175:2019 [48], class C.

Type of space	Airborne sound	Impact sound
Between dwellings	$\mathrm{R'_w} + \mathrm{C_{50-5000}} \geq 54\,\mathrm{dB}$	$\mathrm{L'_{n,w}} + \mathrm{C_{I,50-2500}} \leq 54\,\mathrm{dB}$
Between offices	$\mathrm{R'_w} \geq 37\,\mathrm{dB}$	$\mathrm{L'_{n,w}} \leq 63\,\mathrm{dB}$
Between office and meeting room	$\mathrm{R'_w} \geq 44\,\mathrm{dB}$	$\mathrm{L'_{n,w}} \leq 63\,\mathrm{dB}$

element. Each solution is a combination of a cavity filling and a floating floor. I show in table 4.3 the corresponding acoustic performance as single number quantities. In table 4.3, I highlighted the solutions that might fulfil the requirements for dwellings from table 4.1, under the assumption that flanking transmission is tackled accordingly. Note that in the table, I present the actual value of the sum $\sum_L = \mathrm{L_{n,w}} + \mathrm{C_{I,50-2500}}$, both for positive and negative values of $C_{I,50-2500}$. In the evaluation according to the NS 8175, the negative values must be discarded.

Table 4.2. Selection of cavity fillings and floating floor solutions for a Woodsol floor element.

	Cavity fill	Fill m'	Floating floor
A	empty	-	
B	wood fibre	13 kg/m^2	-
C	gravel	100 kg/m^2	-
D	gravel	100 kg/m^2	lightweight floating floor on continuous resilient layer, $s' < 15$ MN/m^3
E	gravel	100 kg/m^2	lightweight floating floor on point elastic supports (50 mm x 100 mm x 12,5 mm sylodyn ND, c-c ca. 500 mm)

Table 4.3. Single number quantities for the solutions described in table 4.2. Following abbreviations were used: $\sum_R = \mathrm{R_w} + \mathrm{C_{50-5000}}$, $\sum_L = \mathrm{L_{n,w}} + \mathrm{C_{I,50-2500}}$.

	total m' (kg/m^2)	R_w (dB)	$C_{50\text{-}5000}$ (dB)	$\sum_R$ (dB)	$L_{n,w}$ (dB)	$C_{I,50\text{-}2500}$ (dB)	$\sum_L$ (dB)
A	100	35	0	35	85	-2	83
B	113	39	0	39	83	-3	80
C	200	45	0	45	79	-4	75
D	230	60	-1	**59**	52	+2	**54**
E	220	61	-1	**60**	50	+1	**51**

The trend lines given in table 4.4 were identified based on the data collected. They provide order of magnitudes for the weighted normalised impact sound pressure level and may be useful in preliminary dimensioning of new floor elements on the basis of the total mass per unit area of the element m', i.e. including bare floor, cavity filling and floating floor. The trend lines are provided for following constructions: i) bare floor, ii) floating floor built with gypsum fibre-boards, e.g., Fermacell, on continuous resilient layer with dynamic stiffness s' > 15 MN/m^3, iii) floating floor built with dry screed, e.g., plasterboard, on continuous resilient layer with dynamic stiffness s' > 15 MN/m^3, iv) as iii) but with low dynamic stiffness s' < 15 MN/m^3 and iv) wet screed on continuous resilient layer with low dynamic stiffness s' < 15 MN/m^3. These relationships are based on a limited number of objects and therefore should be used cautiously.

Table 4.4. Trend lines for weighted normalized impact sound pressure level with the spectrum adaptation term $C_{I,50-2500}$ in dB from *paper # 5*. m' indicates the total mass per unit area of the element.

Floating floor	Resilient layer	Trend line
bare floor (no additional layer)		$L_{n,w}+C_{I,50-2500} = 101-10\log m'$
gypsum fibre board	s' > 15 MN/m^3	$L_{n,w}+C_{I,50-2500} = 82-30\log m'$
plasterboard	s' > 15 MN/m^3	$L_{n,w}+C_{I,50-2500} = 87-30\log m'$
plasterboard	s' < 15 MN/m^3	$L_{n,w}+C_{I,50-2500} = 80-30\log m'$
wet screed	s' < 15 MN/m^3	$L_{n,w}+C_{I,50-2500} = 210-65\log m'$

The paper also proposes an equation to estimate the improvement of the impact sound level due to the the gravel effect:

$$\Delta(L_{n,w}+C_{I,50-2500}) = 0.12\cdot\Delta m'_{gravel} \tag{4.2}$$

where $\Delta m'_{gravel}$ is the additional mass of the element in $\mathrm{kg/m^2}$ due to the gravel. As stated above, also this relationship has to be used cautiously.
As an example of the application of these data, we can determine the mass per unit area required to meet the requirements suggested in the NS 8175:2019 between dwellings, class C [48], assuming that flanking sound transmission is negligible. The results are shown in table 4.5. Note that the estimate on the impact noise level requires a resilient layer with low dynamic stiffness ($s' < 15$ MN/m^3). In both cases, an optimization of the materials might lead to a slight reduction of the required mass.

Table 4.5. Estimated total mass per unit area of the floor element necessary to meet the requirements for dwellings according to NS 8175:2019, class C.

	Requirement	m$'$
Airborne sound	$\mathrm{R'_w + C_{50-5000} \geq 54dB}$	$\geq$ 200 kg/m^2
Impact sound	$\mathrm{L'_{n,w} + C_{I,50-2500} \leq 54dB}$	$\geq$ 260 kg/m^2 and resilient layer with $s' < 15$ MN/m^3

Based on the data presented in the paper, we elaborated, together with the project partners, a possible office building concept with detail drawings [49]. The concept is based, for the time being, only on direct sound transmission considerations and will be further detailed as the analysis on flanking sound transmission is

completed. Figure 4.2 shows a detail of the floor between two offices (left side) and two meeting rooms (right side), respectively, which fulfils the corresponding acoustic requirements for office buildings in Norway (see table 4.1). The total

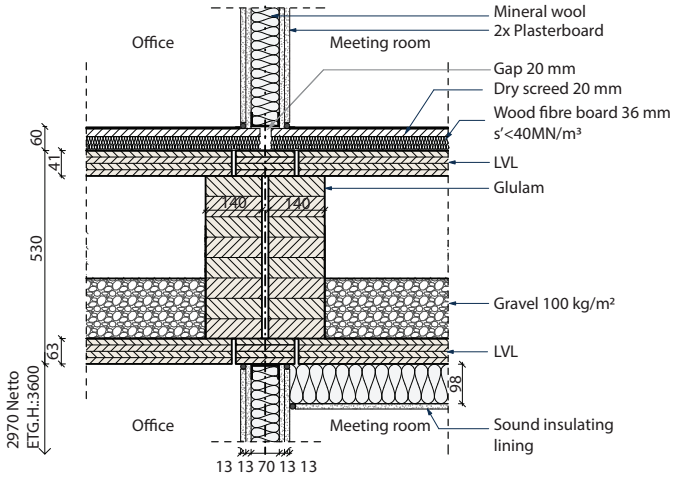

Figure 4.2. Construction detail for a Norwegian office building. Requirement according to NS 8175:2019, class C. Adapted from [49].

height of the construction amounts to 600 mm. According to the project partners, this is a competitive element height for the target span of up 10 m, compared to concrete and steel constructions.

4.3 Paper #6

Paper #6: Structural reverberation time measurements on Woodsol prototype.

This paper completes the characterization of the properties of the Woodsol floor elements and the moment resisting frame. The work described therein was the first step towards the investigation of the flanking sound transmission. Several important results are presented in the paper, regarding both the specific properties of the floor element and the measurement method. I discuss here only the results regarding the measurement method, which are generally applicable, and refer to the paper for the further results.

The reverberation time can be measured either with impact hammer or shaker excitation. Impact hammer excitation offers many practical advantages compared to shaker excitation. However, the standard ISO 10848-1 [25] indicates shaker excitation as the preferred excitation to avoid non-linearities effects. While the

effect of non-linearities seems to have a strong influence on the measurement results for heavy-weight constructions, e.g., masonry, it is not the case for lightweight constructions. We compared the results obtained with the two excitation sources to gain more knowledge on this aspect. We could confirm that this requirement is not as important in lightweight building elements. The use of hammer excitation greatly simplifies the measurement procedure without any significant loss in accuracy.

The Woodsol floor elements are strongly inhomogeneous lightweight structure and exhibit very different properties on the top and bottom side. Therefore, they poses several challenges to the standard method described in ISO 10848-1. We investigated the dependency of the measured reverberation time on the excitation and response position arrangement. We observed a strong dependency of the results on both the excitation and the sensors position. We registered longer reverberation times on the upper lightly damped surface of the element and shorter reverberation times on the lower surface, which was highly damped by the gravel. Consequently, one might have to consider the specific application of the results when deciding on the measurement positions to consider. How far this affects the further considerations on the flanking transmission is a question that remains to be addressed.

We observed differences in the measured transfer functions. This could certainly have an influence on the results of an EMA. However, the typical procedure of the EMA include at least two elements that are intended to limit non-linearities in the measurements. The first one is the *good practice* to hit the structure with as little force as it is needed to obtain a good signal to noise ratio. This goes together with the use of a relatively small hammer and has specifically the objective to avoid exciting non-linearities. The second element is that multiple impacts are used at each measurement position and in the analysis procedure only impacts with similar amplitude are selected. Also a visual check of the obtained transfer functions and possibly of the effect of averaging different impacts is part of the procedure and helps obtaining uniform measurement data. Since in our case, both damping values from the EMA and reverberation time measurements are available for the frequencies up to about 100 Hz, it could be interesting to compare the respective values, which are strongly related. However, the analysis is not entirely straightforward, specially in the case where several modes with different amplitudes and damping are within one frequency band. We can still try the comparison for one selected case: the EMA measurement performed on the 4.7 m element, with gravel mounted on columns. The second transverse mode has natural frequency $f_0 = 54.5$ Hz and $\zeta = 4.9$ % (data from table 4 in Paper #4). Following relationships holds between damping ζ and reverberation time RT:

$$RT = \frac{1.1}{\zeta f_0} \tag{4.3}$$

Substituting the corresponding values, we obtain $RT = 0.4$ s, which is clearly below the value $RT = 1.4$ s obtained from the reverberation time measurements for the 50 Hz 1/3 octave band. However, the reverberation time data show a rather large standard deviation ($\sigma = 0.9$ s for the shaker measurements and $\sigma = 0.8$ s for the impact hammer). On the EMA side, we are looking at just one mode. Further analysis would be needed to understand in detail the deviation between the two procedures.

Chapter 5

Major contributions and further work

5.1 Answers to the research question

The work presented in this thesis focused on hollow-box floor elements, their modal behaviour and the radiated sound power under impact excitation at low frequencies. I identified, analysed and used advanced measurement methods that allowed me to investigate the influence of the mounting condition, the influence of the floor size and the influence of additional mass on these aspects. I compared the results obtained on a mock-up of the Woodsol system with results obtained in a standard laboratory. We compiled a collection of hollow-box floor elements from different producers, analysed the parameters governing their acoustic performance and identified general trends. Furthermore, I selected and tested construction solutions suitable for the Norwegian building industry, that are able to fulfil the Norwegian acoustic requirements. I structured my work around the four research questions formulated in section 1.4. Below I summarize the answers we found.

Q1. How to assess modal behaviour and direct sound transmission?
Standard transmission suites in acoustic laboratories have typically an opening size of around 3 m x 4 m. The specimen is normally installed in the opening by letting it rest on its edges, possibly with an interposed resilient layer. This corresponds to boundary conditions close to simply supported. When considering the impact sound insulation at frequencies below 150 Hz, both the opening size and the boundary conditions of a standard transmission suite can be a limitation to the accuracy of the data. At higher frequencies, the modal density increases and the measurement results are not strongly affected by the size of the specimen and

the boundary conditions.
By using EMA, I showed that both the size and the boundary condition of the specimen have an influence on the vibration modes' distribution. At frequencies below 150 Hz, where the modal density is low, this can have a considerable effect on sound radiation. The measurements that I performed with ITM showed up to 3 dB difference on the radiated sound power level in 1/3 octave band, while changing the boundary conditions from free-free to the specific project boundary conditions (clamped at the corner). The effect of the size was up to 10 dB while comparing the 4.7 m element to the 9 m element.
These results show that to obtain accurate data at low frequencies, measurements shall be performed with representative object size and boundary conditions. The ITM is a suitable measurement method that can be used to meet these requirements and obtain reliable results.

Q2. Are vibration velocity based measurement methods a suitable tool?
The ITM, RIM and DCM are valid alternatives to measurements in a standard acoustic laboratory to determine the radiated sound power from building elements. All these methods can be used to determine the radiated sound power from a floor element under impact excitation *in-situ*, offering advantages compared to the standard measurement procedures based on measuring sound pressure levels in a transmission suite. The application of ITM *in-situ* allows the use of the specific boundary conditions of the investigated system and it does not underlay size limitations due to e.g., opening size of the laboratory. Additionally the methods offer increased accuracy because the measurement is not dependent on the sound field in the receiving room, which at low frequencies is not diffuse. Furthermore, the ITM delivers additional information compared to standard measurements such as the radiation factor and insights in the material properties.

Q3. What are the typical properties of the Woodsol floor element?
The results from EMA showed the typical modal distribution of the Woodsol floor elements. The mode shapes and their natural frequency show the effect of the high stiffness of the elements in the longitudinal direction and the lower stiffness in the transverse direction. The vibration mode distribution determined by the length of the elements and the high stiffness, resulted in a lower sound radiation from the Woodsol element compared to similar products at low frequencies.
The boundary conditions affect the modal behaviour of the floor element by shutting down specific modes and by slightly increasing the modal damping. Both effects contribute to a reduced sound radiation.
Table 4.3 shows the acoustic performance of the Woodsol floor elements for the bare floor with and without additional mass in the cavity and with different floating floors. The results show that the gravel in the cavity dramatically improves the air-

borne and impact sound insulation in the range between 50 Hz and 1250 Hz. The measurements showed an improvement of 10 dB on $R_w + C_{50-5000}$ and of 8 dB on $L_{n,w} + C_{I,50-2500}$ with 100 kg/m^2 gravel. Although this is, in general, not sufficient to fulfil even basic acoustic requirements, it is a necessary and effective way of approaching them. The measured floating floor solutions build a comprehensive collection that can be used to fulfil a wide range of acoustic requirements.
The trend lines presented in table 4.4 provide a relationship between the mass per unit area of the floor element and the quantity $L_{n,w} + C_{I,50-2500}$, allowing an efficient preliminary assessment and dimensioning of hollow-box floor elements based on given acoustic requirements.

Q4. What would a practical solution look like?
The floor solutions presented in figure 2.5 are all based on standard solutions that are currently used by the Norwegian building industry. We tested this solutions on a Woodsol floor element. Based on the obtained results, we could draft practical floor solutions for office and residential buildings based on the Woodsol system, which can fulfil the acoustic requirements according to the standard NS 8175:2019. The relatively low requirements for an office building can be fulfilled with a simple solution: a hollow-box floor element filled with 100 kg/m^2 gravel and a floating dry screed installed on top by means of a continuous resilient layer with dynamic stiffness $s' < 40 MN/m^3$. Floor solutions based on a resilient layer with low dynamic stiffness $s' < 15 MN/m^3$ or on point elastic resilient supports and dry screed deliver a much higher performance and can fulfil the requirements for residential buildings. The solution with point elastic resilient supports appeared to be the most versatile and best performing giving room for optimization of the cavity filling.

5.2 Further work

Within the work for this thesis, I obtained detailed results describing the modal behaviour and the direct sound transmission through the floor elements of the Woodsol systems. I showed how different standard solutions perform when combined with the Woodsol floor element. It would be interesting to compare the performance of these solution when combined with other constructions, e.g. cross laminated timber floors, concrete floors or other types of lightweight constructions.
The analysis of the flanking sound transmission could not be included in this thesis and remains as further work. I collected a comprehensive dataset that will allow the investigation of the flanking transmission in a horizontal direction, i.e., from floor element to floor element and the vibration transmission from the floor elements to the columns. However, a thorough analysis of the data is yet to be concluded. We expect that looking into the energy balance between the subsystems i) source floor-element, ii) transmission path and iii) receiver floor element will provide important insights to understand and predict the flanking transmission in a Woodsol building. The complete data is available for each subsystem and includes the structural reverberation time, source subsystem vibration velocity level and receiver subsystem vibration velocity level.
Within the scope of this thesis, I focused on the experimental methods and did not look into the prediction models. However, the data collected and the knowledge gathered would allow setting up suitable FEM, SEA or hybrid engineering models for the floor elements and the building system and validate them.
The Woodsol project will continue until 2021 focusing on solving the structural issues. The complete project documentation will include guidelines on how to fulfil acoustical requirements in buildings with different scope of use. The data produced within this work provide all the information to achieve this goal.

Bibliography

[1] K. A. Malo, *Woodsol application for NFR research project*, NTNU, Trondheim, 2015.

[2] Pöyry Management Consulting, *Markeds-analyse av skognæringen i norge*, Innovasjon Norge, 2014.

[3] G. Olofsson, *Skog22 nasjonal strategy for skog og trenæringen*, Det kongelige Landbruks- og matdepartementet, Oslo, Norway, 2015.

[4] Statsbygg, *Tre for bygg og bygg for tre. kunnskapsgrunnlag for økt bruk av tre i offentlige bygg*, Det Kongelige landbruks- og matdedartement, Oslo, Norway, 2013.

[5] K. A. Malo and J. Köhler, 'Vibrations of timber floor beams with end restraints,' in *Structures and Architecture: Concepts, Applications and Challenges–Proceedings of the 2nd International Conference on Structures and Architecture, ICSA*, P. Cruz, Ed., CRC Press, 2013, pp. 181–189.

[6] A. Homb, *Evaluering av lydegenskaper for bærende dekkekonstruksjoner, Woodsol report no. 01/17*, SINTEF Community, Trondheim, 2017.

[7] H. Halstedt, *Woodsol prototype element production drawings*, SINTEF Community, Trondheim, 2018.

[8] K. A. Malo and H. Stamatopoulos, 'Connections with threaded rods in moment resisting frames,' in *Proceedings of the World Conference on Timber Engineering (WCTE 2016)*, 2016.

[9] A. Vilguts, K. A. Malo and H. Stamatopoulos, 'Moment resisting frames and connections using threaded rods in beam–to-column timber joints,' in *Proceedings of the World Conference on Timber Engineering (WCTE 2018)*, 2018.

[10] F. Ljunggren, C. Simmons and K. Hagberg, 'Correlation between sound insulation and occupants' perception – proposal of alternative single number rating of impact sound,' *Applied Acoustics*, vol. 85, pp. 57–68, 2014.

[11] F. Ljunggren, C. Simmons and R. Öqvist, 'Correlation between sound insulation and occupants' perception – proposal of alternative single number rating of impact sound, part ii,' *Applied Acoustics*, vol. 123, pp. 143–151, 2017.

[12] R. Öqvist, 'Measurement and perception of sound insulation from 20 hz between dwellings,' PhD thesis, Luleå tekniska universitet, 2017.

[13] K. Hagberg, 'Management of acoustics in lightweight structures,' PhD thesis, LTH, Lund, 2018.

[14] J. Olsson, 'Low Frequency Impact Sound in Timber Buildings: Transmission Measurements and Simulations,' PhD thesis, Linnaeus University, 2019.

[15] *ISO 10140-2:2010 Acoustics — Laboratory measurement of sound insulation of building elements — Part 3: Measurement of airborne sound insulation*.

[16] *ISO 10140-3:2010 Acoustics — Laboratory measurement of sound insulation of building elements — Part 3: Measurement of impact sound insulation*.

[17] *ISO 16283-2:2018 Acoustics – Field measurement of sound insulation in buildings and of building elements – Part 2: Impact sound insulation*.

[18] N. B. Roozen, L. Labelle, M. Rychtáriková and C. Glorieux, 'Determining radiated sound power of building structures by means of laser doppler vibrometry,' *Journal of Sound and Vibration*, vol. 346, pp. 81–99, 2015.

[19] N. Hashimoto, 'Measurement of sound radiation efficiency by the discrete calculation method,' *Applied Acoustics*, vol. 62, no. 4, pp. 429–446, 2001.

[20] *ISO 15186-1:2000 Acoustics - Measurement of sound insulation in buildings and of building elements using sound intensity – Part1: Laboratory measurements*.

[21] C. Hopkins, *Sound Insulation*. Elsevier / Butterworth-Heinemann, 2007.

[22] A. Homb and S. Conta, 'Strategies to evaluate acoustic properties of timber hollow box floors,' in *INTER-NOISE Conference Proceedings*, Madrid: Institute of Noise Control Engineering, 2019.

[23] S. Schoenwald, S. Vallely and H.-M. Tröbs, 'Advanced methods to determine sound power radiated from planar structures,' *The Journal of the Acoustical Society of America*, vol. 141, no. 5, pp. 3713–3713, 2017.

[24] M. Kohrmann, 'Numerical methods for the vibro-acoustic assessment of timber floor constructions,' PhD thesis, Technische Universität München, 2017.

[25] *ISO 10848-1 Acoustics - Laboratory and field measurement of flanking transmission for airborne, impact and building service equipment sound between adjoining rooms*.

[26] J. Y. Jeon, J. K. Ryu, J. H. Jeong and H. Tachibana, 'Review of the impact ball in evaluating floor impact sound,' *Acta Acustica united with ACUSTICA*, vol. 92, no. 5, pp. 777–786, 2006.

[27] A. Homb, 'Low frequency sound and vibrations from impacts on timber floor constructions,' PhD thesis, NTNU, Trondheim, 2006.

[28] C. Lothar, H. Manfred and B. A. T. Petersson, *Structure-borne sound: structural vibrations and sound radiation at audio frequencies*. Springer, 2005.

[29] C. Winter, 'Frequency dependent modeling for the prediction of the sound transmission in timber constructions,' PhD thesis, Technische Universität München, 2018.

[30] S. A. Hambric, S. H. Sung and D. J. Nefske, *Engineering vibroacoustic analysis: methods and applications*. John Wiley & Sons, 2016.

[31] B. Van Damme and A. Zemp, 'Measuring dispersion curves for bending waves in beams: A comparison of spatial fourier transform and inhomogeneous wave correlation,' *Acta Acustica united with Acustica*, vol. 104, no. 2, pp. 228–234, 2018.

[32] M. N. Ichchou, J. Berthaut and M. Collet, 'Multi-mode wave propagation in ribbed plates: Part i, wavenumber-space characteristics,' *International Journal of Solids and Structures*, vol. 45, pp. 1179–1195, 2008. DOI: https://doi.org/10.1016/j.ijsolstr.2007.09.032.

[33] A. Santoni, S. Schoenwald, B. Van Damme and P. Fausti, 'Determination of the elastic and stiffness characteristics of cross-laminated timber plates from flexural wave velocity measurements,' *Journal of Sound and Vibration*, vol. 400, pp. 387–401, 2017.

[34] R. D. Blevins, *Formulas for natural frequency and mode shape*. New York: Van Nostrand Reinhold, 1979.

[35] A. W. Leissa, *Vibration of plates*. Scientific and Technical Information Division, NASA, 1969.

[36] A. W. Leissa, 'The free vibration of rectangular plates,' *Journal of sound and vibration*, vol. 31, no. 3, pp. 257–293, 1973.

[37] G. B. Warburton, 'The vibration of rectangular plates,' *Proceedings of the Institution of Mechanical Engineers*, vol. 168, no. 1, pp. 371–384, 1954.

[38] A. Brandt, *Abravibe toolbox for experimental modal analysis,* `http://www.abravibe.com`.

[39] A. Brandt, *Noise and vibration analysis: signal analysis and experimental procedures*. John Wiley & Sons, 2011.

[40] D. J. Ewins, *Modal testing: Theory, Practice and Application*. Research studies press LTD, 2000.

[41] J. W. S. B. Rayleigh, *The theory of sound*. New York: Dover Publications, 1945, vol. 1, 2.

[42] T. E. Vigran, *Building acoustics*. CRC Press, 2014.

[43] J. D. Maynard, E. G. Williams and Y. Lee, 'Nearfield acoustic holography: I. theory of generalized holography and the development of nah,' *The Journal of the Acoustical Society of America*, vol. 78, no. 4, pp. 1395–1413, 1985.

[44] W. A. Veronesi and J. D. Maynard, 'Nearfield acoustic holography (nah) ii. holographic reconstruction algorithms and computer implementation,' *The Journal of the Acoustical Society of America*, vol. 81, no. 5, pp. 1307–1322, 1987.

[45] C. C. Fuller, S. Elliott and P. A. Nelson, *Active control of vibration*. Academic Press, 1996.

[46] M. C. Junger and D. Feit, *Sound, structures, and their interaction*. MIT press Cambridge, MA, 1986.

[47] L. E. Kinsler, A. R. Frey, A. B. Coppens and J. V. Sanders, *Fundamentals of acoustics*. Wiley-VCH, 1999.

[48] *NS 8175:2019 Acoustic conditions in buildings - Sound classification of various types of buildings*.

[49] A. Homb and S. Conta, *LYDISOLERING Woodsol dekker til kontorbygg, Woodsol report no. 01/19*, SINTEF Community, Trondheim, 2019.

Appendix A

Included papers

Paper #1

26th INTERNATIONAL CONGRESS ON SOUND AND VIBRATION
7-11 July 2019, Montreal

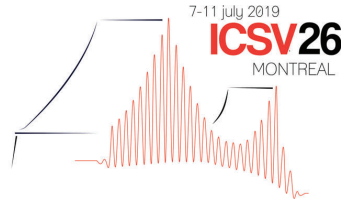

EXPERIMENTAL MODAL ANALYSIS ON WOODSOL TIMBER HOLLOW BOX FLOOR ELEMENTS

Simone Conta
Norwegian University of Science and Technology NTNU, Trondheim, Norway
email: simone.conta@ntnu.no

Anders Homb
Norwegian University of Science and Technology NTNU, Trondheim, Norway
email: anders.homb@ntnu.no

Woodsol is a Norwegian research project aiming at developing a timber building construction system based on long span floor elements and moment resisting frames. Due to the long span requirement and the lightweight construction, we expect major challenges at low frequencies when looking at the impact sound insulation. To address this issue and develop suitable strategies for improvement, we studied among other the modal properties of the floor element. We scheduled a large measurement program allowing for investigating different floor sizes, the effect of additional mass in the floor cavity and two type of boundary conditions. The first type are free-free boundary conditions aimed at collecting data for the validation of the finite element models. As the other boundary conditions type, we built one cell of the building frame system accurately representing the mounting situation of the floor element on the moment resisting frame with the special connectors. On each setup, we performed an experimental modal analysis of the floor elements, using the roving hammer technique with multiple reference accelerometers. The paper will present the results obtained so far and discuss both the measurement procedure and analysis of the measurement data. We will also discuss the expected effect of the modal behavior on the impact sound insulation of the floor elements.

Keywords: modal analysis, timber, impact sound

1. Introduction

The WOODSOL project aims at developing urban buildings up to ten stories featuring large architectural flexibility [1]. Two key topics of the project are the long span floor elements and the moment resisting frames.
The strategy that we are following to develop suitable acoustical solution within the project includes following three main steps [2]: 1) assess basic vibroacoustic properties and collect data for model validation using the experimental modal analysis, 2) study the sound radiation and impact sound insulation using the integral transform method [3], 3) perform junction transmission measurements to study flanking transmission in the system.

In this paper, we focus on the modal analysis of the floor element. The experimental activities were designed with following goals: 1) collect experimental data for the validation of the numerical models, 2) familiarize experimentally with the WOODSOL elements and identify critical features, and 3) assess experimentally the vibroacoustic properties of the floor elements, of the connectors and their interaction.

2. Test objects

2.1 Woodsol floor element

The WOODSOL floor element is of type hollow box. The current cross section is shown in figure 1. The top and bottom plates are in the current design KERTO-Q plates with thickness 43 mm and 61 mm respectively. The thickness of the bottom flange is designed to fulfill fire safety requirements when the floor is installed without additional ceiling. The outermost stringers are glulam GL30c, while the inner ones are glulam GL28c [4]. The cavity can be filled with gravel as needed according to the acoustic requirements. The cross section as shown is designed for a span length of approximately 9 m to 10 m. We build prototype elements with the lengths 9 m, 4.7 m and 3.7 m. All of them have the same cross section to ease the comparison of the results. The filling with gravel varies. In table 1 an overview over the different configurations is given. The weigth of the 9 m floor element without gravel is 2.4 ton. The weight of the 4.7 m floor element is 1.2 ton without gravel and 2.4 ton with 100 kg/m^2 gravel in the cavity.

Table 1: Scheduled measurement program. Only the highlighted configurations are considered in this paper. Some of the configurations were described in the given references.

Floor length	Boundary conditions	Additional mass	Ref
9 m	**free-free**	**no**	[5]
9 m	clamped	no	[7]
9 m	simply supported	no	[7]
4.7 m	**free-free**	no + **gravel, 100 kg/**m^2	
4.7 m	**on columns**	no + **gravel, 100 kg/**m^2	
3.7 m	free-free	no + gravel, 100 kg/m^2	
3.7 m	on columns	no + gravel, 100 kg/m^2	

2.2 WOODSOL connector

One of the targets of the WOODSOL system is to realize a moment resisting frame without additional bracing. The key element of the system is beside stiff floor elements, the connection between floor elements and columns. The principle of the WOODSOL connector is based on a metal bracket installed to the floor element and to the columns using long threaded metal rods. The details are presented in [6]. In figure 2 the current prototype versions is shown. This was used to mount the floor elements to the columns.

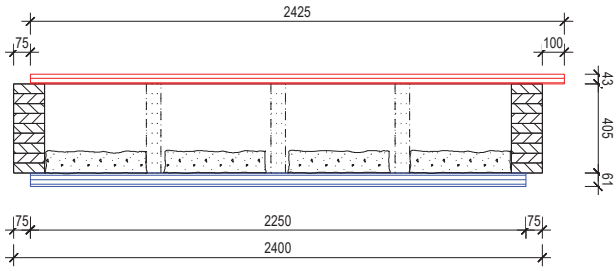

Figure 1: Cross section of the WOODSOL floor element [4].

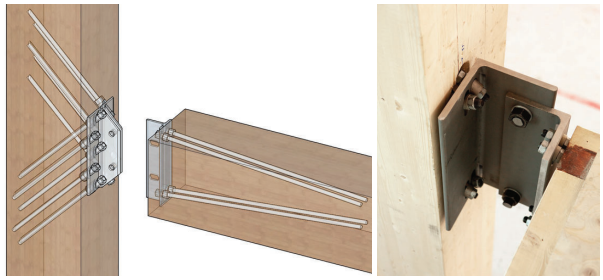

Figure 2: Woodsol connector concept (left,foto:Aivars Vilguts, NTNU) and picture of the connector installed between the columns and the floor element on the prototype (right, foto:SINTEF/A.- L. Bakken).

3. Experimental setup

Two different experimental setups were used to realize two types of boundary conditions: free-free boundary conditions and "*on columns*". Free-free boundary conditions were achieved by installing the floor element on top of air bellows. The setup is shown in figure 3a. The resonance frequencies of the floor on the bellows were 3 Hz to 6 Hz. This is at least 4 octaves below the first mode of the floor.
To realize the boundary condition "*on columns*", the WOODSOL building prototype was used. In the current configuration, two identical floor elements are mounted to six columns using one connector at each corner as shown in figure 2 and 3b. The two floor elements are not connected directly to each other. The columns were 5 m high 0.40 m x 0.45 m glulam elements. Their dimension is chosen according to the WOODSOL project requirements and takes into account both structural requirement and fire safety for a building up to eight stories. The floor is mounted with the bottom flange 2 m above ground.
The scheduled measurement program is shown in table 1. It includes several different configurations based on the three parameters: floor length, boundary conditions and additional mass. The measurements are still on-going while we are writing this paper so that only the highlighted configurations can be considered in this paper.

4. Experimental procedure and processing of the acquired data

The measurements were performed using the roving hammer technique with several accelerometers as a reference. On the 9 m floor, a grid with 10 x 5 points (size 0.56 m x 0.98 m) and 4 reference ac-

Figure 3: The two experimental setups: LEFT (a): Element L1 mounted on air bellows; setup used for the free-free BC measurements. RIGHT (b): Woodsol prototype ; setup used for the *on columns* BC measurements (foto:SINTEF/Anne-Line Bakken).

celerometers were used. On the 4.7 m floor, a grid with 9 x 5 points (size 0.55 m x 0.56 m) and 7 reference accelerometers were used. An impact hammer with soft rubber cap was used to excite the structure. At least three impacts at each point of the grid were recorded as time signals using a multichannel acquisition system. The time between impacts was approximately 10 s allowing for sufficient window length to avoid leackage. The data were post processed using the Abravibe toolbox [8] in Matlab. The first step here is the impact processing. The optimal settings for triggering level, pretrigger, block size and windowing of both the force and acceleration signal are defined with help of the abravibe toolbox graphical user interface. Then, the frequency response function (FRF) were built selecting manually the impacts to be used, after visual check of both the FRF and using the coherence function. The quality of the calculated FRFs is additionally checked by verifying the reciprocity of the FRFs at the reference points. The poles and the modal participation factors were computed using the polyreference time domain method. Based on the stabilization diagram, the reference positions that gave clearer mode functions were selected for the further steps. With the selected references, the poles were extracted. The AutoMAC criterion was used to asses how well the identified modes are decoupled and so check the quality of the modes identification. Finally the extracted mode shapes were checked visually for plausibility using the animation function of the toolbox [5] [9].

5. Measurement results

Figure 4 a) and b) show the amplitude of the measured transfer function acceleration/force for similar selected points on the 9 m and the 4.7 m floor both installed with free-free boundary conditions. The diagram a) shows the results for the 9 m floor which had no additional mass in the cavity. The diagram b) shows the results for the 4.7 m floor which had 100 kg/m^2 gravel in the cavity as additional mass. The diagram c) shows the amplitude of the measured transfer function acceleration/force for the same selected points on the 4.7 m floor with additional mass installed with different boundary conditions: in this case the floor is mounted on the columns. The numbers mark the identified modes and refers to the description to the right of the figure. The phase information is omitted for space reasons.
Figure 5 and figure 6 show the identified modes shapes for the configurations described above. For each mode shape, the frequency is given at which the mode shape occurs. Some of the mode shapes could not

be identified in either configuration and are marked with *n.a.* Damping considerations are omitted here for space reasons.

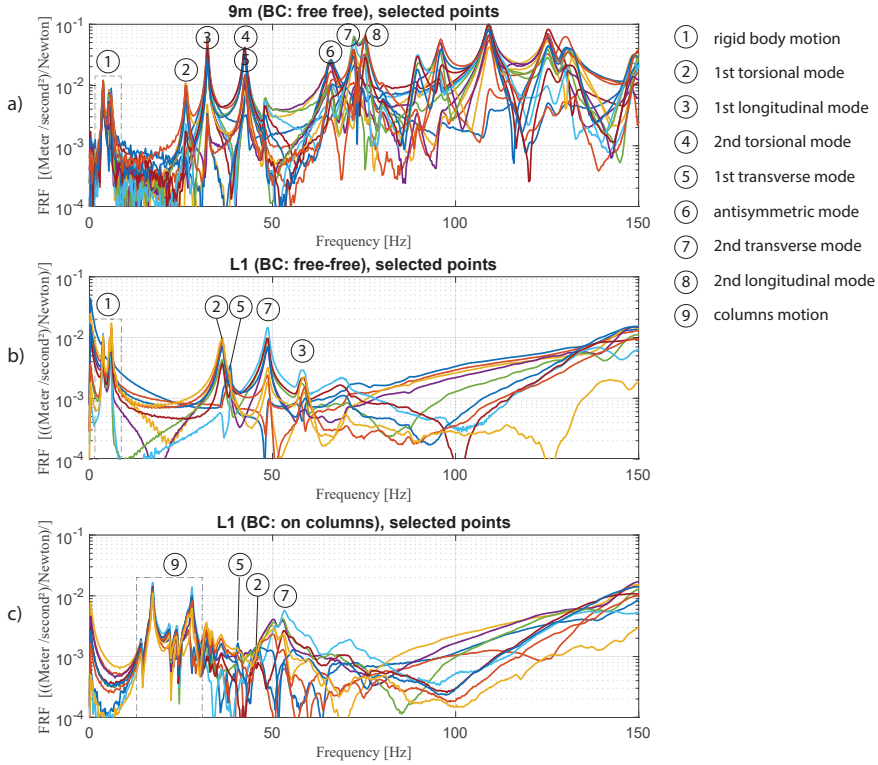

Figure 4: Measured frequency response functions (selected points) for the 9 m element without additional mass on air bellows (a), the 4.7 m (L1) element with additional mass on air bellows (b) and the the 4.7 m (L1) element with additional mass on columns (c).

6. Analysis and discussion

6.1 General observations

We would like to first highlight following general comments: 1) the choice of the reference accelerometer positions and the availability of several references was crucial to obtain the presented data. Only through an accurate choice of the measurement positions, it was indeed possible to distinguish the 2nd torsional mode and the 1st transverse mode on the 9 m floor with free-free boundary conditions. They appear indeed at almost identical frequencies: 42.1 Hz and 42.7 Hz respectively. The same applies for the first torsional mode (36 Hz) and the first transversal mode (38.5 Hz) of the 4.7 m floor with free-free boundary conditions. 2) When analyzing the data of the configurations with additional mass, the major limitations was posed by the large damping introduced in the system above approx. 60 Hz which made it nearly impossible to identify any mode above that frequency. 3) The measurement performed with the

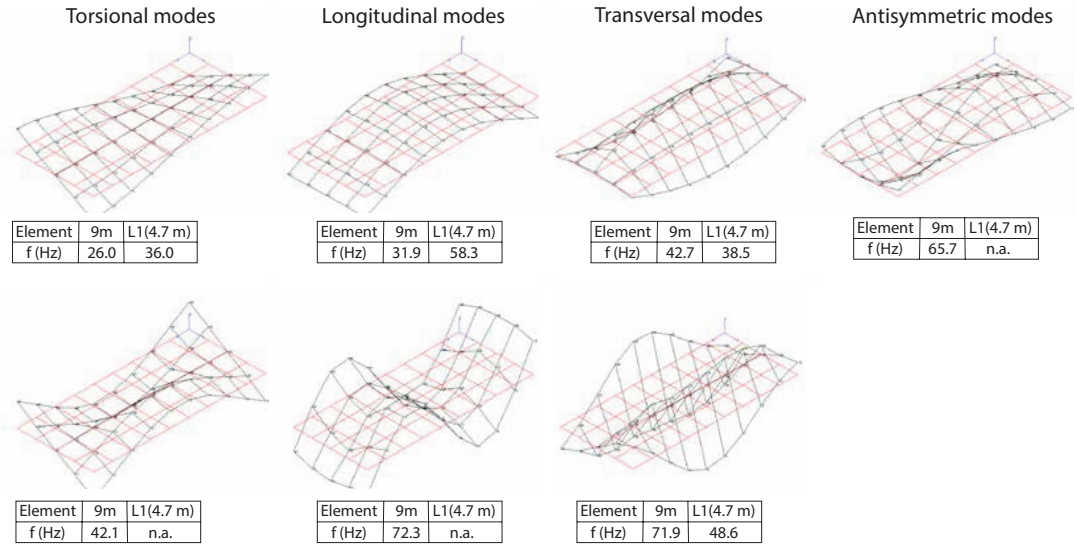

Element	9m	L1(4.7 m)
f (Hz)	26.0	36.0

Element	9m	L1(4.7 m)
f (Hz)	31.9	58.3

Element	9m	L1(4.7 m)
f (Hz)	42.7	38.5

Element	9m	L1(4.7 m)
f (Hz)	65.7	n.a.

Element	9m	L1(4.7 m)
f (Hz)	42.1	n.a.

Element	9m	L1(4.7 m)
f (Hz)	72.3	n.a.

Element	9m	L1(4.7 m)
f (Hz)	71.9	48.6

Figure 5: Identified mode shapes for the 9 m element and the 4.7 m (L1) element. Both elements were supported on air bellows (free-free boundary conditions).

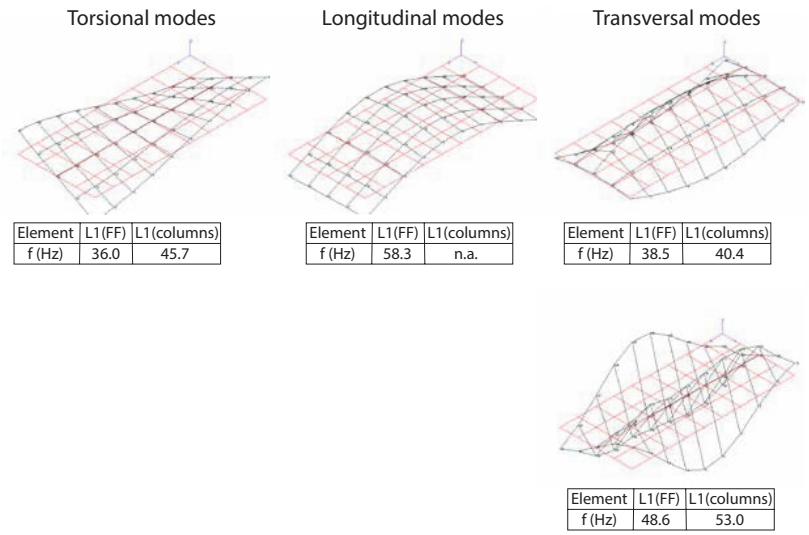

Element	L1(FF)	L1(columns)
f (Hz)	36.0	45.7

Element	L1(FF)	L1(columns)
f (Hz)	58.3	n.a.

Element	L1(FF)	L1(columns)
f (Hz)	38.5	40.4

Element	L1(FF)	L1(columns)
f (Hz)	48.6	53.0

Figure 6: Identified mode shapes for the L1 element (4.7 m) mounted in two different ways: on air bellows (free-free boundary conditions) and on columns using the WOODSOL connectors.

floor elements mounted on the columns show that the dynamic of the undamped columns largely dominates the measured frequency response. This posed a challenge to the analysis of the floor properties and calls for an improvement of the setup.

6.2 Effect of additional mass

The comparison of the measured response functions shown in figure 4 a) and b) allows to gain insights in the effect of additional mass. A careful approach is required though, since we are changing two parameters at once: length and additional mass. Nevertheless the effect of the change in length can be predicted fairly well so that a clear interpretation of the data is possible.
The frequency of the first torsional mode is 26.0 Hz and 36.0 Hz for the 9 m and 4.7 m floor respectively. This is probably due to the increased stiffness when the end beams come closer reducing the length of the element. The first longitudinal mode almost doubles in frequency when halving the length: the frequency is 31.9 Hz with 9 m length and 58.3 Hz with 4.7 m. The small shift towards lower frequencies by half length (58.3 Hz instead of 63.8 Hz) is probably due to the additional mass. The transversal modes are expected not change significantly when reducing the length, but they do. This is hence probably an effect related to the additional mass.
The most obvious effect of the additional mass is observed above 60 Hz: here the peaks are so largely damped that individual modes cannot be identified any longer. Moreover the broader peaks in the FRFs with additional mass suggest an increased damping in the floor also below 60 Hz. See for instance the peak marked with the number 2 and 3 in figure 4 a) and b).
The measurements show that the amplitude of the FRFs is reduced by more than 10dB above 60 Hz nearly broadband and that below 60 Hz the FRFs peaks are reduced by up to 7 dB. The amplitude of few modes (e.g. the first torsional mode) is not affected at all by the additional mass.
The expected influence of these effects on the impact sound insulation can be summarized as follow: above 60 Hz we expect the sound insulation to be largely improved by the additional mass, in a measure comparable to the reduction in amplitude of the transfer functions. The effect at lower frequencies is less obvious to estimate since the effects are different for different modes. The sound radiation properties of the different modes need to be considered. This will be done in the next step of our analysis, which will also allow to confirm the expectation on the improvement of the sound insulation above 60 Hz.

6.3 Effect of the mounting to the columns

The results showing the effect of the differenct boundary conditions are presented in figure 4, diagrams b) and c).
Despite the limitations stated above, some modes could be clearly identified with the measurements and some effects could be observed. In general, the FRFs have a lower amplitude when the floor is mounted to the columns. The effect is very dependent on the single FRF, but a general reductions of about 5 dB in the frequency range 50 Hz to 150 Hz can be stated. The broader peaks suggest a higher damping in the system. Single peaks are reduced by as much as 10 dB.
The scheduled measurements with an improved setup will show if the modes which were not identified are eliminated by the boundary conditions or if this was only an effect of the superimposing dynamic of the floor and the columns.
The observed effects are expected to improve the impact sound insulation at low frequencies, but it is not possible to give a quantitative answer with the collected data. The planned further activities will probably give better answers.

7. Conclusions and further work

The measurements performed gave a good insight in the effect of additional mass in the cavity of the floor elements. This effect is most pronounced above ca. 60 Hz where single modes cannot be observed any longer and the amplitude of the FRFs is about 10 dB lower with additional mass compared to no additional mass. Below this frequency an increased damping is observed. Further measurements are planned on a 4.7 m floor element without additional mass to confirm these results.
The measurements performed on the columns gave a first impression of the effect of this boundary conditions: additional damping is inserted in the system and some of the modes are shut down. Unluckily the dynamic of the whole setup limited the achievable analysis. An improvement of the setup is currently under study. Target of the improvement will be to reduce the dynamic of the columns at least to the level that is expected in the full constructions system.
In general we can conclude that both the additional mass and the boundary conditions influence positively the improvement of impact sound insulation, either introducing damping in the system, reducing the amplitude of the vibrations in the system or eliminating some of the vibration modes.

Acknowledgement

This project has been carried out within the Woodsol project (http://www.Woodsol.no), which is funded by the Norwegian Research Council. The colleagues at NTNU S. Nesheim and A. Vilguts were involved in the design and construction of the WOODSOL prototype and L. J. Lassesen greatly supported us during the construction of the prototype at Charlottenlund videregaende skole in Trondheim (NO).

REFERENCES

1. Woodsol project summary, http://www.woodsol.no.
2. Homb, A., Conta,S., *Strategies to evaluate acoustic properties of timber hollow box floors* , Internoise 2019, Madrid, June 16-19, 2019 (Abstract submitted).
3. Conta, S., Homb, A., *Challenges and limitations using the Integral Transform Method to obtain the impact noise level of timber floors*, in Proceedings of Euronoise 2018, M. Taroudakis (Ed.), Crete, May 27-31, 2018 (pp.: 667-674), ISSN: 2226-5147.
4. Halstedt, H., *Woodsol prototype element production drawings*, SINTEF Byggforsk, Trondheim, NO (2018).
5. Conta, S., *Experimental modal analysis on Woodsol prototype floor element*, NTNU internal report, Trondheim, Norway (2017).
6. Malo, K. A., Stamatopoulos, H., *Connections with threaded rods in moment resisting frames*, In Proceeding of the World Conference on Timber Engineering, IBSN 978-3-903024-35-9. Eberhardsteiner, J., Winter, W., Fadai, A., and Poell, M. (eds.), pp. 168-176, Wien, Austria. 2016.
7. Bjorge, V., Kristoffersen, T., *Konseptstudie av trebaserte kompositttdekker med mulighet for innspenning til limtresoyler*, Master thesis, NTNU, 2017.
8. Brandt, A., *Notes On Using the ABRAVIBE Toolbox for Experimental Modal Analysis*, http://www.abravibe.com.
9. Brandt, A., *Noise and Vibration Analysis, Signal Analysis and Experimental Procedures*, John Wiley and Sons, (2011).

Paper #2

Paper #2

Errata corrige:
Equation 10 should be corrected to:

$$K[\alpha\beta\gamma] = \frac{k_A[\gamma]}{\sqrt{(k_A[\gamma]^2 - k_x[\alpha]^2 - k_y[\beta]^2)}} \tag{A.1}$$

In Equation 14, L'_n should be corrected to L_n.
Equation 15 should be corrected to:

$$L_n = L_W - 4 \text{ (dB)} \tag{A.2}$$

The results presented in figure 9 needs to be corrected accordingly. Figure A.1 shows the corrected version.

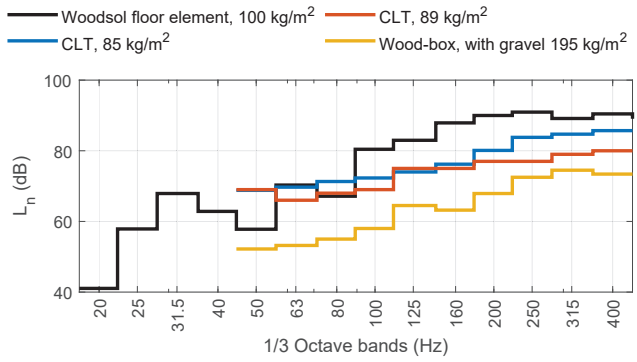

Figure A.1. Corrected version of figure 9 in *Paper #2*. It shows the impact noise level determined for a 9 m empty Woodsol floor element compared to literature data for objects with similar mass per unit area.

Challenges and limitations using the Integral Transform Method to obtain the impact noise level of timber floors

Simone Conta, Anders Homb
Department of Civil and Environmental Engineering, NTNU, Trondheim, Norway

Summary
The Woodsol project aims at developing long span lightweight floors based on a wood-box concept for timber buildings with high architectural flexibility. The major challenge regarding impact sound insulation is expected to be at low and medium frequencies. The impact noise level of the building element needs to be measured but no building acoustics laboratory offers an opening with a size of 8 to 10 m. For this reason, we intend to use the Integral Transform Method (ITM) to determine the impact noise level. The input to the ITM is the measured vibration velocity on the building element. Based on the spatial Fourier transformation, the ITM can be used to calculate the radiated sound power in the wave number domain. From that, the impact noise level is calculated. The result shall be comparable with results obtained performing measurements according to the relevant standards. Preliminary measurements were performed on a prototype floor. Assessment of the measured vibration levels and calculated impact noise levels will be given. The practical challenges and limitations encountered so far will also be addressed and discussed in this paper.

PACS no. 43.40.+s, 43.58.+z

1. Introduction

This paper describes measurements performed on a Woodsol prototype floor element. The design of the element is based on the wood-box concept. The section of the floor element is shown in figure 1. The upper and bottom plate are laminated veneer lumber of type Kerto-Q, while the stringers are glulam. This type of construction was chosen to fulfil the requirements set by the project. The floor shall span at least 9 m and contribute to the structure of the building with high stiffness. The fire resistance requirements set the minimum thickness of the bottom plate. Goal of the measurements is to asses the acoustic properties of this construction as a starting point for further development.

Considering the lightweight properties of the floor element and its size, the major challenge regarding impact sound insulation is expected to be at low and medium frequencies. Common building acoustics laboratories have openings sizes with dimensions of about 3 m x 4 m. We therefore need to use an alternative measurement method to determine the impact noise level of the floor element. The Integral Transform Method (ITM) is gaining popularity and appeared to be a suitable tool. Although a number of references are available on the ITM, its application is not straightforward and requires an accurate planning of the measurements and a comprehensive analysis of the acquired measurement data. In this paper, after briefly recalling the basic elements of the theory behind the ITM, we present the procedure we followed to set up and carry out the measurements. We will also present preliminary results and some considerations about the validity of the data.

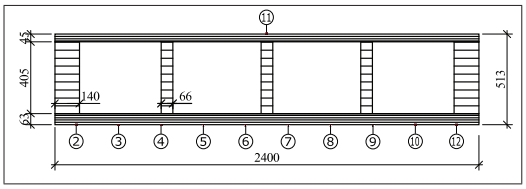

Figure 1. Cross section of the Woodsol floor element under investigation. The numbers indicate the positions of the accelerometers.

2. Theory and procedure

The ITM has its foundation in the wavenumber transform and the description of the plane radiators as sum of plane wave [1]. For the current work following references were mainly used: for the implementation we

referred to the PhD thesis of Mathias Kohrmann [2] while for the measurement setup, the work of Stefan Schoenwald [3] and Christoph Winter [4] have been important sources.
In the following, we shall recall the steps and the equations, which are needed to define a proper measurement setup and implement the method in e.g. Matlab. We will also highlight the elements that are necessary for a reliable measurement setup.

2.1. Basic quantities

We will first recall some relations for a number of basic quantities for easier reference.
The bending wave speed c_B in the material is the governing quantity. We are dealing here with engineered timber products (Kerto-Q) with orthotropic material properties, which means that the bending wave speed is different in the x and y direction (c_{bx}, c_{by}). Following relations hold :

$$c_{bx}(f) = (2\pi f)^{1/2}\left(\frac{B'_x}{\rho h}\right)^{1/4} \tag{1}$$

$$c_{by}(f) = (2\pi f)^{1/2}\left(\frac{B'_y}{\rho h}\right)^{1/4} \tag{2}$$

with f frequency, B bending stiffness of the structure/plate, ρ density of the material and h height of the structure/plate.
The basic relations between wavelength λ, wavenumber k, frequency f and bending wave speed c_b are:

$$k_x = \frac{2\pi}{\lambda_x} \qquad k_y = \frac{2\pi}{\lambda_y} \tag{3}$$

$$\lambda_x f = c_{bx} \qquad \lambda_y f = c_{by} \tag{4}$$

We shall also recall here the relation for the critical frequency f_c:

$$f_c = \frac{c_0^2}{2\pi}\sqrt{\frac{m''}{B'}} \tag{5}$$

2.2. Measurement grid size

The first step in the ITM method is to measure the vibration velocity distribution on the plate. Since the method is essentially based on a 2-D wavenumber transform, the *Shannon*-Criterion (also known as the *Nyquist*-Theorem) sets the requirement on the grid size. Following relations hold between between raster size Δx, Δy, minimum wavelength λ_{min} and maximum frequency f_{max}

$$\Delta x < \frac{\lambda_{min}}{2}, \qquad \Delta y < \frac{\lambda_{min}}{2}, \tag{6}$$

$$f_{max} < \frac{c_{bx}(f_{max})}{2\Delta x} \qquad f_{max} < \frac{c_{by}(f_{max})}{2\Delta y} \tag{7}$$

Since in the ITM the calculations are carried out in frequency steps, it is not necessary to filter the signal before performing the wavenumber transform. Nevertheless it is necessary to check that no strong peaks with their side lobes are too close to the aliasing limits. This can be easily checked in the wavenumber transform spectra.
The conditions on the grid size imply a high number of measurements points. To reduce the measurement time one can use the geometrical symmetry of the test obejct. Symmetry can be used only up to a certain extent. Winter [4] showed that performing the measurements only on 1/4 of the plate led to an overestimation of the radiated sound power, due to the introduced leakage. Performing the measurements on 1/2 deck might lead to acceptable results, but this needs to be confirmed.
The frequency range of interest for this work is 20 Hz to 200 Hz. Due to the lack of experience with the method and the uncertainties in determining c_{bx} and c_{by}, the raster size was set to 24 cm in x direction and 30 cm in y direction. This should allow to obtain reliable measurements data up to at least 400 Hz.
In the table I, we list several key quantities, compared with similar experiments found in literature. To determine c_b, we used the tabulated Young modulus and density values for Kerto-Q combined with the actual geometry of the deck for the calculation of the bending stiffness. This is a rather rough approach and we shall verify later if it was appropriate or not.

2.3. Calculation of the radiated sound power

At each point of the grid the vibration velocity is converted from the time domain to the frequency domain using a common Fourier Transform. The input data to the integral transform method are now available and can be processed using a two dimensional Fourier Transform (the wavenumber transform) to obtain the radiated sound power. According to [2], the frequency dependent radiated sound power $P(f)$ can be calculated from the measured velocity pattern of a plane radiator in the wave number domain with following relation:

$$P(f) = \frac{1}{2}\frac{\rho_A c_A}{4\pi^2}\Re\Bigg[\int_{-\infty}^{\infty}\int_{-\infty}^{\infty} \frac{k_A(f)}{\sqrt{k_A(f)^2 - k_x^2 - k_y^2}}|\hat{v}(k_x, k_y, f)|^2 dk_x dk_y\Bigg] \tag{8}$$

where following symbols are used:

- $P(f)$ radiated sound power at the frequency f,
- ρ_A density and c_A speed of sound in the air,
- $k_A = \frac{2\pi f}{c_A}$ wavenumber of air,
- k_x and k_y the wavenumbers in x and y direction,
- $\hat{v}(k_x, k_y, f)$ the complex vibration velocity distribution in the wavenumber domain.

Table I. Key quantities for the current setup compared to the reference setups.

Ref.	Material, thickness	Raster size		Bending wave speed @ f_{max}		Nyquist frequency		Critical frequency	
		Δx	Δy	c_{bx}	c_{by}	$f_{max,xdir}$	$f_{max,ydir}$	$f_{c,x}$	$f_{c,y}$
-	Kerto-Q, 63 mm	24 cm	30 cm	645 m/s	867 m/s	1350 Hz	1450 Hz	375 Hz	223 Hz
[3]	CLT, 80 mm	11 cm	11 cm	901 m/s	550 m/s	4100 Hz	2500 Hz	584 Hz	955 HZ
[4]	Gypsum board, 2x 12,5mm	25 cm	25 cm	189 m/s		380 Hz		1224 Hz	
[3]	Steel, 1mm	4 cm	3 cm	116 m/s		1500 Hz		12800 Hz	
[2]	Aluminium plate, 2 mm	6 cm	6 cm	162 m/s		1350 Hz		6000 Hz	

It is necessary to transform this analytical expression into a discrete formulation, in order to use it with measurement data (see [2] for details). $P(f)$ assumes the form of a vector $\mathbf{p}$ with dimension $n_f \times 1$, $K(k_x, k_y, f)$ and $\hat{v}(k_x, k_y, f)$ assume the matrix form $\mathbf{K}$ and $\hat{\mathbf{V}}$ with dimensions $M_\alpha \times M_\beta \times n_f$. The individual terms of $\mathbf{p}$ at the frequency step γ have the form:

$$P[\gamma] = \frac{1}{2}\frac{\rho_A c_A}{4\pi^2}\Re\Bigg[\sum_{\alpha=1}^{M_\alpha}\sum_{\beta=1}^{M_\beta} K[\alpha,\beta,\gamma]\cdot|\hat{v}[\alpha,\beta,\gamma]|^2\Delta x^2\Delta y^2\Bigg]\Delta k_x \Delta k_y \quad (9)$$

where following symbols are used:

- α and β coordinates in the wavenumber domain,
- $M_\alpha = z_p\frac{l}{\Delta x}$ and $M_\beta = z_p\frac{w}{\Delta y}$ number of samples in the wavenumber domain,
- z_p zero padding factor (see section 2.4),
- $l \times w$ dimensions of the plate,
- $\Delta k_x = \frac{2\pi}{z_p l}$ and $\Delta k_y = \frac{2\pi}{z_p w}$ the sampling interval in the wavenumber domain.

The terms of the matrix $\mathbf{K}$ are:

$$K[\alpha\beta\gamma] = \frac{k_A[\gamma]^2}{\sqrt{(k_A[\gamma]^2 - k_x[\alpha]^2 - k_y[\beta]^2)}} \quad (10)$$

The derivation of the individual spectral amplitudes $\hat{v}[\alpha,\beta,\gamma]$ from the vibration velocity pattern in the spatial domain $v[r,s,\gamma]$ (with r and s spatial coordinates) is a key point in the procedure. This is done through a two dimensional Fourier Transform on the vibration velocity pattern in the spatial domain for each frequency step.

2.4. Zero padding

Zero padding is a simple technique used in signal processing to increase the length of a measured signal and hence the resolution of a Fourier Transform. It consists in appending zeros to a signal. The zero padding factor z_p is defined as:

$$z_p = \frac{M}{N} \quad (11)$$

where N is the original length of the signal in samples and M the resulting length, after appending the zeros.

It is is very important to notice here, that while using *zero padding* we increase the resolution of the Fourier Transform, but we are not adding any information to the signal. All the information that is available is the one which could be described with the original resolution. The purpose of using the zero padding technique in the ITM is to achieve a better resolution of the boundaries of the plate. The typical side lobes in the wavenumber spectrum are due to the to the finite size of the plate. From a mathematical point of view, they are due to the sinc function corresponding to the square window describing the finite size of the plate. The higher the resolution, the steeper is the sinc function and the sharper is the description of the finite size of the plate. While using the ITM, one has to choose a value of z_p *high enough* to take this effect properly into account. We are showing an example of this in section 4.2.
In addition to this, a high *zero padding* factor is used to solve some numerical issues related to the $\mathbf{K}$-matrix [2]. Preliminary checks showed that the value of $z_p = 50$ used in the current analysis was adequate. Nevertheless we shall verify in our further work this choice, by implementing more advanced thechniques as shown in [2].

2.5. Calculation of the impact noise level

The target of this work is to obtain impact noise level data which are comparable with data obtained from measurements carried out according to the standard ISO16283-2 [5]. As a first approximation, we will use the relation that a sound source with sound power L_W generates a sound pressure level L_i under the assumption of diffuse field as follow, [7]:

$$L_i = L_W - 10log\frac{p_{ref}^2 \cdot 55.3 \cdot V}{P_{ref}\cdot 4\rho c^2 \cdot T_{60}} \quad (12)$$

$$= L_W - 10log\frac{V}{V_0} + 10log\frac{T_{60}}{T_0} + 14dB. \quad (13)$$

According to the standard [5], the normalized impact sound pressure level is calculated as:

$$L'_n = L_i + 10log\frac{A}{A_0}. \quad (14)$$

Combining 13 and 14 we obtain a relation that does not depend on V, T and A:

$$L'_n = L_w - 12dB \quad (15)$$

Figure 2. Woodsol floor element installed on air bellows.

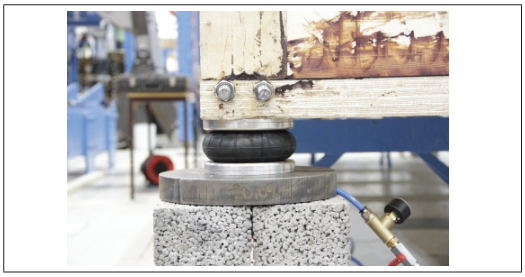

Figure 3. Detail of the supporting air bellows.

The measurement standard requires to measure the sound pressure level at a certain distance from the boundaries. Similarly to what is done in the ISO15186 [6], the *Waterhouse correction* [8] can be used to compensate for this effect :

$$W = \frac{\hat{p}_\infty^2}{4\rho_0 c_0} A\left(1 + \frac{Sc_0}{8Vf}\right) \tag{16}$$

Typical values to use these relation were taken from ISO15186 [6].

3. Experimental setup

3.1. Test object

The procedure described above was used to calculate the normalized impact noise level in the current work. The measurements data were collected using an experimental setup which was dedicated to a modal analysis with free-free boundary conditions. The floor element was mounted on air bellows with the rigid body motion having a frequency of about 3 Hz to 5 Hz. Figure 2 shows the floor element mounted in the lab, including a detail of the mountings with the air bellows.

It is mandatory to highlight here that these boundary conditions are not representative for a typical situation in a building and that the radiated sound power is certainly influenced by this situation. While the absolute value of the radiated sound power might be compromised by this aspect, the considerations about the measurement method are still valid.

The sensors position are shown in figure 1 on the cross section of the element. We used a 12-channel OROS analyser and decided to have 10 accelerometers mounted on a line along the y-direction ($\Delta y = 0.24m$). The measurement line was then moved along the x-direction of the floor ($\Delta x = 0.30m$) while keeping one accelerometer (number 11) fixed for phase reference. The measurements were performed on half deck and the calculated radiated sound power then corrected to the full size of the floor element ($+3dB$).

The accelerometers were mounted using special wooden screws to ensure proper connection of the sensor with the structure.

3.2. Excitation

We used following excitation types: impact hammer and tapping machine. The impact hammer gives the possibility to measure the force and evaluate the transfer functions. The tapping machine was used with the aim of obtaining sound power levels comparable with the lab measurements. The tapping machine was placed at four different positions following the requirement of ISO 16283-2. The impact hammer was used at the same positions as the tapping machine, hitting at the locations of each hammer of the tapping machine.

3.3. Effect of the direct airborne excitation

The measurements of the vibration velocity were performed with the floor element installed in a large industrial hall. There was no separation between the volume above the floor element and the volume below it. This means that the tapping machine could excite the bottom plate in two ways: the expected structure-borne sound due the impact of the hammers and the vibration propagation through the structure and the unwanted airborne sound excitation of the bottom plate due to the sound pressure radiated directly from the upper plate and propagating through the hall.

Preliminary measurements showed that the vibration level generated by the airborne sound excitation is approximately 10 dB lower than the structure-borne excitation but they also showed that this aspect must be taken into account because it might have a relevant effect. Further work is being carried out to better asses this topic.

4. Preliminary results

4.1. Vibration velocity in the wavenumber domain

In figure 4, we show the vibration velocity $|\hat{v}|^2$ distribution for the frequency steps 32 Hz (first bending

mode), 42 Hz (first transversal mode combined with a torsional mode) and 66 Hz (higher order mode). Note that the measured data were mirrored here for the purpose of visualization. In the figure, the excitation positions are marked with white circles while the current active excitation position is highlighted in red. The results match fairly well the frequencies and mode shapes obtained from the experimental modal analysis performed on the same experimental setup.

In figure 5 and 6, we show the vibration velocity $|\hat{v}|^2$ spectra in the wavenumber domain for the first bending mode (32 Hz) and for the frequency step 42 Hz. The black ellipse in the diagrams represents the bending wave speed at the respective frequency calculated using the tabulated data for Kerto-Q. The white circle represent the wavenumber of air k_{air} for this frequency, while the white area highlights the portion of energy that contributes to the radiated sound power.

In figure 5, the main peaks have coordinates k_y close to 0 and $k_x \approx 0.9$. $k_y \approx 0$ corresponds to the fact that the motion related to this mode is aligned with the x axis of the floor element. Similarly in figure 6, $k_x \approx 0$ due to the fact that the mode is along the y axis. The pattern in figure 6 is less clear then in the previous figure, because at this frequency step two vibrational modes are active and the resolution used is not high enough to distinguish the two modes. Results from the experimental modal analysis performed on the same experimental setup showed the first transversal mode at 42.7 Hz and a torsional mode at 42.1 Hz.

In contrast to the common time/frequency Fourier Transform, it is useful here to present the periodical repetition of the Fourier Transform results. The main peaks indeed are expected to lay on a circle (in the case of an isotropic material) or an ellipse (as here, with an orthotropic material), which has the radius corresponding to the associated wavenumber. Knowing the wavenumber and the frequency, it is possible to calculate the bending wave speed. The currently calculated bending wave speed matches only very roughly the measured data. In our further work, we shall use these data to calculate the bending wave speed for the element following the procedure described in [4] and find an improved estimate of the expected bending wave speed. A typical feature of the wavenumber spectra related to finite vibrating plates are the side lobes of the peaks. In our application, they are of utmost importance because they carry part of the information of the radiated sound power. Indeed only the part of the spectrum within the circle with radius k_A (highlighted with the white shading in the figures) contributes to the sound radiation.

Finally, it is worth pointing out here that one should not expect to see a wavenumber spectrum which is perfectly point-symmetrical around the origin. The input to the wave number transform is indeed the complex velocity field. The wave number transform is essentially a 2-D Fourier transform. For a complex signal its output is not symmetrical around the origin.

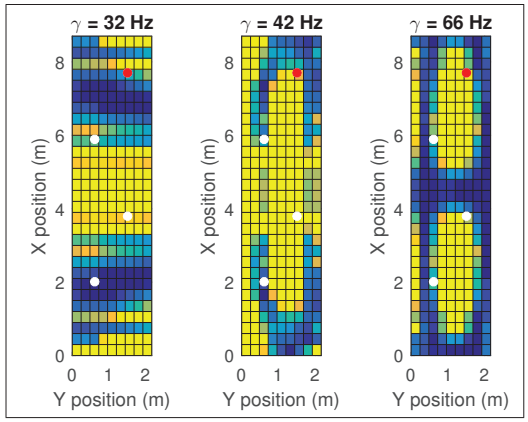

Figure 4. Measured vibration velocity $|v|^2$ distribution. The data were measured on only half deck and are here displayed mirrored. The positions of the tapping machine are marked with the white circles. The red circle indicate the current excitation position.

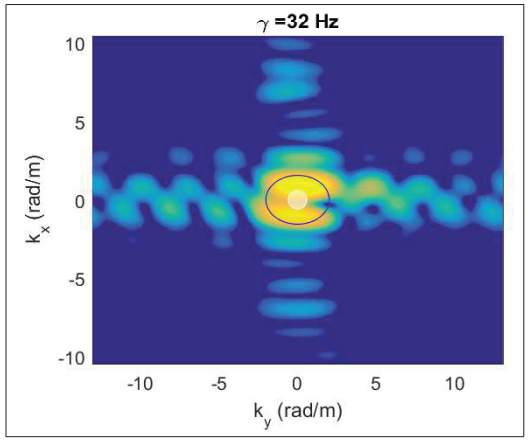

Figure 5. Wavenumber spectrum of the vibration velocity $|v|^2$ for the frequency step $\gamma = 32Hz$. The black ellipse corresponds to the bending wave speed calculated using the tabulated data for Kerto-Q. The white circle represents the wavenumber of air k_{air} for this frequency. The white area inside the circle highlights the contributions to the radiated sound power.

4.2. Effect of zero padding factor

In figure 7 we show the calculated radiated sound power using different values of the *zero padding* factor. With very low values of zero padding ($z_p = 2$) the procedure does not produce stable results because of numerical issues. Increasing z_p from 20 to about 50 the

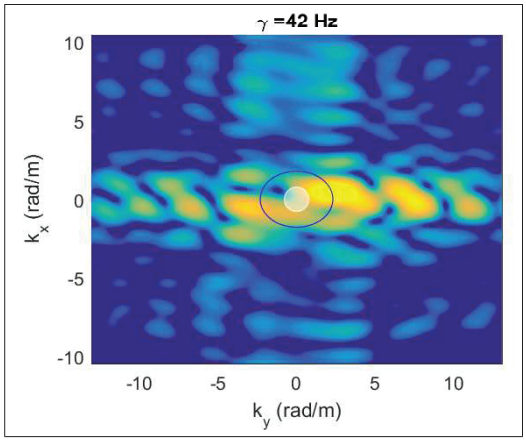

Figure 6. Wavenumber spectrum of the vibration velocity $|v|^2$ for the frequency step $\gamma = 43Hz$. The black ellipse corresponds to the bending wave speed calculated using the tabulated data for Kerto-Q. The white circle represents the wavenumber of air k_{air} for this frequency. The white area highlights the contributions to the radiated sound power.

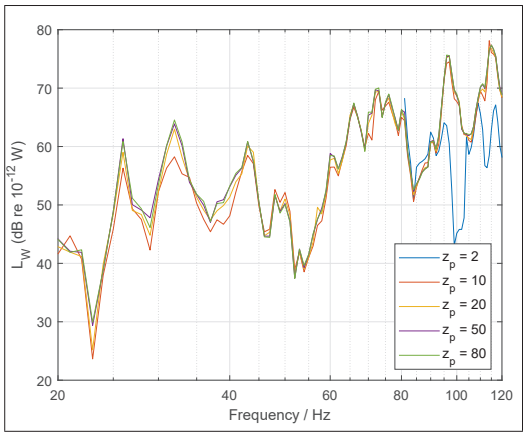

Figure 7. Sound power level calculated with varying *zero padding* factor. The results are shown in the frequency range 20 Hz - 120 Hz for the excitation with tapping machine at one position.

results stabilize at a certain level. Further increasing the zero padding factor does not change the results. For the further calculations we chose to use $z_p = 50$.

4.3. Radiated sound power and impact noise level

The measurement results obtained for the radiated sound power L_W are shown in figure 8. In the diagram the curves obtained for the different excitation positions are shown along with the energetic average. The normalized impact noise level calculated from the energetic average of the measured sound power is shown

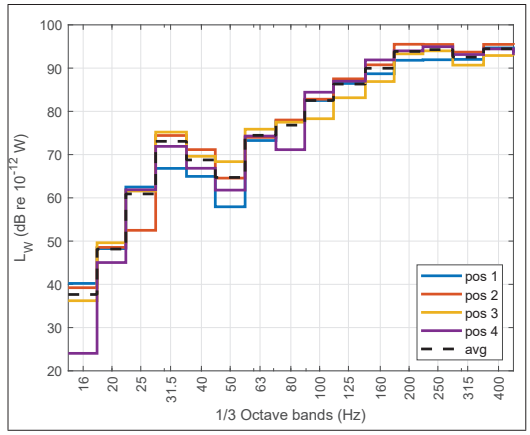

Figure 8. Sound power level calculated from excitation with tapping machine at four different positions.

in figure 9 in 1/3-octave bands up to 400 Hz. The local maxima around the eigenfrequency of the first mode (32 Hz) confirm the expectation that the long span might lead to characteristic features in the spectrum at low frequencies.

For reference we show in the same diagram the normalized impact noise level measured in a lab for three more constructions: two CLT floor elements with similar mass per unit area (m' = 85 kg/m^2 and m' = 89 kg/m^2) [9] and a wood-box construction filled with gravel (m' = 195 kg/m^2) [10]. Unluckily the datasets available only showed frequencies above 50 Hz. The results show that normalized impact noise level for the Woodsol element above 100 Hz is very similar to that for a CLT panel of comparable mass per unit area. The strong differences below 100 Hz could be due to the boundary conditions, the size of the element and the stiffness properties of the design. We will need to confirm this result.

5. Conclusions

In this paper we described the usage of the integral transform method on a prototype floor element. We highlighted the challenges encountered and a few limitations that we faced. All relevant equations, which are needed to define the parameters of the experimental setup and to implement the method in a computer program were given for ease of reference and further usage in the work to come.

The preliminary results were obtained using a tapping machine at four different position as excitation.

From the measured vibration velocity, we calculated the radiated sound power and corrected this so that it should be comparable with data obtained following the measurements procedure described in ISO16283-2. The preliminary results show that above 100 Hz the normalized impact noise level is comparable to that

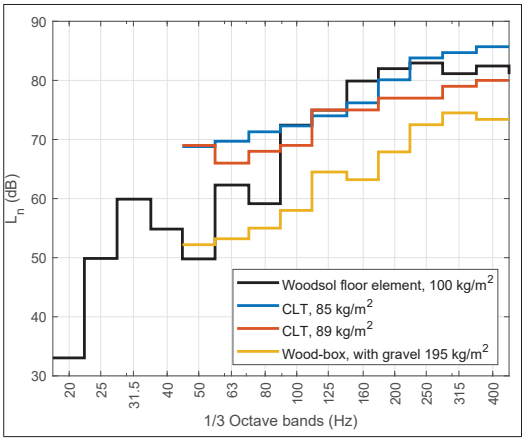

Figure 9. Impact noise level calculated from vibration velocity measurements on the Woodsol floor element (m' = 100 kg/m^2). For comparison three more constructions are shown in the diagram: two CLT floor elements with similar mass per unit area (m' = 85 kg/m^2 and m' = 89 kg/m^2) [9] and a wood-box construction filled with gravel (m' = 195 kg/m^2) [10] .

of a CLT element with similar mass per unit area. At low frequencies, special features were observed that could be due to the boundary conditions, the size of the element and the stiffness properties of the design. Further work is needed to fully understand and validate these results.

Acknowledgement

This project has been carried out within the Woodsol project (http://www.Woodsol.no). Woodsol is funded by the research council of Norway and the consortium partners.

References

[1] Cremer, L., M. Heckl, and B.A. Petersson, Structure-borne sound: structural vibrations and sound radiation at audio frequencies. 2005: Springer.

[2] Kohrmann, M., Numerical Methods for the Vibro-Acoustic Assessment of Timber Floor Constructions, in Ingenieurfakultaet Bau Geo Umwelt (BGU) 2017, Technische Universitaet München.

[3] Schoenwald, S., S. Vallely, and H.-M. Troebs, Advanced methods to determine sound power radiated from planar structures. The Journal of the Acoustical Society of America, 2017. 141(5): p. 3713-3713.

[4] Winter, C., Messtechnische Untersuchung leichter Deckentragwerke im Wellenzahlbereich und Prognose der abgestrahlten Schallleistung, in Lehrstuhl fuer Baumechanik. 2012, Technische Universitaet München.

[5] ISO 16283-2:2015, Acoustics – Field measurement of sound insulation in buildings and of building elements – Part 2: Impact sound insulation

[6] ISO 15186-1:2000, Acoustics – Measurement of sound insulation in buildings and of building elements using sound intensity – Part 1: Laboratory measurements

[7] Jacobsen, F., Fundamentals of Acoustic and Noise Control, Lecture note, 2005, DTU.

[8] Vigran, T.E., Building Acoustics. 2008: Taylor and Francis.

[9] Homb, A., C. Guigou-Carter, and A. Rabold, Impact sound insulation of cross-laminated timber/massive wood floor constructions: Collection of laboratory measurements and result evaluation. Building Acoustics, 2017. 24(1): p. 35-52.

[10] Berner Fachhochschule, Prüfbericht A2. Def 4.1, 2013

Paper #3

Paper #3

Errata corrige:

Figure 10: the label of the vertical axis of the 4 graphs should indicate k_x instead of k_y.

Applied Acoustics 169 (2020) 107457

Contents lists available at ScienceDirect

Applied Acoustics

journal homepage: www.elsevier.com/locate/apacoust

Benchmarking the vibration velocity-based measurement methods to determine the radiated sound power from floor elements under impact excitation

Simone Conta [a,*], Andrea Santoni [b], Anders Homb [a,c]

[a] NTNU, Department of Civil and Environmental Engineering, 7491 Trondheim, Norway
[b] Università degli Studi di Ferrara, Dipartimento di Ingegneria, 44122 Ferrara, Italy
[c] SINTEF Community, 7465 Trondheim, Norway

ARTICLE INFO

Article history:
Received 26 March 2020
Received in revised form 26 May 2020
Accepted 26 May 2020

Keywords:
Radiated sound power
Building acoustic
Rayleigh integral method
Integral transform method
Impact sound insulation
Discrete calculation method

ABSTRACT

The Rayleigh Integral Method, the Integral Transform Method and the Discrete Calculation Method are all vibration velocity-based measurement methods to determine the radiated sound power from planar objects. Even though all these three methods are based on a well-established theoretical background, which has been known for long time, they are only now gaining popularity in the building acoustics field and the building acoustics community is still rather new to them. They offer advantages compared to the standard methods specially in the low frequency range or on special applications with articulated boundary conditions. In this paper, we want to summarize the three methods in one place to highlight their different theoretical foundations. We present a numerical benchmark of these three methods, based on a simple panel with varying boundary conditions, highlighting similarities and differences between them. In a second step, we compare the radiated sound power levels obtained by the three methods with results obtained by a standard measurement procedure according to the ISO 10140-3, under excitation by an ISO tapping machine. Finally, we present the application of the methods to determine the *in-situ* impact noise level of a floor structure: a complex system with challenging boundary conditions. The results show a good agreement between all the tested methods, as long as the respective requirements are satisfied. The results also demonstrate how the vibration velocity-based measurement methods can have a broader application compared to the standard laboratory method and deliver additional information on complex test objects.

1. Introduction

Building acoustic measurements are generally carried out according to appropriate standards. When looking at the impact sound insulation the relevant standards for laboratory measurements is the ISO 10140-3 [1]. The well-known measurement method described therein is based on impact excitation by means of an ISO tapping machine and measurement of the sound pressure level in the receiving room. The accuracy of the results in the low frequencies is limited because the sound field is not diffuse. This point is rather critical considering that frequencies below 50 Hz are of great importance when considering impact sound insulation and annoyance in lightweight buildings [2]. Because of this and the fact that scanning laser vibrometers and multichannel measurement systems are nowadays available in many laboratories, hybrid experimental methods based on vibration velocity measurements are becoming increasingly popular. They are indeed complementary to the standard methods since they offer increased accuracy at low frequencies and set less stringent requirements to the measurement environment. This last point is an advantage also compared to intensity measurements, that require a highly damped receiving room.

The sound power radiated by a vibrating element can be evaluated, from the experimental measurement of the vibration velocity over its surface, by means of at least three different approaches: the Rayleigh Integral Method (RIM) [3], the Discrete Calculation Method (DCM) [4] and the Integral Transform Method (ITM) [5]. All the three methods have been proven to be accurate and reliable to determine the sound power radiated from planar objects, at least if certain requirements are fulfilled [6–13]. The study presented in this paper was driven by two main motivations: i) in the building acoustics community these methods are still rather

* Corresponding author at: Institutt for bygg- og miljøteknikk, NTNU, Gløshaugen: Høgskoleringen 7a, 7491 Trondheim, Norway.
E-mail address: Simone.Conta@ntnu.no (S. Conta).

https://doi.org/10.1016/j.apacoust.2020.107457
0003-682X/

new, and the differences and respective peculiarities are not well known. A thorough and systematic comparative analysis of this methods is still missing and might help to spread the knowledge about them. ii) These methods were previously employed to evaluate the acoustic performance of building elements, either acoustically or mechanically excited, also comparing the obtained results with results determined by standard sound pressure measurements. However, to the authors' best knowledge, the application of these methods to determine the impact sound level generated by an ISO tapping machine has never been thoroughly investigated.

This paper has three main objectives: i) to provide a systematic and critical comparison of the three measurement methods RIM, DCM and ITM, ii) to evaluate the accuracy and the reliability of these methods to measure the impact sound insulation of complex building elements, with articulated boundary conditions, excited by the ISO tapping machine. The validation was performed by comparing the results of the methods under investigation with laboratory measurements performed according to the standard ISO 10140-3; iii) to investigate to what extent the boundary conditions of the considered structure might represent a limitation for the investigated method.

Firstly, we prepared a finite element (FE) model of a thin aluminium plate and calculated the vibration velocity distribution over the plate surface. From this data, we calculated the radiation efficiency of the plate with the three different methods. These results were used to benchmark the three methods, in order to identify limitations, differences and similarities. Moreover, the effect of varying boundary conditions was also investigated to identify possible shortcomings of each method, especially regarding the ITM. Secondly, we measured the impact sound level of a floor element in an acoustic laboratory with the traditional measurements according to the ISO 10140-3 standard and we recorded in parallel the vibration velocity. Assuming perfect diffuse field conditions, we converted the impact sound level in radiated sound power and compared the obtained values with the results determined by the hybrid methods. The analysis allowed us to asses whether RIM, ITM and DCM are reliable alternative to the standard methods for determining the impact noise level under excitation with an ISO tapping machine. Finally, we present an application example. We considered here a timber hollow-box floor installed on the mock-up of a structural system with moment resisting connections. We compared the radiated sound power under impact excitation measured *in-situ* by DCM and ITM with that measured in the lab following ISO 10140-3. We compare the results and discuss the differences obtained.

In the next section, the three hybrid investigated approaches are introduced. Section 3 describes in detail the methodology adopted and the experimental setups. Section 4 presents the results and finally Section 5 includes the conclusions.

2. Measurement methods

2.1. Measurements according to ISO 10140-3

The standard ISO 10140-3 provides the procedure and the requirements to perform laboratory measurements of impact sound level. This standard is well-known, and we shall recall here just a few elements for the sake of clarity and ease of reference.

The laboratory setup comprises two rooms, placed one above the other, separated by the floor under test. The excitation source is placed at several positions on top of the floor and the sound pressure level is measured in the lower room. The normalized impact sound pressure levels L_n are calculated from the energy averaged sound pressure levels in the receiving room and the measured reverberation times. In this study, an ISO tapping machine, described in the ISO 10140–5, was used as impact source. According to the standard, the normalised impact sound pressure level L_n is determined by normalising the measured sound pressure level L_i with respect to the equivalent absorption area A in the receiving room:

$$L_n = L_i + 10\log\frac{A}{A_0}\,(\mathrm{dB}) \tag{1}$$

where A_0 = 10 m^2. The normalised impact sound pressure level determined according to the standard procedure can be converted to a sound power level using the following equation, based on a diffuse field assumption [13,14]:

$$L_W = L_n + 4\ (\mathrm{dB}) \tag{2}$$

The assumption is strictly valid above the Schroeder Frequency, in our case above ~200 Hz.

The limitations of this approach are related to the sound field in the receiving room. At low frequencies the sound field in the receiving room is not diffuse leading to a large standard deviation in the measurements. It has been also shown that due to strong modal coupling between floor element and receiving room, the accuracy in the determination of the floor properties might be limited [7]. Moreover, further limitations are of more practical character, e.g. the size of the laboratory opening and the mounting of the floor element, which is generally limited to boundary conditions close to simply supported.

2.2. Rayleigh Integral Method

The Rayleigh Integral Method (RIM) is one of the classical approaches used to describe the sound radiation from a planar object, describing it in terms of a sum of point sources [3,14–16]. The sound pressure p at a point R at a time t can be calculated from the complex normal surface velocity $\hat{v}_n(r_s)$ on the vibrating surface S at the position r_s with following relation:

$$p(R,t) = j\frac{\rho_0 c_0 k_0}{2\pi}\oint_S \frac{\hat{v}_n(r_s)\cdot e^{j(\omega t - k_0 r)}}{r}dS \tag{3}$$

or in its discretized form:

$$p(R,t) = j\frac{\rho_0 c_0 k_0}{2\pi}\sum_i \frac{\hat{v}_n(r_{s,i})\cdot e^{j(\omega t - k_0 r_i)}\cdot S_i}{r_i} \tag{4}$$

where ρ_0 is the density of air, c_0 is the speed of sound in air, ω is the angular frequency, k_0 is the acoustic wavenumber, $r_i = |R - r_{s,i}|$ indicates the distance between the plate's vibrating element i with area S_i and the position R, j is the imaginary unit.

We can use Eq. (4) to calculate the sound pressure distribution over an imaginary hemisphere centred around the vibrating surface. Then, we can calculate the radiated sound power W by integrating the root mean square sound pressure p^2 over the surface of the hemisphere Ω [6,14]:

$$W = \oint_\Omega \frac{\tilde{p}^2}{\rho_0 c_0}\cdot d\Omega \tag{5}$$

or in its discretized form:

$$W = \sum_i \frac{\tilde{p}_i^2\cdot\Omega_i}{\rho_0 c_0} \tag{6}$$

The above equations are valid only under the assumption of a locally plane wave field and under free-field conditions. The requirement of a locally plane wave imposes that the radius of hemisphere, over which the sound pressure is computed, is sufficiently large. Also, the discretisation of points over the hemisphere

surface must be fine enough to capture the details of the sound radiation pattern. Both aspects can be easily checked by a trial and error procedure and verification that the results do not depend on the settings of the calculation. Alternatively, one could calculate the sound intensity directly at the interface between the fluid and the vibrating element ($z = 0$, with z the cartesian axis perpendicular to the panel surface) and integrate over its surface [7]. The two approaches are equivalent. The second approach requires a slightly more advanced mathematical formulation but avoids the calculation over the large amount of points on the sphere. In the current paper, we used the first approach.

The spatial discretisation of the radiating plate must consider the Nyquist-Shannon sampling theorem and the velocity of the bending waves propagating through the panel. The requirements of the theorem must be fulfilled over the whole frequency range of interest. If Δx, Δy are the size of the i^{th} element of the plate and $\lambda_{b,x}$, $\lambda_{b,y}$ are the wavelength of the bending waves in the panel along the x and y direction respectively:

$$\Delta x < \frac{\lambda_{b,x}}{2}, \Delta y < \frac{\lambda_{b,y}}{2}. \tag{7}$$

2.3. Integral Transform Method

The Integral Transform Method is an alternative classical approach to the determination of the radiated sound power from planar objects and its theoretical approach was already described by Heckl in [5]. Williams and Maynard described the same method and discussed the details of its implementation in [17].

The sound power W radiated by a surface S can be calculated from the sound pressure $p(x,y,z = 0) = p_s(x,y)$ on the surface of the vibrating structure and from the complex normal surface velocity $\hat{v}_n(x,y)$ on the vibrating surface S at the position (x,y) with the well know relation [18]:

$$W = \frac{1}{2} Re\left\{ \iint_{-\infty}^{+\infty} p_s(x,y)\, \hat{v}_n(x,y)^* dxdy \right\} \tag{8}$$

which corresponds to integrating the sound intensity over the radiating surface. By using the Rayleigh-Parseval theorem and the expression for the sound pressure from a plane radiator described as a sum of plane waves [5], the above equation can be rewritten as [18]:

$$W(f) = \frac{1}{2} \frac{\rho_0 c_0}{4\pi^2} \mathrm{Re}\left\{ \iint_{-\infty}^{+\infty} \frac{k_0(f)}{\sqrt{k_0^2(f) - k_x^2 - k_y^2}} \left|\hat{v}(k_x,k_y,f)\right|^2 dk_x dk_y \right\} \tag{9}$$

where the dependency on the frequency f is explicited, $\hat{v}(k_x,k_y,f)$ is the complex vibration velocity of the plate surface expressed in the wavenumber domain, i.e. the 2-D Fourier transform of plate vibration velocity, k_0 is the wavenumber in air and k_x, k_y are the wavenumber components of the structural waves in the plate, respectively along the x and y direction.

For the purpose of this paper, we implemented the procedure following the approach presented in [11], which we refer the reader to for the implementation details. For ease of reference, we indicate here the discretized form of Eq. (9) for the radiated sound power W:

$$W(\gamma) = \frac{1}{2} \frac{\rho_0 c_0}{4\pi^2} \mathrm{Re}\left\{ \sum_{\alpha=1}^{M_\alpha} \sum_{\beta=1}^{M_\beta} \frac{k_0(\gamma)}{\sqrt{k_0(\gamma)^2 - (\alpha\Delta k_x)^2 - (\beta\Delta k_y)^2}} \left|\hat{v}(\alpha,\beta,\gamma)\right|^2 \Delta x^2 \Delta y^2 \right\} \Delta k_x \Delta k_y \tag{10}$$

where γ indicates the discrete frequency step, α, β are the coordinates in the wavenumber domain, $M_\alpha = z_p \frac{l}{\Delta x}$ and $M_\beta = z_p \frac{w}{\Delta y}$ represent the number of samples in the wavenumber domain with $l \times w$ the dimensions of the plate, with z_p the zero padding factor required in the 2-D Fourier transform; $\Delta x, \Delta y$ is the grid size of the vibration velocity measurements (i.e. the dimensions of the plate divided by the number of grid points in the respective directions) and $\Delta k_x = \frac{2\pi}{z_p l}, \Delta k_y = \frac{2\pi}{z_p w}$ is the resolution in the wavenumber domain. In the practical usage of this relationship, the vibration velocity in the wavenumber domain will be calculate with a 2-D Fourier transform of the measured vibration velocity field at each frequency step γ. Many of the practical challenges are shared here with acoustic holography. An example is the use of the zero padding to reduce wraparound errors and obtain an adequate aperture size [17,19,20]. It is interesting to note here that Williams and Maynard already showed that the use of zero padding does not create any limitation with respect to the plate boundary condition, even in the extreme case of all the edges in a free condition (F-F-F-F BCs).

The measurement of the vibration velocity on the plate underlies the Nyquist-Shannon sampling theorem requirements for the Integral Transform Method in the same manner as it is for the RIM. Further aspects must be considered when assessing the limit of validity of the ITM method: they include the bias error, the bending wave velocity in the measurement object and the decay of the side lobes.

The bias error is due to the numerical singularity that arises whenever the wavelength or a multiple of it matches the size of the aperture. This problem can be tackled either by refining the numerical procedure to contain the singularity [11,17] or by further increasing the zero padding factor. Both approaches deliver comparable results.

To discuss the further requirements of ITM, it is helpful to introduce a few diagrams. Fig. 1 shows typical wavenumber plots obtained during the analysis procedure with the ITM. In the wavenumber versus frequency diagram (a) we recognise the dispersion curve of the structural waves k_b, highlighted by the dashed line. For reference, the wavenumber of the soundwaves in air k_0 is plotted as a solid line. A closer look at selected frequencies reveals the specific features of the spectrum (diagrams b and c of Fig. 1): the main peaks represent the vibrational modes of the plate. The side lobes are given by the finite size of the panel and the boundary conditions, which also have a strong influence on their decay. From Eq. (10), it follows that only the area within the radiation circle with radius k_0 contributes to the sound radiation. In Fig. 1a, the same area is that between the two solid lines. Therefore, the side lobes are a major contribution to the radiated sound power, especially for frequencies below the critical frequency f_c. Considerations about aliasing must include the side lobes. As a good rule of thumb, to avoid aliasing the side lobes must decay considerably before reaching k_{max}.

Fig. 2 shows idealized curves for the following three cases and the respective upper limits of the method. Case a): the frequency f_{max} at which the structural wave dispersion curve reaches the limit $k_{x,max} = \frac{\pi}{\Delta x}$ (determined by the Nyquist-Shannon theorem requirements on the grid spacing) is well below the critical frequency f_c of the ITM. In this case f_{max} is the upper limit of validity of the ITM. The limit might be slightly lower depending on the measurement setup and the boundary conditions. In the case of orthotropic plates, or a different grid size along the x and the y direction, the lowest frequency limit must be considered. Case b): the critical frequency f_c is close to the frequency f_0 at which the wavenumber of sound waves in air reaches the limiting wavenumber: $k_0 = k_{max}$. In this case f_0 is the upper limit at which the ITM method delivers reliable results. This limit is best visualised by looking at Fig. 1c and considering that i) the sum of Eq. (10) is performed over the whole wavenumber domain showed by the diagram and ii) the surface within the radiation circle k_0 contributes to sound radia-

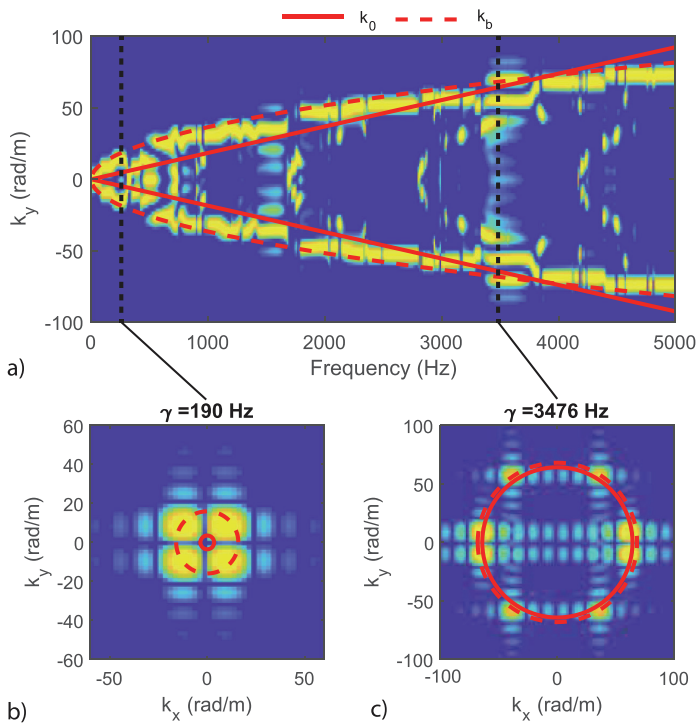

Fig. 1. Typical wavenumber plots obtained by the ITM. a) wavenumber spectrum along the y direction for $k_x = 0$ as a function of the frequency, b) wavenumber spectrum at the frequency step 190 Hz (note that the k_x and the k_y is adapted for better readability), c) wavenumber spectrum at the frequency step 3476 Hz. $f_c = 4000$ Hz, $k_{y,max} = 150$ rad/m, $f_0 = 6000$ Hz.

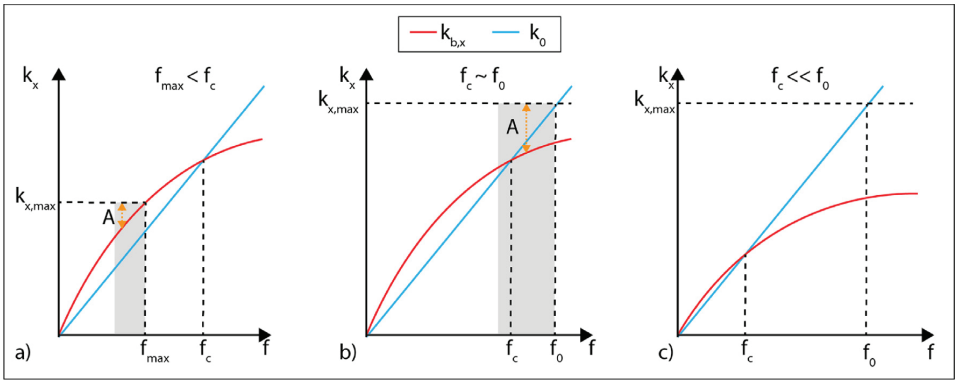

Fig. 2. Key elements to assess the requirements when applying the ITM method. a) show the case where f_{max} is below f_c; b) f_c and f_0 are close to each other on a logarithmic scale; c) f_c is much smaller than f_0. The blue line is the dispersion curve of the sound waves in air. The red line is the dispersion curve of the structural waves in the plate. (For interpretation of the references to color in this figure legend, the reader is referred to the web version of this article.)

tion. The limit describes the situation where the circle reaches the boundaries of the diagram. For higher frequencies, a portion of the circle would be outside of the diagram boundaries causing an information loss and hence possibly corrupting the results. As for the previous case, the limit might be slightly lower depending on the measurement setup and the boundary conditions. Case c): the critical frequency is much lower than the upper frequency limit: $f_c \ll f_0$. The ITM delivers reliable results also above f_0. The reason for this is that for frequencies $f \gg f_c$ the kernel K in Eq. (10) approaches unity:

$$K[\alpha, \beta, \gamma] = \frac{k_0(\gamma)}{\sqrt{k_0(\gamma)^2 - (\alpha \Delta k_x)^2 - (\beta \Delta k_y)^2}} \rightarrow 1 \text{ for } f \gg f_c \qquad (11)$$

This relaxes the requirement set by the Nyquist-Shannon theorem and aliasing can be effectively exploited to extend the measurement range well above the limit f_0. The results in Section 4.2 show an example of this case.

Both in case *a)* and *b)*, the upper limit must be evaluated considering both the bending wave speed and the decay of the side lobes in the wavenumber spectrum. This is highlighted in Fig. 2 with the symbol *A*, indicating the distance between $k_{x,\max}$ and the curve $k_{b,x}$, and the grey area indicating the range where this two lines approach. This distance must be sufficient to let the side lobes decay before reaching $k_{x,\max}$. This distance is dependent on the tested object, its boundary conditions and the measurements settings. An example of the importance of this assessment is presented in Section 4.1, when discussing the grid size required by the all-free-edges (F-F-F-F) boundary conditions.

The ITM offers the advantage of delivering additional material information (e.g. structural wave velocity in the plate) compared to the other methods presented in this paper [13]. Additionally, the measured vibration velocity could also be used to investigate the sound intensity radiated from the element with the supersonic intensity technique [21], which uses the very same data and processing procedure implemented for the ITM.

2.4. Discrete Calculation Method

The Discrete Calculation Method (DCM) is a hybrid approach, proposed by Hashimoto [4] in order to experimentally evaluate the sound power radiated by a planar vibrating structure based on the radiation impedance concept. As the two previous methods, it requires the complex normal vibration velocity $\widehat{v}_{n,i}(\omega,x,y)$ to be measured on a grid of points *i* evenly distributed over the vibrating surface. The sub-elements associated to each measurement position are considered as equivalent radiating pistons; their self Z_{ii} and cross radiation impedances Z_{ij} can be analytically computed as:

$$Z_{ii} = \rho_0 c_0 s_i \left[1 - \frac{J_1(2k_0a_i)}{k_0a_i} + \frac{S_1(2k_0a_i)}{k_0a_i}\right] \tag{12}$$

$$Z_{ij} = \frac{\rho_0 c_0 k_0^2 s_i s_j}{2\pi}\left[2\frac{J_1(k_0a_i)}{k_0a_i}\right]\left[2\frac{J_1(k_0a_j)}{k_0a_j}\right]\left(\frac{\sin k_0 d}{k_0 d} + i\frac{\cos k_0 d}{k_0 d}\right) \tag{13}$$

The area of the i^{th} equivalent piston element is s_i, while a_i is its equivalent radius and d is the distance between the i^{th} and j^{th} elements, while J_1 represents the first order Bessel's function, and S_1 is the Struve's function.

Under the assumption of a baffled plate radiating in the free field, the radiated sound power can be determined from the velocity distribution and the self and mutual radiation impedances as:

$$W = \sum_i \left[\mathrm{Re}(Z_{ii})|v_i|^2 + \sum_j \mathrm{Re}\left(Z_{ij}\, v_i v_j\right)\right] \tag{14}$$

where we omitted the subscript *n* to improve the readability of the equation. In order to obtain the root-mean-square (rms) radiated sound power, as for the RIM and the ITM, the DCM requires as input data the rms complex velocity.

As indicated in the original paper [4], the requirements set by the Nyquist-Shannon theorem must be fulfilled up to at least the critical frequency when the DCM method is used. Above the critical frequency the grid size plays only a minor role on the accuracy of the results.

3. Methodology

As stated in the introduction, we want to accomplish three main tasks: i) numerical benchmark the RIM, ITM and DCM on a simple object considering different boundary conditions, ii) compare the radiated sound power obtained with these three advanced hybrid methods with the radiated sound power determined by impact sound pressure measurements in a standard sound transmission test facilityand iii) to test these three advanced methods on a complex setup and evaluate possible advantages compared to standard laboratory measurements.

In this section, we present the details of the tested setups.

3.1. Benchmark the methods with different boundary conditions

The first task is to benchmark RIM, ITM and DCM on a simple object, i.e. a thin aluminium plate, with different boundary conditions (all edges clamped C-C-C-C, all edges simply supported S-S-S-S, all edges free F-F-F-F, two opposite edges simply supported and two free S-F-S-F). This shall highlight possible limitations or artefacts due to the specific methods.

An aluminium plate (Young's modulus E_{alu} = 7.1 × 1010 N/m^2, density ρ_{alu} = 2700 kg/m^3, Poisson's ratio ν = 0.33, damping factor η = 0.03) with dimensions 0.5 m × 0.6 m × 0.003 m was modelled in the FEM software Abaqus/CAE 2017 (Fig. 3). We used C3D8 general purpose linear brick elements with a maximum mesh size of 0.01 m, which is 10 times smaller than the bending waves wavelength in the aluminium plate at 6000 Hz. The calculations were performed as a steady state linear perturbation with a resolution of 10 Hz from 10 Hz to 5650 Hz so that the results could be evaluated in 1/3 octave bands from 20 Hz to 5000 Hz. The excitation was a harmonic point force distributed over four adjacent nodes at the position *x = l/4*, *y = w/4*. The vibration velocity of the nodes on the bottom face was stored on 120 × 100 grid and evaluated on a variable subset of points, as described in Section 4.1.

The vibration velocity distribution data set produced by the numerical simulation was then fed to Matlab scripts implementing the three methods.

When applying the RIM method, we used a calculation sphere with radius 10 m and 1600 points evenly distributed on its surface.

When applying the ITM method we used a fixed zero-padding factor z_p = 20 for all grid sizes.

3.2. Measurements according to ISO 10140-3

This experimental investigation was performed according to ISO 10140-3 standard on a complex floor structure. The vibration velocity on the bottom side of the plate was measured in addition to the sound pressure in the receiving room.

A timber hollow-box floor element with dimension 2.4 m × 3. 7 m × 0.5 m was installed in the vertical sound transmission test facility at the SINTEF acoustic laboratory in Oslo (Fig. 4). The cross-section geometry of the element is shown in Fig. 5 along with the key elements of the measurement setup. The hollow part of the element was partly filled with gravel with a surface mass of approximately 100 kg/m^2. The floor structure was simply supported on the two short sides with an interposed resilient stripe (Sylomer SR55) and free on the two long sides (S-F-S-F).

The floor element was excited at four positions with a standard tapping machine. The sound pressure was measured in the receiving room (V = 200 m^3) with one microphone on a rotating boom at two positions according to ISO 10140-3. The reverberation time was measured accordingly. The radiated sound power was calculating using Eqs. (1) and (2) and averaging energetically the four tapping machine positions according to the standard.

With the same setup, the acceleration in the vertical direction was measured on the bottom surface of the floor element on a 10 × 13 points measurement grid, corresponding to a spacing 0,24 m × 0,28 m (Fig. 5). The corresponding wavenumber limits are: $k_{x,\max}$ = 13 rad/m, $k_{y,\max}$ = 11 rad/m; f_0 = 595 Hz (y-direction).

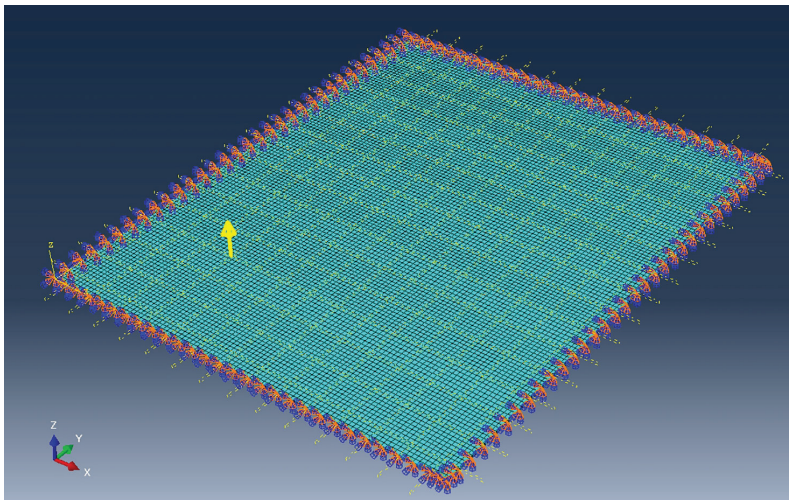

Fig. 3. FE model of the aluminium plate in Abaqus. The mesh (black continuous lines), the evaluation grid (dashed yellow lines), the point load (yellow arrow) and the boundary conditions (C-C-C-C) are shown. (For interpretation of the references to color in this figure legend, the reader is referred to the web version of this article.)

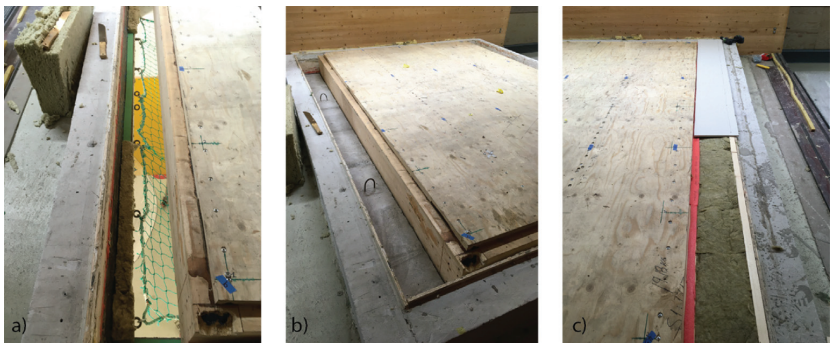

Fig. 4. Three moments of the installation of the test floor into the lab opening: a) positioning of the element (note the S-F-S-F boundary conditions), b) filling of the remaining space with 150 mm concrete and c) sealing of the volume with mineral wool and plasterboard.

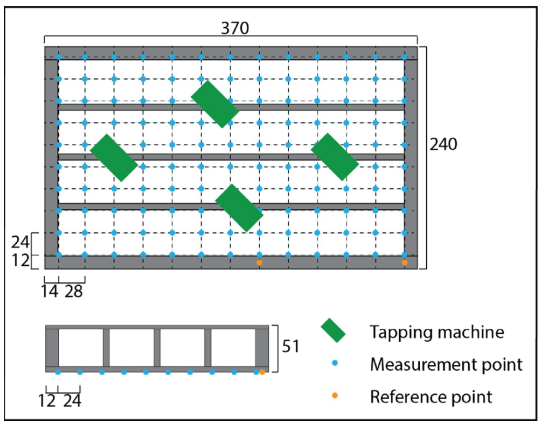

Fig. 5. Schematic of the measurement setup showing the cross section of the measurement objects, the accelerometer positions and the excitation positions. All dimensions in cm.

The critical frequency f_c for this element was determined in (13) as $f_c \cong 250$ Hz. In terms of ITM requirements, this experimental setup is an example of the condition showed in Fig. 2c.

One line (10 points) of the grid was measured at a time, then the tapping machine was moved to the next position and the procedure repeated. After all the excitation positions were covered, the accelerometers were moved to the next line. One additional accelerometer was kept fixed for the whole measurement session as phase reference. The radiated sound power was then calculated for each tapping machine position and the results averaged energetically. The same set of data was analysed with the three methods RIM, ITM and DCM.

When applying the RIM method, we used a calculation hemisphere with radius 10 m, discretised with 1600 points evenly distributed on its surface. When applying the ITM method we used a zero-padding factor $z_p = 60$.

3.3. Application example

Finally, the three methods were tested on a complex setup to evaluate their performance in a "practical" case. The *in-situ* radi-

Fig. 6. Measurement test-rig used for the application example.

ated sound power measured on the complex setup was compared to the radiated sound power determined in laboratory to assess how the laboratory boundary conditions affect the results.

The same floor element, which was tested in the OSLO laboratory, was also installed on the mock-up of a structural system based on moment resisting frames. The mock-up was composed by the floor element mounted on four glulam columns with dimensions 0.4 m × 0.45 m × 5 m by means of threaded rods and metal brackets. The setup is shown in Fig. 6, while the reader may refer to [13] for detailed information on the system.

Table 1
Requirement fulfillment criteria for RIM, ITM and DCM.

RIM criteria:	$\Delta x < \frac{\lambda_{b,x}}{2}, \Delta y < \frac{\lambda_{b,y}}{2}$ @ maximum frequency of interest $f_{max,i}$
ITM criteria:	$f_{max,i} < f_0$ as per case b) in Fig. 2
DCM criteria:	$\Delta x < \frac{\lambda_{b,x}}{2}, \Delta y < \frac{\lambda_{b,y}}{2}$ @ critical frequency f_c

Table 2
Key quantities to evaluate the criteria in Table 1.

Maximum frequency of interest:	$f_{max,i}$ = 5623 Hz, to cover the 5000 Hz 1/3 octave band
Critical frequency:	f_c = 4000 Hz
f_0 (frequency where $k_0 = k_{max}$):	k_0 @ $f_{max,i}$: 104 rad/m
Bending waves @ $f_{max,i}$:	$v_{b,max,i}$ = 408 m/s, $\lambda_{b,max,i}$ = 0.072 m, $k_{b,max,i}$ = 87 rad/m
Bending waves @ f_c:	$v_{b,c}$ = 343 m/s, $\lambda_{b,c}$ = 0.086 m, $k_{b,c}$ = 73 rad/m

We used the same accelerometer configuration and measurement procedure described in Section 3.2. The radiated sound power was determined by the three methods RIM, ITM and DCM. It shall be noted here that the influence of the airborne excitation on the bottom plate due to the noise radiated by the tapping machine exciting the top plate and the corresponding reverberant sound field in the facility was negligible, as discussed in [13].

4. Results

4.1. Assessment of the grid size

In Table 1, we summarize the criteria for the evaluation of the requirements on the grid size for the three methods. In Table 2, we provide the key quantities for the evaluation and in Table 3, we present the criteria assessment for the aluminium plate under investigation evaluated with three different grid sizes: 15 × 10, 30 × 25 and 60 × 50.

We calculated the radiated sound power $L_{w,grid}$ with the three methods RIM, ITM and DCM for the boundary conditions CCCC, SSSS, SFSF, FFFF and the three different grid sizes: 60 × 50, 30 × 25 and 15 × 10 points. Taking as reference the grid 60 × 50, we calculated the level difference

$$\Delta L_W = L_{W,60x50} - L_{w,grid_x}(dB) \quad (15)$$

The results obtained for each case are presented in Fig. 7.

For all the three methods, the results presented in Fig. 7 show a strong dependency of the grid size on the BCs. For the CCCC BCs, no difference is observed between the results obtained with the grid size 60 × 50 and 30 × 25 as expected, since both grid sizes fulfill the criteria over the whole frequency range of interest. The ITM method and the DCM method deliver reliable results even with the larger grid points spacing, which do not fulfill the criteria for the highest frequencies within the range of interest. The Rayleigh method seems to be the most sensitive to the grid size, showing the largest deviations with the smallest grid. With SSSS BCs, small deviations appear for all methods but well within ±1 dB, if the criteria are fulfilled. When the BCs are changed to SFSF and FFFF the deviations increase to more than ±2 dB with the grid size 30 × 25 even though it does fulfill the spatial sampling criteria. The finest considered grid points spacing seems to be required to obtain accurate results.

4.2. Benchmark the methods with varying boundary conditions

Fig. 8 shows the radiation index L_σ of the aluminium plate

$$L_\sigma = 10 \log_{10} \sigma \quad (16)$$

Table 3
Evaluation of the criteria given in Table 1, based on the quantities provided in Table 2.

Dimensions aluminium panel: l = 0.5 m, w = 0.6 m						
Grid points	15 × 10		30 × 25		60 × 50	
Δx, Δy (m)	0.033	0.060	0.017	0.024	0.008	0.012
$\frac{\lambda_{b,max,i}}{2}$	0.036	0.036	0.036	0.036	0.036	0.036
RIM Criteria:	fulfilled	not fulfilled	fulfilled	fulfilled	fulfilled	fulfilled
k_{max} (rad/m)	94	52	188	131	377	262
f_0 (Hz)	5100	2833	10,200	7083	20,400	14,167
ITM Criteria:	not fulfilled	not fulfilled	fulfilled	fulfilled	fulfilled	fulfilled
$\frac{\lambda_{b,c}}{2}$	0.043	0.043	0.043	0.043	0.043	0.043
DCM Criteria:	fulfilled	not fulfilled	fulfilled	fulfilled	fulfilled	fulfilled

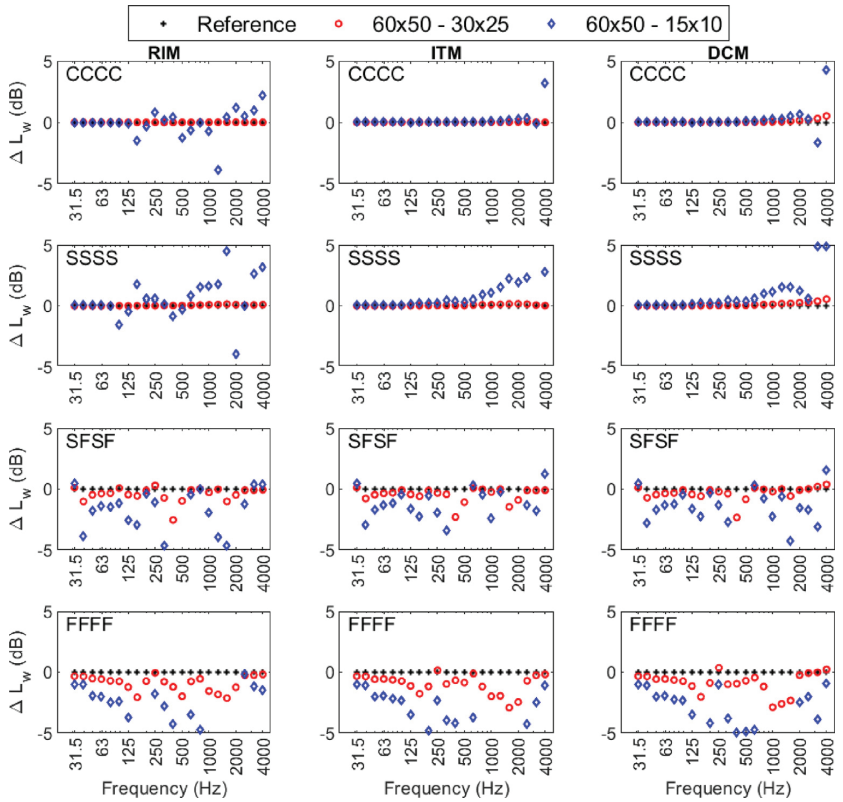

Fig. 7. Difference in the radiated sound power DL_W obtained from different grid sizes for the CCCC, SSSS, SFSF, FFFF BCs, with the methods RIM, ITM and DCM. Grid sizes: 30×25, 15×10. The differences are calculated by taking the finer grid 60×50 as reference.

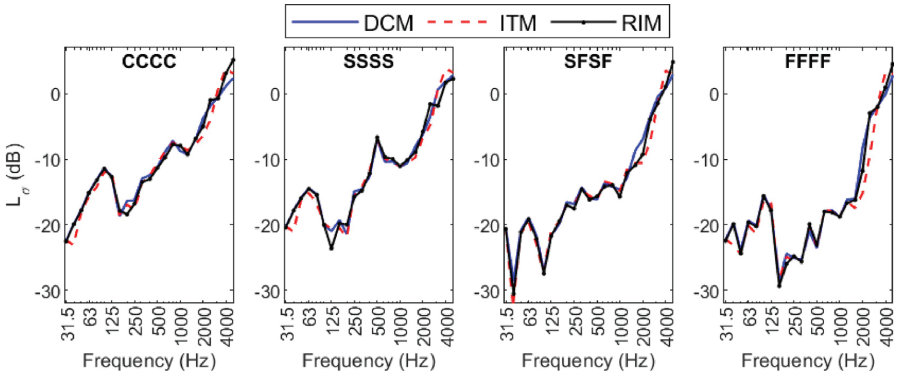

Fig. 8. Comparison of the radiation efficiency calculated with the three methods RIM, ITM and DCM for following boundary conditions: C-C-C-C, S-S-S-S, S-F-S-F, F-F-F-F. Grid size: CCCC and SSSS: 30×25; FFFF and SFSF: 60×50.

where σ is the radiation efficiency calculated from the vibration velocity distribution obtained from the FE simulation. The three methods were used to calculate the radiation efficiency: ITM, DCM and RIM. The four diagrams present following boundary conditions: all edges clamped (CCCC), all edges simply supported (SSSS), two opposite edges simply supported and two free (SFSF), all edges free boundary conditions (FFFF). Based on the results presented in Section 4.1, we used the grid size 30×25 for CCCC and SSSS and 60×50 for FFFF and SFSF.

The calculated radiation efficiencies show the expected behaviour (see e.g. [22]) and the results from the three methods show a good agreement. However, it is helpful to plot the differences

between the curves to gain a more detailed view. The two diagrams in Fig. 9 presents the differences in the radiation efficiency for each set of BCs obtained respectively as:

$$\text{a)} \quad \Delta L_\sigma = L_{\sigma,RIM} - L_{\sigma,ITM}(\text{dB}) \tag{17}$$

$$\text{b)} \quad \Delta L_\sigma = L_{\sigma,RIM} - L_{\sigma,DCM}(\text{dB}) \tag{18}$$

where the subscript indicates which method was used to calculate σ. In the diagrams, we also highlight the ±2 dB range using black dashed lines.The comparison between RIM and ITM shows deviations mainly within ±2 dB in the whole frequency range of interest, even though at a few frequency bands the discrepancies are up to 3 dB and in the 3150 Hz 1/3 octave band the deviation is even larger. The same observation can be made for all BCs, even though, the deviations seem to increase with FFFF BCs. The comparison between RIM and DCM shows a good agreement and highlights a slightly increasing deviation between the results as the frequency increases. The discrepancies between the methods might be related to the near field generated by the excitation used: excitation by a harmonic concentrated force as in this case, generates a strong nearfield comparable to that generated by a shaker in an experimental setup [23]. A nearfield is a local feature of the vibrational field. Local features are described by the high frequency components of the spectrum and due to the finite size of the grid these features can be reproduced only to a limited extent [16]. The sensitivity of the methods to these effects is different due to their different mathematical implementation and it might be worth of further investigation.

As we have seen in the previous section, the grid size must be adapted to the BCs for all the three investigated methods. Possible deviations from the reference radiated sound power might happen at different frequencies for the different methods and the different BCs. This prevent us from making an absolute reliability ranking of these methods.

The ITM results could be further investigated by studying the wavenumber spectra. Each color plot in Fig. 10 shows the vibration

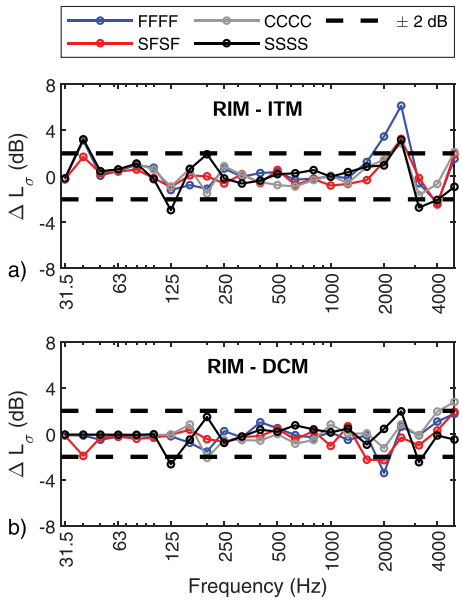

Fig. 9. Differences between radiation efficiency σ calculated by a) RIM and ITM and b) by RIM and DCM, for different boundary conditions. Grid size: see Fig. 8.

velocity wavenumber spectrum multiplied with the kernel *K*, given in Eq. (11), in the format k_x (longitudinal direction) versus frequency at $k_y = 0$. At each frequency step the amplitude was normalized to the maximum in the same frequency step. Data are shown in dB with a 10 dB range. The black dashed line shows the wavenumber for bending waves calculated according to the thin plate theory. The solid white line indicates the wavenumber of the sound waves in air. The area within the two white lines contributes to sound radiation. The plots are presented for two boundary conditions and two grid sizes: a) CCCC, 30 × 25; b) FFFF 30 × 25; c) CCCC, 60 × 50; d) FFFF, 60 × 50.

The diagrams a) and c) in Fig. 10 clearly show the dispersion curves of the bending waves and higher order lamb waves. The curves in a) and c) are nearly identical confirming that a 30 × 25 grid is in this case appropriate to avoid aliasing effects with CCCC BCs. The diagrams b) and d) in Fig. 10 differs strongly in the area between the two white solid lines (e.g. the features highlighted with the red arrows in b)). This indicates that a 30 × 25 grid is in this case not sufficient to avoid aliasing effects with FFFF BCs. A larger 60 × 50 grid is then mandatory to obtain reliable results. An even larger grid or higher z_p might slightly improve the accuracy of the results but at a higher computational cost.

4.3. Measurements according to ISO 10140-3

In Fig. 11, we compare the radiated sound power level, obtained from sound pressure measurements performed in a sound transmission test facility according to the standard ISO10140-3 (ISO), with the results obtained from vibration velocity measurements, performed on the very same setup and analysed with the RIM, ITM and DCM approaches. In the upper diagram the sound power level L_w obtained by each method is presented. As explained in Section 2.1, the impact noise level obtained by the standard method was converted to a radiated sound power level assuming a perfectly diffuse sound field, by means of Eq. (2). To ease the comparison, we show in the lower graph the respective difference between each curve and the ISO curve.

We observe, in general, a good agreement between the methods within the frequency range in which the requirements of the methods are fulfilled. We observe that below 125 Hz the vibration velocity-based measurement methods are in close agreement with each other but clearly deviate from the results based on sound pressure measurements. The limitation here are not the measurement methods, but the diffuse field assumption, which is required to convert the sound pressure levels into the radiated sound power levels. This assumption is not valid at low frequencies in our measurement setup. The requirements set by the Nyquist-Shannon theorem are met up to approximately 500 Hz on this setup [13]. We clearly observe that the Rayleigh methods fails above this frequency, due to the introduced aliasing effects. ITM and DCM still deliver reliable data as expected. Above 4000 Hz, both the DCM and the ITM deviate from the standard results but they agree with each other. We suspect that this has to do with the experimental setup and the mounting of the accelerometers.

It is interesting at this point to compare the results presented in Fig. 11 with the results presented in Figs. 8 and 9. The results from the experimental setup show smaller deviations between the methods as compared to the results from the numerical simulation. In fact, the deviations between ITM and DCM are well within ±2 dB in the experimental situation, while the ±2 deviation was exceeded in several frequency bands in the numerical simulation results. One possible reason for the better agreement might be that in the experimental case no near field effects are expected, mainly because of the larger distance between excitation point and measurement points [23]. In addition, the larger spatial extension of the experimental excitation (the length of the tapping machine is

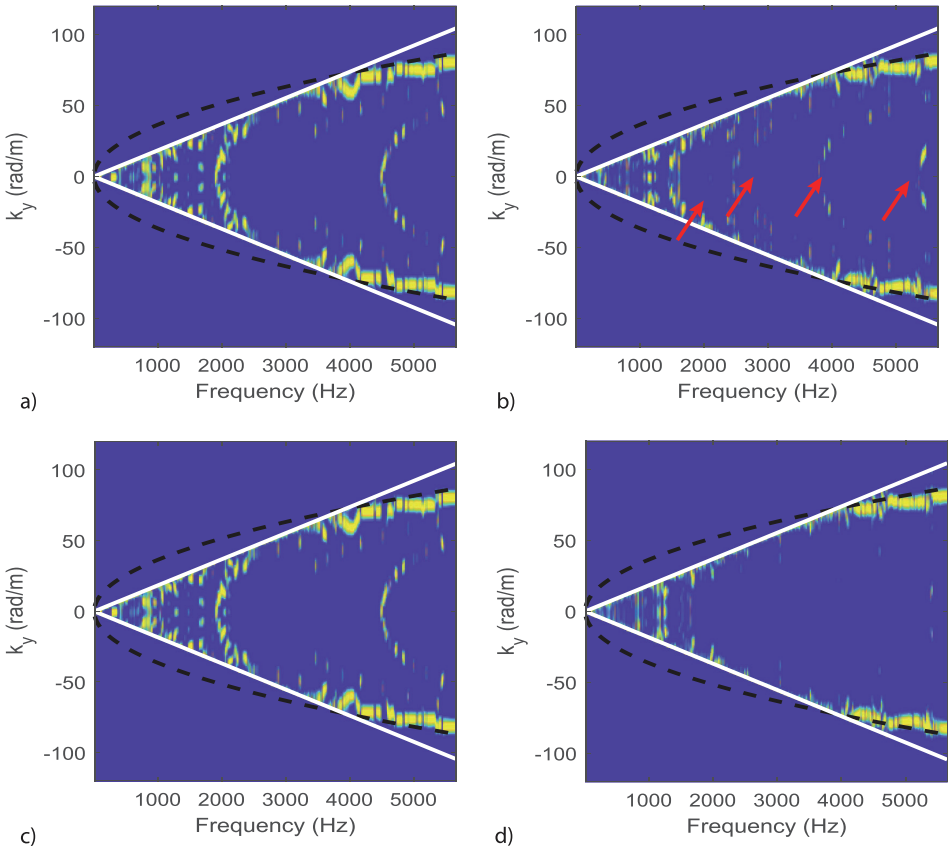

Fig. 10. Wavenumber spectrum of the product K · v (Eq. 10) plotted for $k_y = 0$, normalized to the maximum amplitude at each frequency step. BCs and grid sizes: a) CCCC, 30 × 25; b) FFFF 30 × 25; c) CCCC, 60 × 50; d) FFFF, 60 × 50. In b) the red arrows mark the aliasing effects. (For interpretation of the references to color in this figure legend, the reader is referred to the web version of this article.)

0.5 m) compared to the point excitation of the simulation was probably able to excite a larger number of modes within the considered frequency range, smoothening the peaks and the dips caused by the resonances. The averaging between tapping machine excitation position goes in the same direction. Both aspects possibly reduce the discrepancies between the methods.

These results demonstrate that all three methods RIM, ITM and DCM are valuable alternatives to the standard method to determine the radiated sound power of a planar object due to impact excitation. Neither the boundary conditions, nor the sequential excitation by the tapping machine at several positions, nor the shifting of the accelerometers over the measurement grid appear to be limiting factors to the application of the methods.

4.4. Application example

As an application example, we present in this section the results obtained by ITM and DCM for the same floor element installed in two different situations: in a standard laboratory setup (Oslo) and on a moment resisting frame (CVGS). We exclude RIM from the comparison in this case due to its limited frequency range of validity.

Fig. 12 shows the radiated sound power obtained for the same floor in the two different situations by ITM (a) and DCM (b).

Both methods deliver results in close agreement and can identify the specific radiation properties of the tested setups. The radiated sound power obtained in the Oslo laboratory and at CVGS are almost identical above 500 Hz. Below 500 Hz, the modal behaviour of the floor elements on the two setups differs because of the different boundary conditions and this affects the radiated sound power. Between 100 Hz and 500 Hz the radiated sound power level is up to 3 dB higher with the CVGS BCs. Between 50 Hz and 100 Hz the radiated sound power level is up to 4 dB lower with the CVGS BCs. In the 31.5 Hz 1/3-octave band and below 25 Hz forced vibration introduced by the undampened columns of the CVGS setup determine the high radiation peaks. Both the ITM method and the DCM method can catch these features.

5. Conclusions

We presented three measurement methods suitable to determine the radiated sound power from planar objects and benchmarked them in the special case of mechanical excitation, either by a point force or by a tapping machine. We discussed in detail the limit of validity of the methods and presented relevant examples.

The comparison of the methods was firstly performed based on numerical data computed for an aluminium plate with vary-

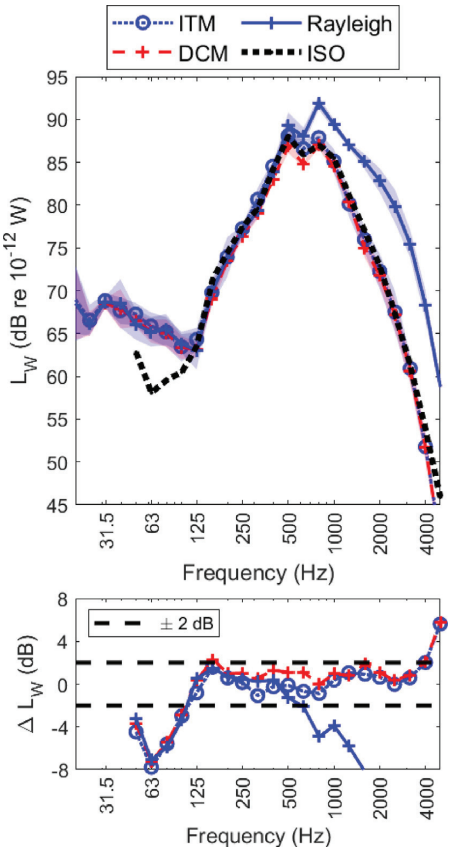

Fig. 11. Comparison of the three methods RIM (Rayleigh), ITM, DCM with the radiated sound level obtained from the impact sound level measured according to the standard ISO10140-3 on a S-F-S-F lab setup.

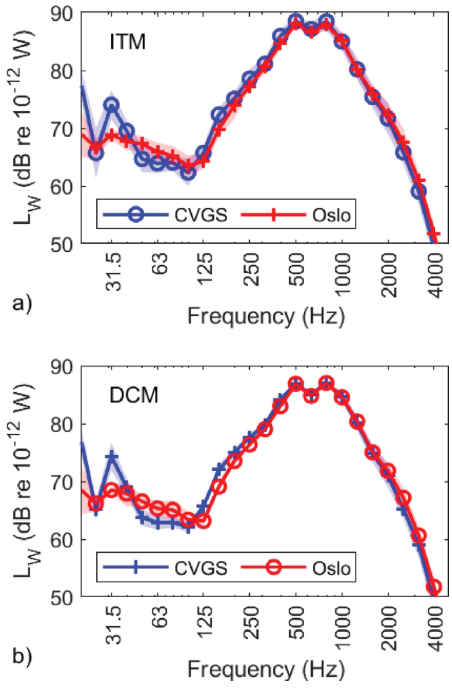

Fig. 12. Sound power level measured in the acoustic lab (Oslo) and "in situ" (CVGS) with ITM a) and DCM b).

ing boundary conditions. The benchmarking of the three methods RIM, ITM and DCM on such a simple object showed a general good agreement between the methods over the whole frequency range of interest, with discrepancies mainly within ±2 dB, even though higher deviations were found in certain frequency bands. The required grid size resulted to be dependent on the BCs for all methods. F-F-F-F boundary conditions requires a finer grid to accurately evaluate the radiated sound power compared to boundary conditions restraining the edges to a higher degree.

The three considered methods were then applied to an experimental data set, measured in laboratory conditions on a complex floor structure under impact excitation by a tapping machine. We compared the sound power levels computed by means of these three hybrid methods with the sound power obtained from sound pressure measurements in a standard sound transmission test facility according to the ISO 10140-3 standard. A good agreement between the methods was found from 20 Hz to 4000 Hz, as long as the validity requirements of the methods were fulfilled. No limitations were observed due to the sequential repositioning of the tapping machine or the position shifting of the accelerometers.

Finally, the ITM and DCM methods were applied to a complex experimental setup, showing that they provide accurate results and they are consistent with each other also for in situ conditions. We showed that these methods can be used to obtain accurate information on the specific experimental setup. This is an advantage compared to the standard laboratory setup, since they require reduced practical constraints.

CRediT authorship contribution statement

Simone Conta: Conceptualization, Methodology, Software, Investigation, Writing - original draft. **Andrea Santoni:** Writing - review & editing, Software. **Anders Homb:** Writing - review & editing, Supervision.

Declaration of Competing Interest

The authors declare that they have no known competing financial interests or personal relationships that could have appeared to influence the work reported in this paper.

Acknowledgments

This study has been carried out within the Woodsol project, a project funded by The Research Council of Norway and leaded by Kjell Arne Malo at NTNU. The project include research at NTNU and SINTEF Building & Infrastructure and the PhD grant for the first author of this paper, which is gratefully acknowledged. Petra Rüther at SINTEF was work package leader for "WP6 Prototype", which made the prototype possible. Sveinung Nesheim and Aivars Vilguts, both PhD students at NTNU and member of the Woodsol project, were involved in the design and construction of the WOODSOL prototype. Leif Joar Lassesen and students from Charlottenlund Videregående skole in Trondheim (NO) greatly supported us during the construction of the prototype. The laboratory team at SINTEF Community in OSLO supported us during the measurement in Oslo.

References

[1] ISO10140-3:2010. Acoustics — Laboratory measurement of sound insulation of building elements — Part 3: Measurement of impact sound insulation.
[2] Ljunggren F, Simmons C, Öqvist R. Correlation between sound insulation and occupants' perception – Proposal of alternative single number rating of impact sound, part II. Appl Acoust 2017;123:143–51.
[3] Rayleigh JWSB. The theory of sound. New York: Dover Publications; 1945.
[4] Hashimoto N. Measurement of sound radiation efficiency by the discrete calculation method. Appl Acoust 2001;62(4):429–46.
[5] Heckl M. Radiation from plane sound sources. Acta Acustica United Acustica 1977;37(3):155–66.
[6] Revel GM, Rossi GL. Sound power estimation by laser Doppler vibration measurement techniques. Shock Vib 1998;5(5–6).
[7] Roozen NB, Labelle L, Rychtáriková M, Glorieux C. Determining radiated sound power of building structures by means of laser Doppler vibrometry. J Sound Vib 2015;346:81–99.
[8] Santoni A, Fausti P, Schoenwald S, Tröbs H-M, editors. Sound radiation efficiency measurements on cross-laminated timber plates. INTER-NOISE and NOISE-CON Congress and Conference Proceedings; 2016: Institute of Noise Control Engineering.
[9] Santoni A, Schoenwald S, Van Damme B, Fausti P. Determination of the elastic and stiffness characteristics of cross-laminated timber plates from flexural wave velocity measurements. J Sound Vib 2017;400:387–401.
[10] Schoenwald S, Vallely S, Tröbs H-M. Advanced methods to determine sound power radiated from planar structures. J Acoust Soc Am 2017;141(5):3713.
[11] Kohrmann M. Numerical methods for the vibro-acoustic assessment of timber floor constructions [Dissertation]: Technische. Universität München; 2017.
[12] Marchetto C, Maxit L, Robin O, Berry A. Vibroacoustic response of panels under diffuse acoustic field excitation from sensitivity functions and reciprocity principles. J Acoust Soc Am 2017;141(6):4508–21.
[13] Conta S, Homb A. Sound radiation of hollow box timber floors under impact excitation: an experimental parameter study. Appl Acoust 2020;161:107190.
[14] Vigran TE. Building acoustics. CRC Press; 2014.
[15] Cremer L, Heckl M, Petersson BA. Structure-borne sound: structural vibrations and sound radiation at audio frequencies. Springer; 2005.
[16] Bies DA, Hansen C, Howard C. Engineering noise control. CRC Press; 2017.
[17] Williams EG, Maynard JD. Numerical evaluation of the Rayleigh integral for planar radiators using the FFT. J Acoust Soc Am 1982;72(6):2020–30.
[18] Fuller CC, Elliott S, Nelson PA. Active control of vibration. Academic Press; 1996.
[19] Maynard JD, Williams EG, Lee Y. Nearfield acoustic holography: I. Theory of generalized holography and the development of NAH. J Acoust Soc Am 1985;78(4):1395–413.
[20] Conta S, Homb A, editors. Challenges and limitations using the Integral Transform Method to obtain the impact noise level of timber floors. Euronoise 2018; 2018; Creta.
[21] Williams EG. Chapter 2 - Plane Waves. Fourier Acoustics. London: Academic Press; 1999. p. 15–87.
[22] Squicciarini G, Thompson DJ, Corradi R. The effect of different combinations of boundary conditions on the average radiation efficiency of rectangular plates. J Sound Vib 2014;333(17):3931–48.
[23] Davy JL, Mahn JP, Guigou-Carter C, Villot M. The prediction of flanking sound transmission below the critical frequency. J Acoust Soc Am 2012;132(4):2359–70.

Paper #4

Applied Acoustics 161 (2020) 107190

Contents lists available at ScienceDirect

Applied Acoustics

journal homepage: www.elsevier.com/locate/apacoust

Sound radiation of hollow box timber floors under impact excitation: An experimental parameter study

Simone Conta [a,*], Anders Homb [a,b]

[a] NTNU, Department of Civil and Environmental Engineering, 7491 Trondheim, Norway
[b] SINTEF Community, 7465 Trondheim, Norway

ARTICLE INFO

Article history:
Received 17 September 2019
Received in revised form 12 November 2019
Accepted 16 December 2019

Keywords:
Timber hollow-box floor
Experimental modal analysis
Integral transform method
Radiated sound power
Impact noise level

ABSTRACT

The timber building industry is developing building systems for urban buildings with open architecture based on long span floor systems. Span length can be increased with constant cross section by combining stiff floor elements e.g. hollow-box floors with supports that provide high rotational stiffness. Detailed knowledge of the vibroacoustic behavior of such a system is not available and is needed to design buildings that fulfill the requirements in an economic and sustainable way. We set up a prototype and performed experimental investigations to identify the modal properties of such a system and to gain understanding of the sound radiation properties under impact excitation. The measurements were performed in an industrial hall using experimental modal analysis (EMA) and the Integral Transform method (ITM). The results highlight the limitation of standard acoustic laboratories and show the importance of using advance measurement methods to acquire reliable data. The size of the element and the boundary condition clearly affect the radiated sound power at low frequencies. Sound radiation can be efficiently reduced above 50 Hz by using traditional strategies such as gravel in the cavity of the floor elements. Additionally, insights about the ITM are presented, showing that symmetry cannot be exploited and that there is no requirement for a baffle when impact excitation is under investigation.

1. Introduction

Hollow core slabs are popular when long span is required and are widely used in urban buildings with the most different purposes, including commercial, office and apartment buildings. The timber building industry is developing hollow box floor systems to offer an alternative to hollow core concrete slabs. Development seems to be driven by structural requirements and little literature is available on the acoustic properties [1–3]. More detailed knowledge is crucial if acoustic requirements shall be fulfilled in an efficient and sustainable way in a building typology that is increasingly important in our ever growing and more dense cities.

Hollow box timber floors can reach long span at competitive floor height and with efficient material consumption compared with for instance massive CLT timber floors [4–5]. In order to fulfil acoustic requirements, the hollow volume of these floor elements can be used either to integrate acoustic materials as for example absorbing materials (mineral fibres), additional mass (gravel, concrete) or to install more advanced elements such as mass tuned damper. Several large companies (e.g. Lignatur, StoraEnso [6], MetsäWood [7], Moelven) designed their own products in this category and carried out the development of these floor systems, but there is a lack of public acoustic knowledge and literature on this subject.

Malo [8] showed that stiff end restraints can be exploited to achieve longer span with constant cross section. This has clear structural and economic advantages, but the acoustic implications were not investigated before.

The Norwegian research project WOODSOL aims at developing mid-rise timber buildings (up to 10 stories), based on stiff hollow box floor elements combined with moment resting frames [9] and offers a chance to deepen the knowledge on this subject. The floor elements are hollow boxes partly filled with gravel resulting in a strongly inhomogeneous object, featuring a heavily damped plate on the bottom and a lightly damped plate on the top. The floor elements are combined with a connection system that aims at being moment resisting. The connectors are mounted at the corner of the floor element, giving, in principle, a clamped fixation of the corners.

This results in unique boundary conditions for the sound radiation of the floor elements, which need to be investigated for under-

* Corresponding author at: Institutt for konstruksjonsteknikk, NTNU, Richard Birkelands vei 1A, 7491 Trondheim, Norway.
E-mail address: Simone.Conta@ntnu.no (S. Conta).

https://doi.org/10.1016/j.apacoust.2019.107190
0003-682X/

standing the acoustical behaviour of the structure and – in a second step – serve as basis for the computational models. To accomplish this purpose, we set up an extensive experimental campaign on a prototype of the system.

The main goals of the campaign were: 1) investigate the modal properties of the floor element, 2) investigate the sound radiation properties of the floor element, 3) identify governing factors and possibility to improve impact sound insulation (e.g. stiffness, additional mass), 4) investigate the vibration transmission between floor elements and columns and 5) determine the influence of the connecting detail between floor elements. In this paper, we focus on the experimental investigation, presenting the adopted measurement methods and the results related to the floor elements sound radiation properties (items 1 and 2).

We investigated the sound radiation focusing on impact sound at low frequencies, expecting here the main challenges due to the long span and lightweight properties of the floor elements. Due to the size of the elements, the interest in the specific mounting system and the frequency range of interest, we could not perform ordinary laboratory measurements in a standard acoustic floor test facility. We therefore used two methods to investigate the vibroacoustic properties of our setup; 1) an experimental modal analysis (EMA) to study the modal behaviour and 2) the measurement method denominated *Integral transform method (ITM)* to study the radiated sound power. Various methods are then available to calculate the impact noise level from the radiated sound power (see section 5). We wanted to gather measurement data that eventually allow the comparison of the acoustic performance of the floor element (i.e. the impact noise level L_n) with other documented construction available in literature or common in the practice. This led to the choice of a tapping machine as excitation source and the selection of excitation positions according to the standard ISO16283 [10]. For the data presented in this paper, the frequency range was set from 20 Hz to 400 Hz. The upper frequency limit was chosen considering the requirement of the ITM method (see section 3.2.2.2), its implications in terms of time resources and a reasonable overlap with data available in literature.

This paper is organized as follow: section 2 describes the measurement object, focusing on the boundary conditions (2.1), the floor elements (2.2) and the mounting system (2.3). In section 3, the methods are introduced along with the specific experimental setup and the measurement program is presented (3.3). In section 4, we present and discuss the measurement results starting from the basic properties and then looking at the effect of specific factors on the sound radiation. In section 5, we briefly present how the observations of the radiated sound power can be interpreted in terms of impact noise level. Finally, in section 6, we present a summary of our findings. Two appendices address two questions related to the ITM method and its application on this specific setup. Appendix A presents the investigations related to the effect of the airborne excitation of the lower plate of the floor element. Appendix B presents the results showing that symmetry considerations cannot be exploited to reduce the measurement time when using the ITM method.

2. Measurement object

2.1. The WOODSOL building system (boundary conditions)

The Woodsol building system is a frame construction system with the following special features: 1) the frame is moment resisting in one direction, 2) the floor elements are of type *hollow box, 3)* the stiffness of the floor element is exploited in the frame structure to achieve moment resisting capacity.

The Woodsol frame is made of massive timber components, i.e. glulam columns. The principle is shown in the sketch in Fig. 1. In Fig. 2, we show the prototype of the system we built to perform several acoustic investigations, including part of the measurement presented in this paper.

In the prototype the columns were 5.2 m high and have a cross section with dimension 0.40 m × 0.45 m. The material used was glulam GL30c from Moelven. The floor elements were installed to the columns with the bottom flange 2 m above the laboratory floor. The columns were installed to the floor by means of a pin connection with the free rotational axis perpendicular to the floor element's longitudinal direction. This is also the direction where the frame is expected to be moment resisting. The columns were braced on top by means of aluminum profiles (not shown in the picture). In the prototype two floor elements shared the central columns. The floor elements were not connected to each other at any other point. In the following we will refer to the prototype setup as: "*on columns* boundary condition". This could be nearly considered as clamped at the corners, whereas this definition is not rigorous since a) the connection has a finite rotational stiffness [9] and b) the frame is moment resisting only around two axis, while the third one is undefined (i.e. rotation around one axis has no controlled constraints).

In order to understand the effect of the frame system on the modal and acoustical behavior of the floor elements, reference measurements with "*free-free* boundary conditions" were also performed. *Free-free* boundary conditions were achieved by installing the floor elements on air bellows (Figs. 3 and 4). One air bellow was placed at each corner of the floor element. The air bellows rested either on the floor of the lab or on massive blocks giving enough clearance (80 cm) to work under the floor element. The air bellows (Parker air bellows series 9109, type 6" × 1) were inflated to 6 bar giving natural frequencies for the rigid body motion at 3 Hz to 5 Hz. This was about 4 times lower than the first mode of the floor elements.

2.2. Floor elements

The investigated floor elements are of a hollow box type. The design used here is the optimized cross section, as described in [12] and shown in Fig. 5. The cross section has a total height of 0.5 m and was designed for a span length of 9 m to 10 m. We built

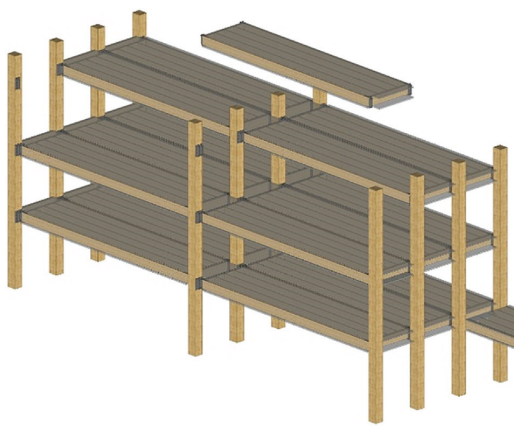

Fig. 1. Woodsol building system: frame construction based on moment resisting connection between continuous columns and stiff floor elements [11].

Fig. 2. Woodsol prototype; setup used for the on columns BC measurements, photo: SINTEF/A.-L. Bakken.

Fig. 3. Free-free boundary conditions: floor element installed on air bellows.

Fig. 4. Free-free boundary conditions: detail showing the air bellows.

prototype elements with lengths 9 m, 4.7 m and 3.7 m. All of them have the same cross section to ease the comparison of the results.

The top and bottom plates are laminated veneer lumber (LVL) panels with thickness 43 mm and 61 mm respectively. The outermost stringers are glulam GL30c, while the inner ones are glulam GL28c [11]. The materials properties are given in Table 1.

The top and bottom plates are glued to the stringers. Screws are used in the horizontal connections and are also used to ensure structural safety in vertical direction. A strong glued connection ensures no relative movements between components (composite effect $\gamma = 1$ to describe it according to Eurocode 5 [13]), while a screwed connection allows small relative movements ($0 < \gamma < 1$). In the Eurocode 5 [13] following relation is given, which describes how the composite effect affects the effective bending stiffness B_{eff}:

$$B_{eff} = \sum_{i=1}^{3} E_i I_i + \gamma_i E_i A_i a_i^2 \quad (1)$$

with E_i Young's modulus and I_i second moment of inertia of the i'th component in the cross section (e.g. i = 1 top plate, i = 2 vertical element, i = 3 bottom plate), A_i is the cross-sectional area of the i'th component and a_i is the distance of the component from the neutral axis.

To ensure full composite effect of the joint with the type of glue used, a line pressure between 0.6 N/mm^2 and 1.0 N/mm^2 is required [14]. The manufacturing process of the elements has been different for practical reasons and led probably to different composite effects in the three floor elements build. The two considered elements were built by two different groups of students in two different facilities, with different methods. During the gluing process of the 9 m element, the pressure was applied by means of screws. This ensures good control of the process and an applied line pressure close the required range. For the 4.7 m element, the pressure was applied by adding masses on top of the components to be glued. The resulting applied pressure is expected to have been as low as 0.01 N/mm^2.

In the work of Bjørge and Kristoffersen [12] the effective bending stiffness in longitudinal direction is determined analytically ($B_{L,\infty}$ = 1.6E8 Nm^2, $\gamma = 1$) and by means of deflection measurements on the 9 m element ($B_{L,eff}$ = 1.3E8 Nm^2, $\gamma = 0.75$). Based on the results presented in section 4.4, we estimated the longitudinal bending stiffness for the 4.7 m element as approximately $B_{4.7m,-eff}$ = 6.4E7 Nm^2, $\gamma = 0.19$.

The cavity can be filled with gravel or absorbing material according to the acoustic requirements. We performed measurements with two configurations: empty element and cavity filled with 100 kg/m^2 gravel. The gravel was packed in bags to ease the installation (Fig. 6). The mass of the elements is given in Table 2.

2.3. Connectors

The WOODSOL connectors are designed aiming for a rotational stiffness in the range 8000 kNm/rad < K_θ < 13500 kNm/rad [9].

The connector is made by two metal parts. One metal part is fixed to the column, the other to the floor elements. Both are installed by means of threaded rods as shown in Fig. 7 [32]. The two metal parts are connected by friction bolts. The picture in Fig. 8 shows the current prototype version. Experimental investigations and improvement of the connection are ongoing.

3. Measurement methods and experimental setup

3.1. Experimental modal analysis (EMA)

3.1.1. EMA measurement principle

Experimental modal analysis (EMA) is a well-established measurement method. In the following we shall document the tools and the experimental setup used and highlight specific features. However, we will not present any background since this is outside

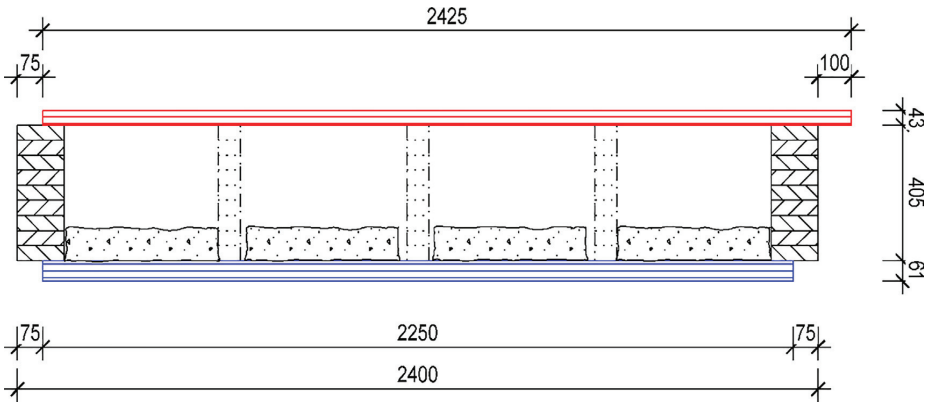

Fig. 5. Floor element cross section [11].

Table 1
Material parameters [12].

	ρ [kg/m3]	E1 [MPa]	E2 [MPa]	E3 [MPa]	G12 [MPa]	G13 [MPa]	G23 [MPa]	ν12	ν13	ν23
GL30c	430	13 000	300	300	650	650	65	0.02	0.02	0.30
LVL (Kerto-Q)	510	10 500	2 400	130	600	120	22	0.02	0.02	0.68

Fig. 6. Element cavity with the gravel bags.

Table 2
Weight of the elements and weigth of the added gravel.

Length	Timber weight (empty element)	Gravel (100 kg/m^2)
9.0 m	2400 kg	–
4.7 m	1300 kg	1200 kg
3.7 m	900 kg	900 kg

the scope of this paper, although literature is available on the subject [17,16].

The measurements were performed using the roving hammer technique with several reference accelerometers. The measurement procedure was based on 1) data acquisition using a multichannel acquisition system and 2) post-processing of the data (see Section 3.1.3).

3.1.2. EMA excitation and response acquisition

On the 9 m floor, a measurement grid with 10 × 5 points (size 0.56 m × 0.98 m) and 4 reference accelerometers were used. On the 4.7 m floor, a measurement grid with 9 × 5 points (size 0.55 m × 0.56 m) and 7 reference accelerometers were used. The measurement grid was aligned with the glulam beams and stringer. Both excitation and response acquisition were performed on the top side of the floor for practical reasons (Fig. 9a). This must be kept

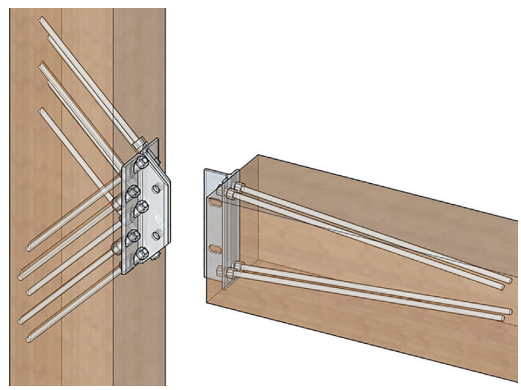

Fig. 7. Principle of the connector showing the threaded rods and the two connecting parts (graphic: A. Vilguts, NTNU).

in mind when comparing the results from the EMA measurements with the ITM results. At frequencies up to at least 100 Hz the vibrational behavior of the floor is dominated by the global modes (see section 4.1) and the upper and lower surface of the floor might be considered equivalent. With increasing frequency this assumption is not valid any longer, since local modes will behave differently on the top and lower surface.

An impact hammer with soft rubber cap was used to excite the structure. At least three impacts at each point of the grid were recorded as time signals using a multichannel acquisition system. The time between impacts was approximately 10 s allowing for enough window length to avoid leakage.

Excitation, response acquisition and analysis were limited to the vertical components.

3.1.3. EMA data analysis

The data were post processed using the Abravibe toolbox [15] in Matlab.

Fig. 8. Picture of the connector installed between the floor element and the column (photo: SINTEF/A.- L. Bakken).

The first step here was the impact processing. The optimal settings for triggering level, pretrigger, block size and windowing of both the force and acceleration signal were defined with help of the Abravibe toolbox graphical user interface. Then, the frequency response functions (FRF) were built by manually selecting the impacts to be used, based on visual check of the FRF and evaluation of the coherence function. The quality of the calculated FRFs was eventually checked by verifying the reciprocity of the FRFs at the reference points.

The poles and the modal participation factors were computed using the polireference time domain method (PTD). Based on the stabilization diagram, the reference positions that gave clearer mode functions were selected for the further steps. The Least Squares Frequency Domain (LSFD) method was used to estimate the mode shapes. The comparison between the measured FRF and those calculated by means of the extracted modal parameters is the first quality check. Moreover, the AutoMAC criterion was used to assess how well the identified modes are decoupled. Finally, the extracted mode shapes were checked visually for plausibility using the animation function of the toolbox.

3.2. Integral transform method (ITM)

3.2.1. ITM measurement principle

The integral transform method is based on the principle of a plane radiator as a sum of plane waves [17] and its theoretical formulation has been long used [18]. In recent years, it is gaining popularity thanks to the increasing availability of multichannel acquisition systems and scanning laser-vibrometers. We report here the main equations for ease of reference but otherwise refer to our previous paper for a compact overview of the method [19] or to the literature for more in depth insights [20–22].

The integral transform method is a hybrid method comprising of three main steps; 1) the measurement of vibration velocity on a relatively fine grid on the sound radiating surface, 2) a two-dimensional Fourier transform transforming the data in the wavenumber domain and 3) the calculation of the radiated sound power in the wavenumber domain using following equation [20]:

$$P[\gamma] = \frac{1}{2}\frac{\rho_A c_A}{4\pi^2}\mathrm{Re}\left[\sum_{\alpha=1}^{M_\alpha}\sum_{\beta=1}^{M_\beta}\mathbf{K}[\alpha,\beta,\gamma]\cdot\left|\hat{v}[\alpha,\beta,\gamma]\right|^2\Delta x^2\Delta y^2\right]\Delta k_x\Delta k_y \tag{2}$$

where: $\hat{v}[\alpha,\beta,\gamma]$ is the vibration velocity in the wavenumber domain, calculated by means of a 2D Fourier transformation for the coordinates α, β in the wavenumber domain at the frequency step γ. Δx and Δy is the distance between measurement points respectively in x and y direction, $M_\alpha = z_p\frac{l}{\Delta x}$ and $M_\beta = z_p\frac{b}{\Delta y}$ are the number of samples in the wavenumber domain, z_p is a zero padding factor required to achieve sufficient resolution, l and b are the dimensions of the plate, $\Delta k_x = \frac{2\pi}{z_p l}$ and $\Delta k_y = \frac{2\pi}{z_p b}$ are the sampling intervals in the wavenumber domain. The terms of the matrix **K** are:

$$\mathbf{K}[\alpha,\beta,\gamma] = \frac{k_A[\gamma]^2}{\sqrt{\left(k_A[\gamma]^2 - k_x[\alpha]^2 - k_y[\beta]^2\right)}} \tag{3}$$

where k_A is the wavenumber of the wave propagating in air, k_x and k_y are the wavenumber components in x and y direction of the waves propagating in the plate.

An advantage of the integral transform method is that the radiation efficiency σ follows directly from the equations above (adapted from [20]):

$$\sigma[\gamma] = \frac{\mathrm{Re}\left[\sum_{\alpha=1}^{M_\alpha}\sum_{\beta=1}^{M_\beta}K[\alpha,\beta,\gamma]\cdot\left|\hat{v}[\alpha,\beta,\gamma]\right|^2\Delta x^2\Delta y^2\right]}{\sum_{\alpha=1}^{M_\alpha}\sum_{\beta=1}^{M_\beta}\left|\hat{v}[\alpha,\beta,\gamma]\right|^2\Delta x^2\Delta y^2} \tag{4}$$

The use of the Fourier transformation and the finite size of the measurement object pose some limits of validity to the method, which are discussed in section 3.2.2.2 along with the chosen grid size.

3.2.2. ITM measurement setup

3.2.2.1. Installation of the test object. The test object was installed in an industrial hall as described in section 2.1. As is evident from Figs. 2 and 3, there were no partitions separating the volume above the floor element and the volume below. This raised two related questions: 1) can we apply the ITM method, which was originally developed for a baffled plane sound radiator? 2) How does the airborne excitation from the noise radiated by the upper part of the floor element affect the vibration velocity on the bottom of the element? We can apply the ITM method without a baffle only if the airborne excitation generates a vibration velocity at least 10 dB below the vibration velocity level generated by the direct impact excitation. We approached these issues experimentally by comparing the vibration velocity on the bottom plate generated by the tapping machine and by airborne excitation with comparable sound pressure level. The results show that if impact excitation is considered, the airborne excitation does not significantly affect the vibration velocity on the bottom plate and hence the ITM method can be applied. The details are presented in appendix A.

3.2.2.2. ITM measurement grid. The ITM method uses a 2-D Fourier transformation to convert the vibration velocity field from the space domain to the wavenumber domain. The Shannon criterion must be fulfilled in order to obtain valid results. This imposes a maximum measurement grid size as described by following equations:

$$\Delta x < \frac{\lambda_{x,min}}{2},\quad \Delta y < \frac{\lambda_{y,min}}{2} \tag{5}$$

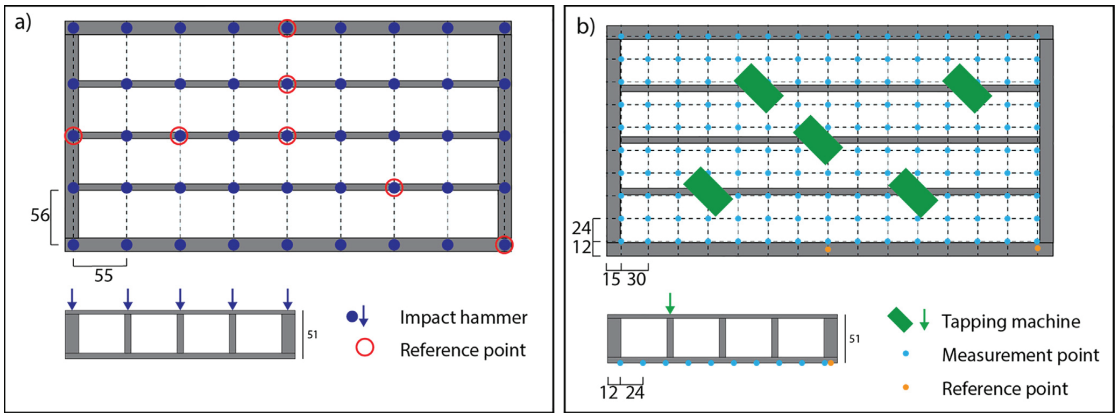

Fig. 9. a) EMA excitation and measurement positions, b) ITM excitation and measurement positions.

with $\lambda_{x,min}$ and $\lambda_{y,min}$ the wavelength in the plate at the highest frequency of interest. Since the relation between wavelengths λ_x, λ_y and frequency include the bending wave speed, and this is not readily known, there is an obvious challenge here. We opted for an educated guess by using plausible numbers and by comparing with existing literature values (see [19] for more details). In addition, after the first measurements were performed, we confirmed our assumptions by evaluating the bending wave speed from the wavenumber spectrum (see section 4.2, Fig. 12).

The resolution of the measurement in terms of wavenumbers is fixed by the dimensions of the measurement object. In our case:

$$\Delta k_x = \frac{2\pi}{l} = 1.33\frac{rad}{m}, \quad \Delta k_y = \frac{2\pi}{b} = 2.6\frac{rad}{m} \tag{6}$$

The use of zero padding is required in the numerical implementation to artificially increase the resolution [20].

We defined a measurement grid with 10 × 16 points with spacing 0.24 m × 0.30 m, giving following maximum wavenumbers within the Shannon criterium:

$$k_{max,x} = \pi/0.30\ \text{m} = 10.5\ \text{rad/m}$$
$$k_{max,y} = \pi/0.24\ \text{m} = 13.1\ \text{rad/m} \tag{7}$$

Looking at the dispersion relation after the measurements were performed (Section 4.2, Fig. 12), the frequency range where the measurements are valid can be established. We obtained following maximum frequencies:

$$f_{x,max} \cong 800Hz, \quad f_{y,max} \cong 500Hz \tag{8}$$

The weakest direction represents the theoretical limit of the method, in this case 500 Hz. However, it shall be noted that this theoretical limit might not be as strict depending on the specific radiation properties of the measurement object as discussed in [20].

The strong requirement on the grid size when using the Integral Transform Method to determine the radiated sound power leads to a high number of measurement points and hence to a long measurement time. One might argue that symmetry consideration could reduce significantly the measurement time and measurement costs. It is therefore important to verify if this concept could be applied. We performed our measurements on the 4.7 m elements covering the entire surface of the element. An investigation of the effect on the results produced by exploiting the symmetry was lightly verified by using different sets of the acquired data. The procedure and results are presented in appendix A. The results lead to the conclusion that symmetry cannot be exploited when using the ITM method. This confirms what suggested by [22] and proves wrong the assumption made by the author in [19]. These results also match the observations made by Hashimoto [23] while evaluating the Discrete Calculation Method (DCM), which share the same challenge as the ITM.

3.2.2.3. ITM excitation and response acquisition. In Fig. 9b, we show the excitation and measurement positions used for the ITM measurements.

The excitation was made by the ISO standard tapping machine positioned at five different locations on top of the floor element according to the requirement of the ISO16283 [10].

The vibration velocity was measured by integrating the acceleration signal measured by accelerometers. We used 12 accelerometers simultaneously. Two were kept fixed for phase reference and 10 were moved sequentially to cover all the rows of the measurement grid.

The acceleration was measured on the bottom of the floor element and only in the vertical direction, since this is the direction that dominates the sound radiation.

3.2.3. ITM procedure

For each configuration, the measurement procedure was as follows: 1) Excite at position one, 2) Record acceleration at row 1, 3) Move tapping machine to the next four positions, while recording the data at each position, 4) Move the accelerometers to the next row and repeat the steps 1 to 4.

The analysis was made in post processing. The radiated sound power was calculated individually for each excitation position and then averaged energetically as indicated in the standard.

3.3. Measurement program

The extensive measurement program shown in Table 3 was carried out to achieve the goals stated in the introduction. It includes several different configurations based on the three parameters: floor length, boundary conditions and additional mass. On each configuration, both an experimental modal analysis with a rowing hammer (EMA) and the measurement of the radiated sound power (ITM) under excitation by the tapping machine were performed.

Table 3
Measurement program. Some of the configurations were described in the given references.

Measurement	Floor length	Boundary conditions	Additional mass	Refs.
EMA, ITM[1]	9 m	free-free	no	[19,24]
EMA	9 m	clamped	no	[12]
EMA	9 m	simply supported	no	[12]
EMA, ITM	4.7 *m*	free-free	a) no b) gravel, 100 kg/m^2	
EMA, ITM	4.7 m	on columns	a) no b) gravel, 100 kg/m^2	
EMA, ITM	3.7 m	free-free	gravel, 100 kg/m^2	
EMA, ITM	3.7 m	on columns	gravel, 100 kg/m^2	

[1]) Data are available for only half of the floor element.

4. Measurement results

4.1. Frequency response functions and mode shapes

In this section, we present the general form of the recorded frequency response functions (FRF) and we establish the correspondence between the peaks in the FRF and the mode shapes. The respective natural frequencies and damping values are given in Table 4.

The diagrams in Fig. 10 show the FRFs magnitude measured on the 4.7 m floor element without additional mass mounted with free-free BC (upper diagram) and mounted on columns (lower dia-

Table 4
Natural frequency f and damping ζ of the identified modes on the 9 m and 4.7 m element with and without gravel installed with free-free BC and on columns BC. *) indicates uncertain data; -) indicates that the mode was not detected.

9 m element			4.7 m element								
Without gravel				Without gravel				With gravel			
free- free				free- free		on columns		free- free		on columns	
Mode	*f (Hz)*	*ζ (%)*	*Mode*	*f (Hz)*	*ζ (%)*	*f (Hz)*	*ζ (%)*	*f (Hz)*	*ζ (%)*	*f (Hz)*	*ζ (%)*
1st torsional	26.0	1.0	1st torsional	40.5	1.8	–	–	36.1	1.7	47.1	4.2
1st longitudinal	31.9	0.5	**1st transverse**	56.5	2.1	59.3	2.4	38.4	1.0	40.7	2.5
2nd torsional	42.1	0.8	2nd torsional	68.2	1.1	94.6	2.1	58.9*	3.6	–	–
1st transverse	42.7	1.0	**1st longitudinal**	81.3	1.2	101.3	1.7	57.3	1.8	64.0*	–
Antisymmetric	65.7	1.7	2nd transverse	85.0	1.1	81.3	1.8	48.5	1.5	54.5	4.9
2nd transverse	71.9	0.9	Antisymmetric	103.0	2.0	–	–	–	–	–	–
2nd longitudinal	72.3	1.7	3rd transverse	115.6	1.1	–	–	–	–	–	–
Higher order	75.0	0.8	Higher order	132.9	2.0	–	–	–	–	–	–
Higher order	95.5	0.8	Higher order	136.9	1.5	–	–	–	–	–	

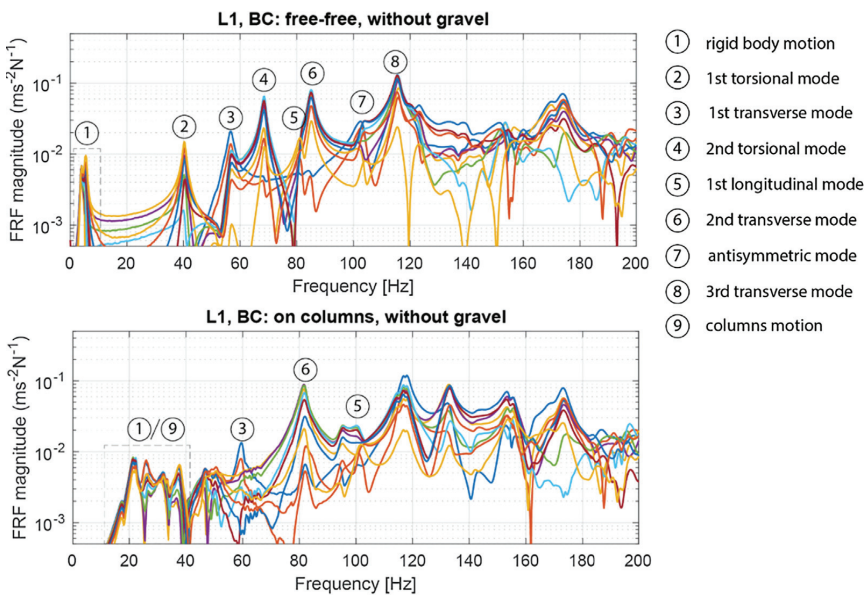

Fig. 10. Frequency response functions measured on the 4.7 m element without gravel showing the identified vibrational modes: the upper diagram presents the results obtained with free-free boundary conditions; the lower diagram presents the results obtained with element on columns.

gram). The numbers above the peaks of the FRFs identify the corresponding vibrational mode, which are graphically presented in Fig. 11. A detailed analysis and discussion of this data is presented in Section 4.3.

At this stage, we highlight the features indicated with the numbers 1 and 9. In the upper diagram, we recognize at least two main peaks, grouped under the number 1. They describe the motion of the floor as rigid body on the air bellows. In the lower diagram, the group of peaks at the frequencies between 20 Hz and 40 Hz is marked with the numbers 1/9. Some of the peaks here correspond to the vibrational modes of the prototype's columns while others describe the rigid body motion of the floor on the connectors. Even if the connectors present a high rotational stiffness, they exhibit a relatively soft behaviour in the vertical direction.

4.2. Bending waves dispersion curve

The diagram in Fig. 12 shows the vibration velocity wavenumber spectrum in the format k_x (longitudinal direction) versus frequency at $k_y = 0$, measured on the 4.7 m element on free-free boundary conditions, without additional mass. At each frequency step the amplitude was normalized to the maximum in the same frequency step. Data are shown in dB. The measurement resolution was $\Delta k = 1.34$ rad/m. The wavenumber spectrum was calculated using a zero padding factor $z_{pad} = 4$, corresponding to $\Delta k = 0.33$ r ad/m . The data are presented with a frequency resolution $\Delta f = 2$ Hz. The data is presented up to 800 Hz, since no major aliasing effects were observed up to this frequency and the extended frequency range helps assessing the trend.

In the diagram, two curves are overlaid to the measurements data. They were calculated using following relation based on the Mindlin thick plate theory (from [25] which cites [26,27]):

$$k_{B,eff} = 2\pi f \left(\frac{1}{2}\left(\frac{\rho h^3}{12B} + \frac{\rho}{\kappa G}\right) + \frac{1}{2}\sqrt{\left(\frac{\rho h^3}{12B} + \frac{\rho}{\kappa G}\right)^2 + 4\frac{\rho h}{B4\pi^2 f^2} - 4\frac{\rho^2 h^3}{12B\kappa G}} \right)^{\frac{1}{2}} \tag{9}$$

Following symbols and quantities were used: f frequency, ρ density of the material (here calculated as total volume divided by total weight), h height of the element, B bending stiffness, $\kappa = 0.9554$ [28], plate shear modulus $G = 6.5 \times 10^8$ Pa. The curve *"Element"* was calculated with the measured effective bending stiffness as given in Section 2.2. The curve *"Kerto"* was calculated using the Young's modulus of Kerto while the other parameters were left unchanged.

Despite the low resolution in the wavenumber spectrum, it seems appropriate to recognize three different regions: below 200 Hz the element shows a lumped behaviour as suggested by the curve *"Element"* fitting reasonably the measured wavenumber spectrum; above 500 Hz the wavenumber spectrum seems to be dominated by the LVL properties as suggested by the curve *"Kerto"* fitting with increasing agreement the measured data; in between there is a transition zone that do not follow the expected trend from the thick plate theory.

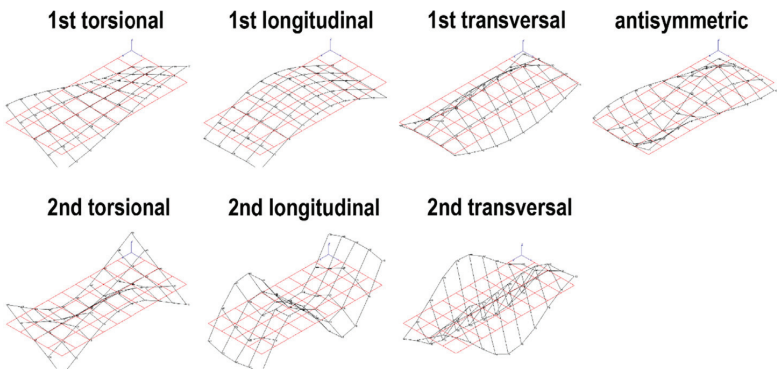

Fig. 11. Identified mode shapes. See Table 4 for the respective frequency and damping information.

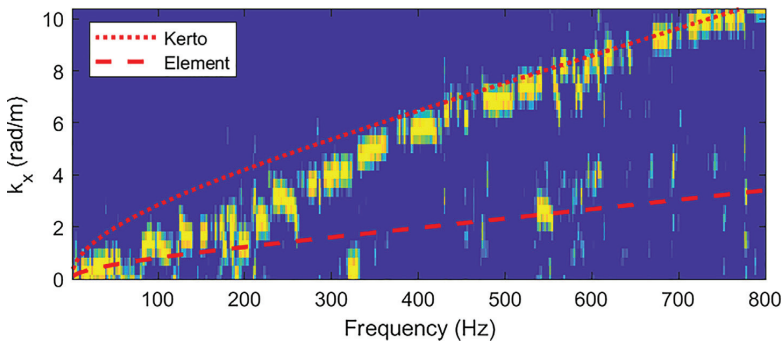

Fig. 12. Wavenumber spectrum of the measured vibration velocity plotted for $k_y = 0$, normalized to the maximum amplitude at each frequency step. Overlaid lines: see text.

4.3. Effect of boundary conditions

Fig. 13 presents a comparison of the frequency response functions (FRFs) measured with different boundary conditions: "free-free" and "on columns". The results are presented for the two configurations a) without additional mass and b) with additional mass (100 kg/m^2 gravel). In each diagram, only a selection of curves is presented, showing the FRFs with highest magnitude. The selection is kept constant among the diagrams. The natural frequencies for the identified modes are listed along with the damping for the two mounting conditions in Table 4.

Below we present a few observations based on the results presented in Fig. 13 and Table 4.

Transversal modes are nearly unaffected by the mounting on the columns (see also Fig. 10) while the amplitude of the torsional modes (e.g. 1st at 40 Hz and 2nd at 70 Hz) is dramatically reduced.

The natural frequency of the 1st longitudinal mode is shifted from 81 Hz (free-free) to 101 Hz (on columns) (see also Fig. 10). This result is surprising since 1) an ideally clamped beam would have the same natural frequency as with free-free boundary conditions and 2) all other support conditions would imply a lower natural frequency compared to free-free or clamped [17]. A possible explanation of the increased natural frequency is that the threaded rods reduce the effective length of the floor by extending the clamping fixture. The result here fits well with a reduction in length of the floor as high as 60 cm, which is the length of the inserted rods. It seems that the connections shift the supporting point approximately half way in the rods, corresponding to 30 cm on each side of the floor. If this result can be confirmed by further investigation, it would imply that a clamped support, as realized in this project, would have two beneficial effects on the achievable span. Firstly, by exploiting the difference between simply supported and clamped and secondly by reducing the effective length of the floor, hereby increasing the achievable span length with constant cross section or conversely allowing a reduction of the cross section for constant span.

Modal damping increases up to a factor of 2 on selected modes (2nd torsional mode).

Finally, above 125 Hz the effect of the boundary conditions is very limited.

Fig. 14 shows the corresponding radiated sound power, again for the two configurations a) without additional mass and b) with additional mass (100 kg/m^2 gravel). Each curve corresponds to the energy-averaged sound power level. The shaded area corresponds to ±σ, where σ is the standard deviation calculated between the measurements at the individual excitation positions.

The data presented in Fig. 14 show that the effect on the radiated sound power is limited to narrow frequency bands corresponding to the missing modes in that frequency band. Without gravel the effect is almost negligible between 40 and 400 Hz. With

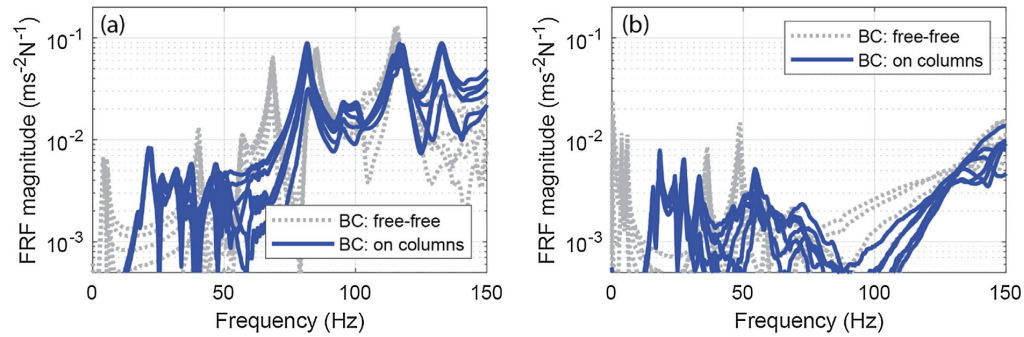

Fig. 13. Frequency response functions for the boundary conditions "free-free" and "on columns". (a) show the effect on empty elements, (b) show the effect on elements filled with 100 kg/m^2 gravel.

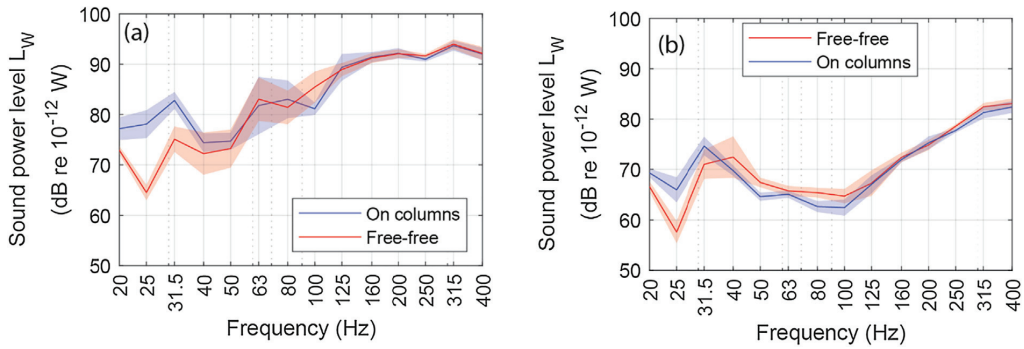

Fig. 14. Radiated sound power for the boundary conditions "free-free" and "on columns". (a) show the effect on elements without additional mass, (b) show the effect on elements with 100 km/m2 gravel as additional mass in the cavity.

gravel, the effect is up to 3 dB sound power reduction in the frequency range from 40 Hz to 100 Hz when mounting the element to the columns.

Below 40 Hz we observe a clear increase of radiated sound power when mounting the element on the columns. This is mainly related to vibrational modes on the undamped columns, which force vibrations on the floor element. It is to clarify if this effect will be also observed in real buildings, where the columns experience more constraints and possibly higher damping.

4.4. Size effect

We start assessing the size effect by looking at the recorded frequency response functions and the position of the identified modes. Fig. 15 shows a selection of the frequency response functions recorded respectively for the 9 m floor and 4.7 m floor (note that this is a subset of the data presented in Fig. 10). Table 4 shows the natural frequencies and damping of the identified modes.

The results in Fig. 15 and Table 4 give a clear indication of which parameters are mainly affected by the change in the length: longitudinal modes are clearly shifted towards higher frequencies when the length of the element is reduced. The frequency of transverse and torsional modes shifts towards higher frequency, by a factor 1.6 ($3/4\pi$). Since the transverse dimension was kept constant, this indicates that the structure stiffens in transversal direction by the effect of the end beams getting closer, when reducing the length of the element.

The shorter floor element experiences a slightly higher modal damping.

Fig. 16 shows the radiated sound power level L_w for the 9 m and the 4.7 m elements. Each curve corresponds to the energy-averaged sound power level. The shaded area corresponds to ± σ,

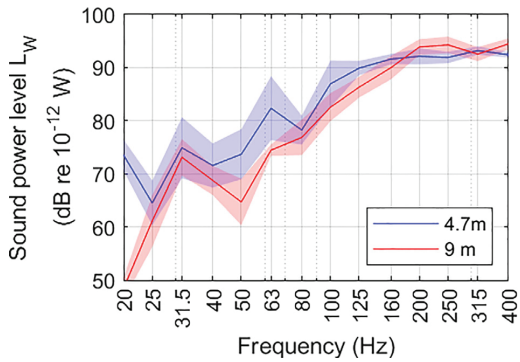

Fig. 16. Radiated sound power measured on the bottom surface of the 9 m and 4.7 m element. Both elements without gravel, BC: free-free. Note that these results are calculated using only half of the bottom surface.

where σ is the standard deviation, calculated between the measurements at the individual excitation positions. Note that these data are based on measurements performed on only half of the bottom surface. The reason for this is that the measurements on the 9 m element were performed at an early stage of the project and the vibration velocity was measured only on half the surface. As stated in section 3.2.2.2, symmetry cannot be exploited when using the ITM method. To keep the results comparable, the analysis has been performed using only half of the measurement surface for both the 9 m and the 4.7 m floor element. In this way, the absolute level of the radiated power is not correct at low frequencies but the comparison yields.

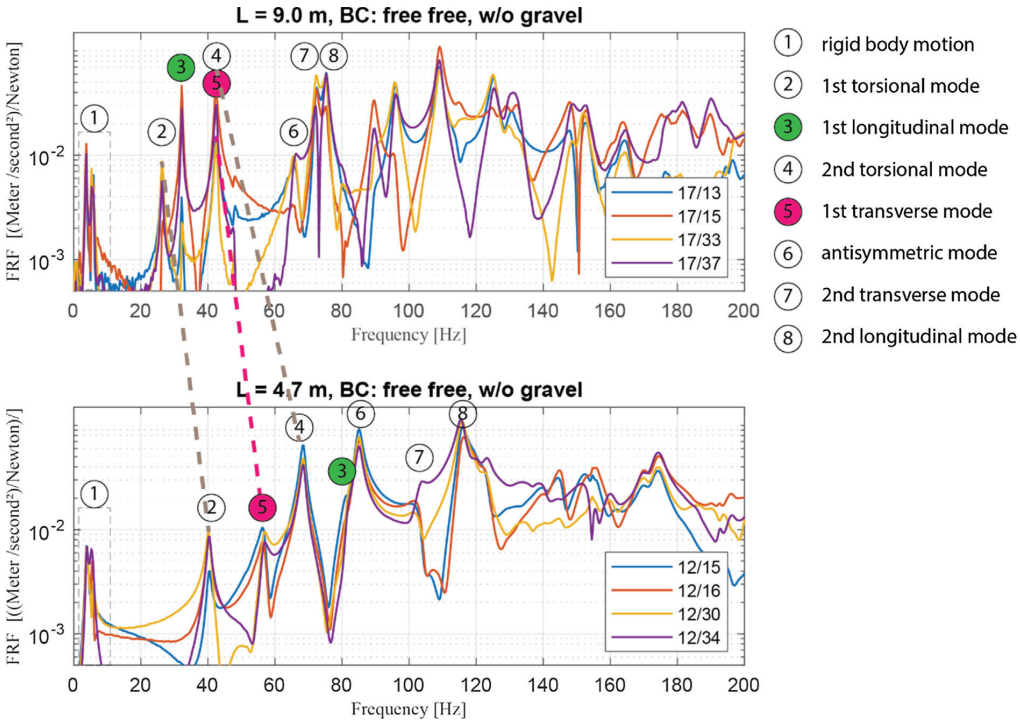

Fig. 15. Frequency response functions measured on the 4.7 m and 9 m element without gravel. The numbers mark the identified modes.

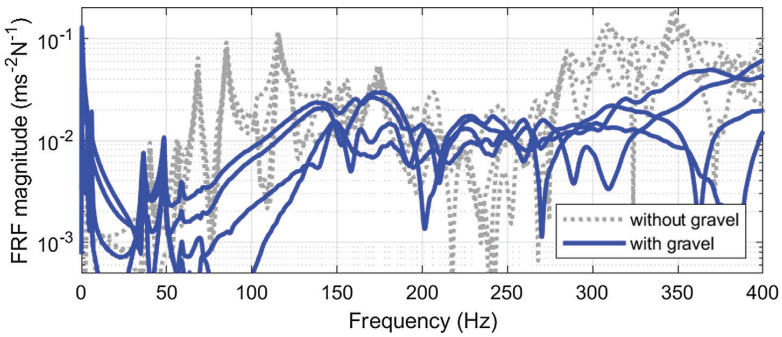

Fig. 17. Measured frequency response functions with the element installed with «free-free» boundary conditions. The frequency response functions measured with (100 kg/m^2) and without gravel in the element are compared.

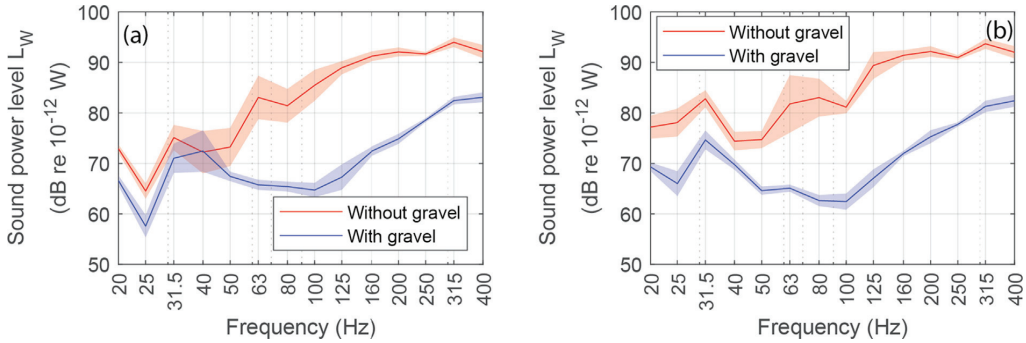

Fig. 18. Radiated sound power measured with and without gravel for the element mounted with (a) free-free BC and (b) "on columns".

Between 40 Hz and 80 Hz the overall L_w for the 4.7 m element is up to 10 dB higher than that for the 9 m element. This seems to relate well with the more even distribution of the vibrational modes in the 4.7 m elements. In the 9 m element there is indeed a clear gap in the FRFs from 43 Hz to 66 Hz.

4.5. Effect of gravel

The effect of additional mass (gravel) on the vibroacoustic behaviour of the floor element was observed best on the 4.7 m floor mounted with "free-free" boundary conditions. The results are presented in Fig. 17. The diagram shows the measured frequency response functions for selected response/excitation combinations with gravel (solid line) and without gravel (dotted line).

The effect of gravel is a strong attenuation of the vibrational modes above 50 Hz and a dramatic increase in damping.

The diagrams in Fig. 18 show the radiated sound power determined with the ITM method with and without gravel, both for free-free boundary conditions and for the floor element mounted on the columns. Each curve corresponds to the energy-averaged sound power level from the five tapping machine positions. The shaded area corresponds to ± σ, where σ is the standard deviation calculated between the measurements at the individual excitation positions.

The results show a reduction of the radiated sound power larger than 10 dB (up to 20 dB) above 50 Hz by adding 100 kg/m^2 gravel in the cavity of the floor elements. A reduction of 5 dB to 10 dB is observed also between 20 Hz and 50 Hz with a minimum at 40 Hz (0 dB with free-free BC), where the 1st torsional mode seems to be unaffected by the additional mass. In the "on columns" case, the increased damping and increased impedance of the floor seem to mitigate the forced vibrations generated by the columns.

5. Impact noise level

The results are presented in this paper in terms of radiated sound power L_w. However, the observed features and level differences can be directly interpreted in terms of impact noise level L_n. When the diffuse field assumption holds (i.e. above the Schroeder frequency), L_n can be calculated with this simple relation [29]:

$$L_n = L_w - 4 \text{ dB} \quad (10)$$

In typical acoustic laboratories for measuring impact noise level, this relation will hold above approximately 150 Hz.

Below the Schroeder frequency, the sound pressure level generated in the receiving room by the radiated sound power has first to be calculated considering the features of the sound field in the measuring room. Only then the impact noise level can be calculated. Roozen [30] investigated this topic, focusing on airborne sound insulation and the same approach could be used here. However, this will affect the absolute levels but not the differences obtained by changing the parameters. This means that the observed differences are directly valid also for the impact noise level.

6. Conclusions

We built a prototype of a building system based on long span hollow-box timber floor elements with moment resisting connec-

tors at the corners. The goal was to gain deeper knowledge of the vibroacoustic behaviour of the system. We performed several experimental investigations focusing on the modal behaviour of the floor elements and the radiated sound power under impact excitation. We used two techniques to obtain our results: experimental modal analysis and Integral transform method. This made it possible to investigate the correct boundary conditions and to show the effect of the size of the element on the measurement results.

Our overall conclusion is that the measured transfer functions and the standard deviation related to the excitation position lead to identify two frequency ranges: a lower one from 20 Hz to 150 Hz with isolated modes and large variance of the measured radiated sound power depending on the excitation position, and an upper one above 150 Hz where the modal density is higher, and the standard deviation is reduced from more than 5 dB to less than 2 dB. Both the effects related to the boundary conditions and those related to the size of the elements are more pronounced in the lower frequency range. Considering that the low frequency range is determining annoyance in wooden lightweight buildings [31], the obtained results are particularly important.

The studied boundary conditions affect the modal behaviour at frequencies below 125 Hz. The amplitude of torsional modes is dramatically reduced, and the natural frequencies of the longitudinal modes are shifted towards higher frequencies. The effect on the radiated sound power strongly depends on the modal distribution and on the modal properties. We observed a reduction of the radiated sound power up to 3 dB in the measurements on columns. This result highlights the need for representative boundary conditions when evaluating building elements in laboratory to achieve good reliability of the data at low frequencies. In our specific setup, the boundary conditions did not have a relevant effect on sound radiations above 125 Hz, since the vibration field was less affected by the boundary conditions with increasing frequency. This cut-off frequency might vary with varying boundary conditions.

The effect of size is mainly related to the distribution of the vibrational modes and reflects clearly in the radiated sound power. Surprisingly, the radiated sound power L_w for the shorter element exceeds L_w for the long element by up to 10 dB between 40 Hz and 80 Hz. Above 160 Hz the differences decrease significantly. This poses again a strong requirement on the element size when measuring the acoustic properties of long span element at low frequencies and highlights a shortcoming of standard acoustic laboratories.

The findings above show the importance of the recently developed advanced measurement methods to determine the acoustic properties of building components such as the ITM used for the measurements in this paper. The findings also show that measurements in standard acoustic laboratories might produce misleading results, when investigating stiff long span structures at low frequencies.

Regarding the effect of additional mass by means of gravel, the conclusion is that it has a dramatic effect on the radiated sound power, specially above 50 Hz, where we observed a reduction largely exceeding 10 dB over wide frequency ranges. For lower frequencies the effect is limited and some modes (e.g. the torsional ones) might not be affected at all by the additional mass.

Finally, the information presented in the appendix provide following important results: 1) the results obtained with this measurement method are not affect by the direct airborne excitation, when impact excitation is used and the hall volume is large enough to avoid excessive sound pressure levels, 2) symmetry cannot be exploited with ITM. Cancellations effects are not accounted for, leading to excessive radiated energy compared to a full measurement. This effect might be negligible in frequency ranges with high modal density, in our case above 160 Hz.

Declaration of Competing Interest

The authors declare that they have no known competing financial interests or personal relationships that could have appeared to influence the work reported in this paper.

Acknowledgments

This study has been carried out within the Woodsol project, a project funded by The Research Council of Norway and leaded by Kjell Arne Malo at NTNU. The project includes research at NTNU and SINTEF Building & Infrastructure and the PhD grant for the first author of this paper, which is gratefully acknowledged. Petra Rüther at SINTEF was work package leader for "WP6 Prototype", which made the prototype possible. Sveinung Nesheim and Aivars Vilguts, both PhD students at NTNU and member of the Woodsol project, were involved in the design and construction of the WOODSOL prototype. Leif Joar Lassesen and students from Charlottenlund Videregående skole in Trondheim (NO) greatly supported us during the construction of the prototype. Kate Layton Matthews provided language support.

Appendix A:. Airborne effect

We are performing sound radiation measurements based on acceleration measurements under tapping machine excitation without confining walls around the excited surface. One natural question that arises is: what is the vibration velocity level caused by the airborne excitation due to the airborne noise generated by the tapping machine itself and being radiated by the upper flange of the excited floor element? Does this affect the vibration velocity level generated directly by the structure-borne excitation?

We answered these questions using following experimental procedure: 1) we first excited the floor element using the tapping machine and measured a) the sound pressure level at 1 m distance, 45 degree elevation from the tapping machine at two positions and simultaneously measured the vibration velocity at 6 positions on the bottom side of the floor element. 3 positions were on the joists and 3 were in between joists. 2) We then calibrated the excitation signal of a half dodecahedron to match the sound pressure level when the dodecahedron was placed at the same position as the

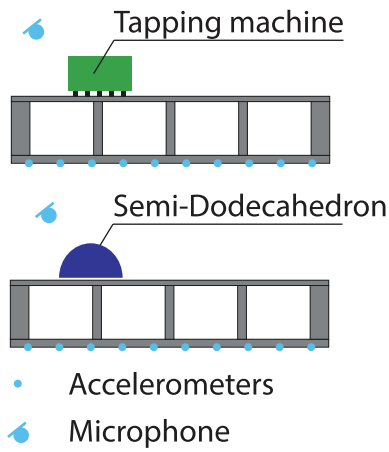

Fig. 19. Graphical representation of the procedure to assess the airborne effect.

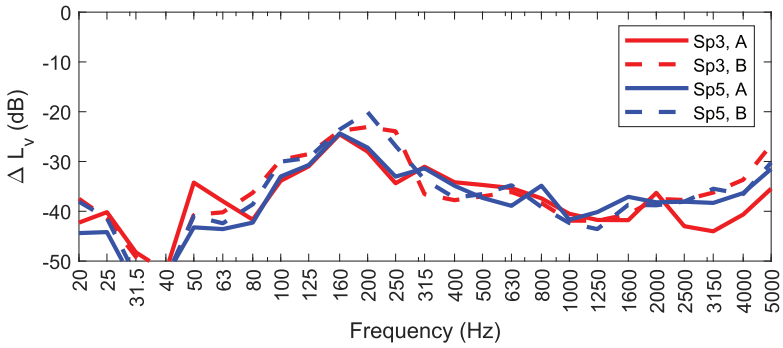

Fig. 20. Measured velocity level difference between excitation by tapping machine and excitation by loudspeaker.

tapping machine. The experimental setup is schematically shown in Fig. 19.

The dodechadron was installed using resilient material to avoid direct structure-borne excitation through the chassis. The vibration velocity on the bottom flange was then measured under the excitation of the calibrated loudspeaker. Finally, the vibration velocity level measured with structure-borne excitation was compared with the one measured with airborne excitation. The whole procedure was repeated for two excitation positions and two accelerometers groups.

In Fig. 20, we present the measurement results showing the effect of the airborne excitation. The curves show the difference between the vibration velocity level measured with airborne excitation by the loudspeaker and with tapping machine excitation. Four curves are presented, corresponding to two different excitation positions and the energetic average over two groups of accelerometers: group A with the accelerometers mounted on the joist, group B with the accelerometers mounted in between joists.

The measured data shows that the level difference is greater than −20 dB in the frequency range from 20 Hz to 5000 Hz. The minimum value of −20 dB is found in the 200 Hz one-third octave band and is probably related to the specific geometry and vibroacoustic properties of the specimen. We do not observe a significant trend related either to the excitation position or to the position of the accelerometers. A level difference greater than 10 dB ensures that the vibration level measured with tapping machine excitation is not affected by the airborne excitation. The safe margin that we found here allowed us to proceed without more detailed investigation. Nevertheless, we point out that this is not a general result and care should be taken whenever measurements are performed in smaller volumes (our hall had greater than 800 m^3) or with a limited height between the floor of the hall and the bottom side of the specimen. Other measurements we performed on a previous setup showed that with only 80 cm between laboratory floor and surface under test the velocity level difference is approaching −10 dB, smaller in some frequency ranges.

Appendix B:. ITM and symmetry

In this appendix we present the procedure that we followed to check if symmetry properties could be exploited when using the ITM method.

We calculated the radiated sound power and compared the respective results using following options:

a) All available data (full floor element),
b) Calculated radiated sound power based on only half data (in longitudinal direction) and add + 3 dB to the results to perform the comparison,
c) Build an artificial measurement data matrix from half the measured data by mirroring the data along the middle axis of the element,
d) Build an artificial measurement data matrix from half the measured data by mirroring the data along the centre point of the element.

The best results were obtained with strategy c) and are presented in Fig. 21.

Fig. 21 shows the radiated sound power level calculated using the measured vibration velocity over the full element (full) and calculated using the data for only half of the element (half) and strategy c). The results are almost identical above 50 Hz but a deviation of up to 6 dB is observed around the 31.5 Hz one-third octave band.

A possible explanation is that the effect relates to the first torsional mode. When measuring on full deck, two dipoles with opposite phase are observed and the effect of their interaction is accurately captured. When measuring only half deck the cancellation effect due to the phase relation cannot be captured and the energy is added rather than canceled.

These results lead to the conclusion that symmetry cannot be exploited when using the ITM method. However, in our case only minor deviations were observed above 50 Hz, suggesting that

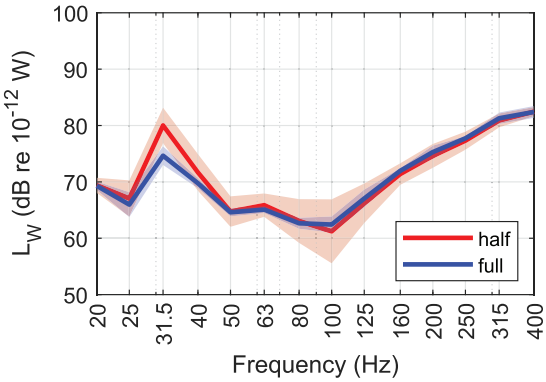

Fig. 21. Radiated sound power level calculated using the measured vibration velocity over the full element (full) and calculated using the data for only half of the element (half). Data source: 4.7 m element, with gravel, bc: on columns.

exploiting symmetry might be acceptable for higher frequencies, i.e. where the modal density is higher.

References

[1] Homb A, Guigou-Carter C, Rabold A. Impact sound insulation of cross-laminated timber/massive wood floor constructions: collection of laboratory measurements and result evaluation. Build Acoust 2017;24(1):35–52.
[2] Bartlomé O, Furrer B, Liebl A, Späh M, Kittel M. Acoustic developments in timber construction. In: Crocker MJ, editor. 21st International Congress on Sound and Vibration 2014 (ICSV 21) Beijing, China: International Institute of Acoustics and Vibration (IIAV); 2014.
[3] Melián Hernández A, Geyer C, Müller A, Pichler J, Sanavi A, editors. Direct and flanking airborne and impact sound insulation of different Swiss timber floor and wall constructions. Forum Acusticum; 2014; Krakow: European Acoustics Association (EAA).
[4] A. Homb Evaluering av lydegenskaper for bærende dekkekonstruksjoner, Woodsolo note no 01/17 2017 Trondheim.
[5] Skaar C, Solem B, Rüther P, editors. Composite floors in urban buildings: Options for a low carbon building de-sign. 6th Forum Wood Building Nordic Trondheim; 2017.
[6] StoraEnso. CLT rib panel brochure, www.storaenso.com, 11/2018.
[7] MetsäWood. Kerto-Ripa brochure 2019 [Available from: https://www.metsawood.com/global/Tools/MaterialArchive/MaterialArchive/Kerto-Ripa-Brochure-UK.pdf.
[8] Malo KA, Köhler J, Vibrations of timber floor beams with end restraints. Structures and Architecture: Concepts, Applications and Challenges–Proceedings of the 2nd International Conference on Structures and Architecture, ICSA; 2013. London: CRC Press.
[9] Vilguts A, Malo KA, Stamatopoulos H. Moment resisting frames and connections using threaded rods in beam–to-column timber joints. Seoul: WCTE; 2018.
[10] ISO16283-2:2018. Acoustics – Field measurement of sound insulation in buildings and of building elements – Part 2: Impact sound insulation.
[11] Halstedt H. Woodsol prototype element production drawings. Trondheim, NO: SINTEF Byggforsk; 2018.
[12] Bjorge V, Kristoffersen T. Konseptstudie av trebaserte kompositttdekker med mulighet for innspenning til limtresoyler [Master Thesis]: NTNU; 2017.
[13] EN1995-1-1:2004. Eurocode 5: Design of timber structures - Part 1-1: General – Common rules and rules for buildings.
[14] Dynea. Technisches. Merkblatt für. Prefere 4094 2004.
[15] Brandt A. Notes On Using the ABRAVIBE Toolbox for Experimental Modal Analysis. In: http://www.abravibe.com, editor.
[16] Brandt A. Noise and vibration analysis: signal analysis and experimental procedures. John Wiley & Sons; 2011.
[17] Cremer L, Heckl M, Petersson BA. Structure-borne sound: structural vibrations and sound radiation at audio frequencies. Springer; 2005.
[18] Maidanik G. Response of Ribbed Panels to Reverberant Acoustic Fields. J Acoust Soc Am 1962;34(6):809–26.
[19] Conta S, Homb A. Challenges and limitations using the Integral Transform Method to obtain the impact noise level of timber floors. In: Association EA, editor. Euronoise 2018; Creta2018.
[20] Kohrmann M. Numerical Methods for the Vibro-Acoustic Assessment of Timber Floor Constructions [Dissertation]: Technische. Universität München; 2017.
[21] Schoenwald S, Vallely S, Tröbs H-M. Advanced methods to determine sound power radiated from planar structures. J Acoust Soc Am 2017;141(5):3713.
[22] Winter C. Messtechnische Untersuchung leichter Deckentragwerke im Wellenzahlbereich und Prognose der abgestrahlten Schallleistung [Master]. Technische Universität München; 2012.
[23] Hashimoto N. Measurement of sound radiation efficiency by the discrete calculation method. Appl Acoust 2001;62(4):429–46.
[24] Conta S. Experimental modal analysis on Woodsol prototype floor element. NTNU/SDU 2017.
[25] Winter C, Müller G. Frequency Dependent Modeling for the Prediction of the Sound Transmission in Timber Constructions; 2018.
[26] Mindlin RD. Influence of rotatory inertia and shear on flexural motions of isotropic, elastic plates. J appl Mech 1951;18:31–8.
[27] Cremer L, Heckl M. Körperschall: physikalische Grundlagen und technische. Anwendungen: Springer-Verlag; 1996.
[28] Santoni A, Schoenwald S, Van Damme B, Fausti P. Determination of the elastic and stiffness characteristics of cross-laminated timber plates from flexural wave velocity measurements. J Sound Vib 2017;400:387–401.
[29] Vigran TE. Building acoustics. CRC Press; 2014.
[30] Roozen NB, Labelle L, Rychtáriková M, Glorieux C. Determining radiated sound power of building structures by means of laser Doppler vibrometry. J Sound Vib 2015;346:81–99.
[31] Ljunggren F, Simmons C, Öqvist R. Correlation between sound insulation and occupants' perception – Proposal of alternative single number rating of impact sound, part II. Appl Acoust 2017;123:143–51.
[32] Malo KA, Stamatopoulos H. Connections with threaded rods in moment resisting frames. Proceedings of the World Conference on Timber Engineering (WCTE 2016) 2016.

Paper #5

Original Research

BUILDING ACOUSTICS

Building Acoustics
1–23

DOI: 10.1177/1351010X20966157
journals.sagepub.com/home/bua
SAGE

Sound insulation of timber hollow box floors: Collection of laboratory measurement data and trend analysis

Anders Homb[1,2], Simone Conta[2], Christoph Geyer[3] and Niko Kumer[4]

Abstract

The industrialisation of timber buildings has improved strongly in recent years. When long span is required, timber hollow-box floor elements are increasingly used due to their structural performance. The aim of this paper is to assess the acoustic performance of timber hollow-box floors, determine the governing parameters and identify the corresponding trends. We collected results from laboratory measurements covering both airborne and impact sound insulation from four different laboratories covering a wide range of application. Data include the bare floor constructions and their combination with different floating floors including both lightweight solutions and hybrid solution. We performed the analysis focusing on following parameters: element stiffness, element mass per unit area, dynamic stiffness of the resilient layer, cavity filling and floating floor material. We present the collected data both frequency-dependent and as single number quantities. General trends and features are identified in the frequency-dependent diagrams. A further detailed analysis is based on the single number quantities. It includes a general relationship between element mass per unit area and given requirements for $R'_W + C_{50\text{-}5000}$ and $L'_{n,w} + C_{I,50\text{-}2500}$. Furthermore, diagrams are presented illustrating the dependence of impact sound insulation numbers on the cavity filling, the dynamic stiffness of the resilient layer and the type of material used for the floating floor. The additional mass in the cavity improves both airborne and impact sound insulation by minimum 10 dB. This, combined with a floating floor, allows the fulfilment of a wide range of requirements.

Keywords

Lightweight, timber floor, building acoustics, impact sound insulation, airborne sound insulation, additional mass

[1]SINTEF Building & Infrastructure, Trondheim, Norway
[2]NTNU, Department of Civil and Environmental Engineering, Trondheim, Norway
[3]Berner Fachhochschule, Biel, Switzerland
[4]Stora Enso, Wood Products, Bad ST. Leonhard, Austria

Corresponding author:
Anders Homb, SINTEF Building & Infrastructure, Høgskoleringen 7B, Trondheim, NO-7465, Norway.
Emails: anders.homb@sintef.no; Anders.homb@ntnu.no

Introduction

Woodsol project

Wood-based structural systems for modern urban buildings are currently not very competetive in the Nordic countries. Even though some landmark buildings have recently been built using timber structures, such as 'Treet' in Bergen or 'Mjøstårnet' in Brumunddal, wood is normally not considered for urban buildings of five to ten stories. Most of the today's buildings with load bearing timber structures are commissioned by owners who, for various reasons, specify the use of wood.

The state of industrialisation in this field has improved in recent years, especially in Sweden and German-speaking countries. However, although several wooden components are produced effectively by various national vendors, no industrialised system for production and assembly of five to ten story buildings are available in Norway. Consequently, building contractors and planners prefer to use other materials (concrete and steel) which they believe represent less risk than timber structure. As a response to this situation, the project Woodsol was funded by the Norwegian Research Council to develop a concept for wooden buildings in urban areas with the following main features: five to ten storeys, industrialised production and open plan configuration. The concept is based on moment-resisting timber frames and long span floor elements. The floor elements are of type hollow-box.[1] The project includes research in two main areas: Structural systems & components and Structural safety & comfort properties. Within comfort properties, the sound insulation of floors, walls and flanking transmission is essential.

The motivation for this paper emerged as we prepared a preliminary study and data collection[2] for the WOODSOL project and detailed a first application scenario for an office building.[3]

Objective

The concept of timber hollow box floors is not new. Originally the cross-section was made of pure wood. Later development includes the use of different engineered wood products (e.g. glulam and laminated veneer lumber). In the Woodsol project this concept is further developed to increase the possible span width. An important advantage of hollow box floors is more efficient material use compared to traditional solid floors (e.g. cross laminated timber slabs). Then it is possible to achieve increased stiffness and load bearing capacity due to stiff structural connections within the cross-section. Moreover, the space inside the box may be used to improve the fire resistance and sound insulation when necessary, without increasing the total height of the element.

This paper focuses on the sound insulation properties of timber hollow box floor element, that is, on the vertical sound transmission through the elements. We aim to establish the current state of the art and build a better understanding by collecting measurement data on internationally level and comparing data from similar floor constructions. Regarding the timber hollow box concept, a number of articles is available, for example,[4] but only a few conference papers focusing on sound insulation, have been found.[5,6] In addition, several manufacturers' presentations of such products give relevant information which is partly available at public platforms.[7]

This paper presents results from sound insulation measurements performed in laboratory. Impact sound insulation tends to be the most significant problem for the wooden floor construction building technique. Nevertheless, both airborne sound insulation and impact sound insulation results are presented. The main objective is to identify features and trends of the sound insulation properties within the available dataset in order to understand how the differences among the constructions affect their sound insulation properties. The collected data are valuable for the assessment of other constructions and input for better prediction tools. For further use, data can also be compared with similar data from wooden joist constructions[8] and cross-laminated timber floor constructions.[9]

The paper is structured as followed: in 'Floor assemblies', we describe the constructions considered in this paper. 'Bare floor constructions', 'Lightweight top floor constructions' and 'Hybrid top floor constructions' present the analysis of the frequency dependent data for the bare floors, solutions with lightweight floating floor and hybrid constructions, respectively. In 'Analysis of the single number ratings', we present a detailed analysis of the single number ratings, starting from an overall evaluation ('Overall trend related to the mass per unit area') and then focusing on the impact sound insulation ('Mass per unit area trend'). Finally, in 'Conclusion', we present the conclusions.

Measurement method and data

The airborne and the impact sound insulation measurements were carried out according to ISO 10140-2[10] and ISO 10140-3[11] respectively, versions valid at the time of measurements. Most of the measurements have been carried out in the frequency range from 50 Hz. The measured airborne sound insulation and normalised impact sound pressure levels in the frequency range 50 to 5000 Hz are presented as graphs in the following sections. From the test result, we calculated the single-number quantities for rating the airborne sound insulation, R_w and $C_{50\text{-}5000}$ and the sum of these according to EN-ISO 717-1.[12] We determined the weighted normalized impact sound pressure level $L_{n,w}$, the spectrum adaptation term $C_{I,50\text{-}2500}$ and the sum of these, $L_{n,w} + C_{I,50\text{-}2500}$ according to EN-ISO 717-2.[13]

Measurements results were collected from the activities related to the WOODSOL project, Silent Timber Build project including data from Lignum, from laboratory measurements at EMPA on closed LVL rib panels by Stora Enso and from laboratory measurements at Bern University on a swiss product. References will be given later in the paper. In total, approximately 70 laboratory measurement data regarding airborne sound insulation and approximately 110 laboratory measurement data regarding impact sound insulation have been collected and evaluated. However, for each main type of construction, a limited number of records will be reported. The idea was to extract results only from constructions relevant to the Woodsol project and focus on the vertical sound transmission of such floors. In 'Bare floor constructions', 'Lightweight top floor constructions' and 'Hybrid top floor constructions', airborne and impact sound insulation data from the different constructions are presented. For all presented data, the total mass per unit area (mpua) in kg/m² of the floor construction is given.

The analysis of the collected results allowed us to identify the parameters that has the most influence on the floor performance in terms of airborne sound insulation and impact sound level.

Sound insulation requirements

For ease of reference, we recall in Table 1 the existing sound insulation requirements and the recently suggested new requirements in Norway[14] and other countries with similar requirements and constructions. The building regulations in many countries were developed when lightweight structures were rarely used or not even permitted for multi-storey residential buildings. Thereby, requirements are based on heavy weight structural behaviour, that is, current single number ratings presuppose structures which have very good low frequency sound insulation properties. To fully compete with heavy floor structures, timber-based constructions need to give similar properties throughout a broad frequency range. The discussion is about using the ISO spectrum adaptation terms from 50 Hz or even from 20 Hz.[15] Therefore, there is an ongoing process in several European countries about the establishment of new requirements or recommendations, at least for residential buildings.

Table 1. Sound insulation requirements, residential buildings.

Country	Legal requirement		Reference
	Airborne sound insulation	Impact sound insulation	
Austria	$D_{nT,w} \geq 55$ dB	$L'_{nT},w \leq 48$ dB	ÖNORM B 8115-2
Norway	$R'_w \geq 55$ dB[a]	$L'_{n,w} \leq 53$ dB[b]	NS8175:2019
Sweden	$D'_{nT,w,50} \geq 52$ dB	$L'_{n,Tw} \leq 56$ dB and $L'_{n,Tw} + C_{I,50-2500} \leq 56$ dB	SS25267:2015
Switzerland	$D_{nT,w} + C \geq 52$ dB	$L'_{nT,w} + C_i \leq 53$ dB	SIA181:2006
Germany	R'_w (Wall/Floor) $\geq 53/\geq 54$ dB	$L'_{n,w} \leq 50/\leq 53$ dB[c]	DIN 4109-1:2018

[a]Suggested requirement in NS 8175:2019: $R'_w + C_{50-5000} \geq 54$ dB.
[b]Suggested requirement in NS 8175:2019: $L'_{n,w} + C_{I,50-2500} \leq 54$ dB.
[c]Weaker requirement valid for lightweight constructions.

Floor assemblies

Construction types

Floor assemblies presented in this paper are the following main types:

I) Bare floor timber hollow-box constructions
II) Lightweight top floor constructions
III) Hybrid top floor constructions

The cross-section of the hollow box itself varied among the different tested products and is further detailed in Table 2. The bare floor cavity can be either empty, filled with sound absorbing material (e.g. mineral wool, wood fibre), or with mass (e.g. gravel). Additional mass can be installed alternatively on top of the bare floor (e.g. gravel, concrete layer or wet screed). Floating floors on top of the bare floor can be either lightweight (e.g. dry screed on mineral wool) or heavy (e.g. concrete or wet screed). The details of the different floor variants and the floating floor options considered in this paper are presented in chapter 3.1 to 5.4.

Bare floor constructions

With bare floor, we denote in the following the main timber hollow-box structure, without additional layer on the top side or ceiling construction on the bottom side. Available data include measurements on bare floors with or without cavity filling. The filling can consist of two types: either a porous absorber to dampen the cavity resonances or gravel / sand, in order to increase the mass per unit area of the floors. As introduced in the previous section, the additional mass can also be installed on top of the hollow-box, either as loose gravel or as a composite concrete or wet screed layer.

Among the collected constructions, the cross-sections have different dimension and material specification as given in Table 2. The respective effective bending stiffness and span length of the floor elements varies accordingly. Schematic drawings of such floors are given in Figure 1(a) to (c).

Table 2. Key data, bare floors.

Element	Woodsol	Lignum	Stora Enso	Swiss Bern
Abbreviation	WS 1-8	LI 1-20	SE 1-3	Bern 1-3
Total thickness	509 mm	200–240 mm	300 mm	294 mm
Beam dimension	Edge beams 75 × 405 mm Center beams 48 × 405 mm c/c 580 mm	Height 138–178 mm c/c 200–243 mm	SE LVL rib 51 × 240 mm c/c 560 mm	80 × 240 mm c/c 625 mm
Top plate	Kerto Q 43 mm	Wood 28–31 mm	SE LVL 35 mm	Wood composite plate 27 mm
Bottom plate	Kerto Q 61 mm	Wood 28–31 mm	SE LVL 25 mm	Wood composite plate 27 mm

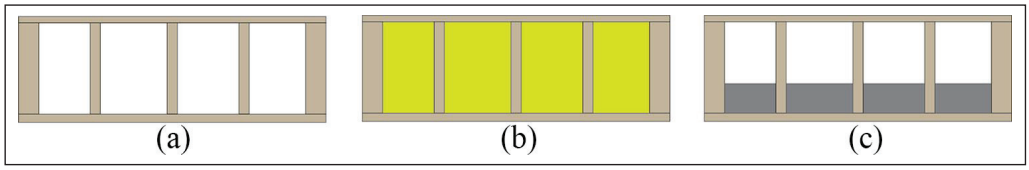

Figure 1. Bare floor cross section of the elements in this paper. (a) Empty wood box. (b) Wood box with porous absorber. (c) Wood box with gravel.

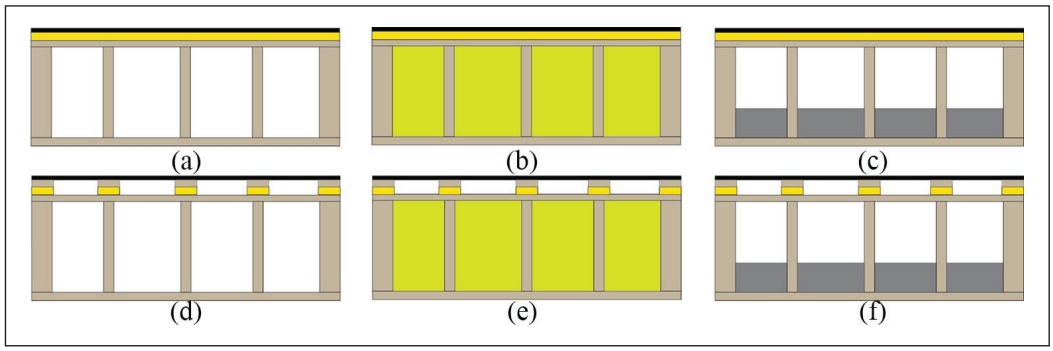

Figure 2. Lightweight top floor constructions. (a) Empty bare floor with dry screed on continuous resilient layer. (b) Bare floor with porous absorber and dry screed on continuous resilient layer. (c) Gravel filled bare floor with dry screed on continuous resilient layer. (d) Empty bare floor with dry screed on point elastic supports. (e) Bare floor with porous absorber with dry screed on point elastic supports. (f) Gravel filled bare floor with dry screed on point elastic supports.

Lightweight top floor constructions

Lightweight timber hollow-box constructions consist of the main timber hollow-box structure as a base floor, with a lightweight floating floor on top. Available data consist of measurements on different objects with a floating floor with the resilient material either over the entire surface or as point elastic support. These can be combined with the different constructions for the bare floor outlined above. Schematic sketches of selected combinations are given in Figure 2(a) to (f).

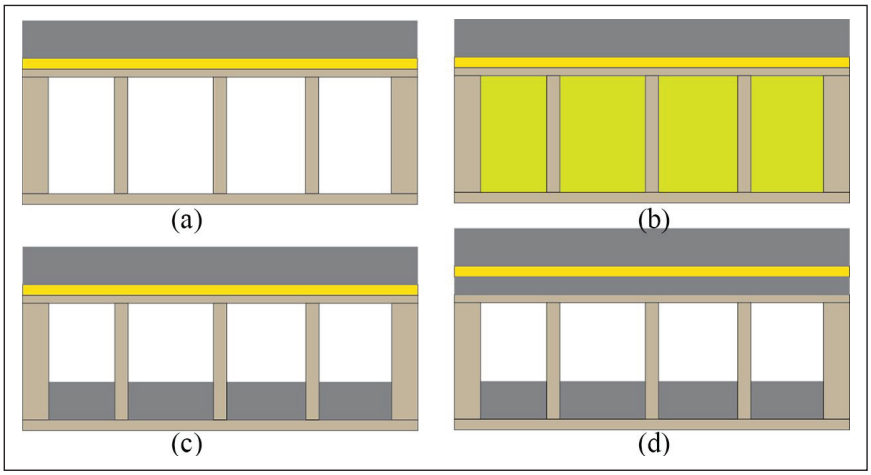

Figure 3. Hybrid top floor constructions. (a) Empty bare floor with concrete or wet screed on continuous resilient layer. (b) Bare floor with porous absorber and concrete or wet screed on continuous resilient layer. (c) Gravel filled bare floor with concrete or wet screed on continuous resilient layer. (d) Gravel filled bare floor with concrete or wet screed on continuous resilient layer with additional gravel layer directly above the hollow box.

Hybrid top floor constructions

Hybrid top floor constructions consist of the main timber hollow-box structure with an additional floating floor including a layer of concrete or wet screed. Schematic diagrams of selected combinations are given in Figure 3(a) to (c).

Bare floor constructions

Bare floor with various cavity fill

Laboratory measurement result of airborne and impact sound insulation of the bare floor are presented in Figure 4(a) and (b). The cross-section dimensions of the considered elements are rather different, see Table 2, and so is the mass per unit area (mpua) of the elements. The comparison includes constructions with gravel, mineral wool or porous wood fibres filling, see bare floor cross sections in Figure 1. An overview of the objects included in the comparison, is given in Table 3 along with the single number ratings. The mass per unit area given in the table, comprises both the mass of the bare floor and the mass of additional fillings. The mass of the additional filling is also given separate in the 'cavity fill' column along with a description of the filling.

The airborne sound insulation results reveal a large spread in the whole frequency range of interest. This is due to the different cross sections of the elements and the varying filling. The heaviest element (Bern) delivers the highest overall airborne sound insulation. The lowest performance is delivered by the lighter elements, especially when the cavity is empty (WS-1).

The effect of the additional mass in the cavity can be clearly observed between 100 Hz and 2000 Hz; in this frequency range, the elements with gravel show R_w values up to 20 dB higher compared to those without gravel. The stiffness of the element strongly influences the airborne sound insulation at low frequencies; the high stiffness of Woodsol elements give high airborne sound insulation at low frequencies, even when the gravel is removed. See SINTEF[17] for more

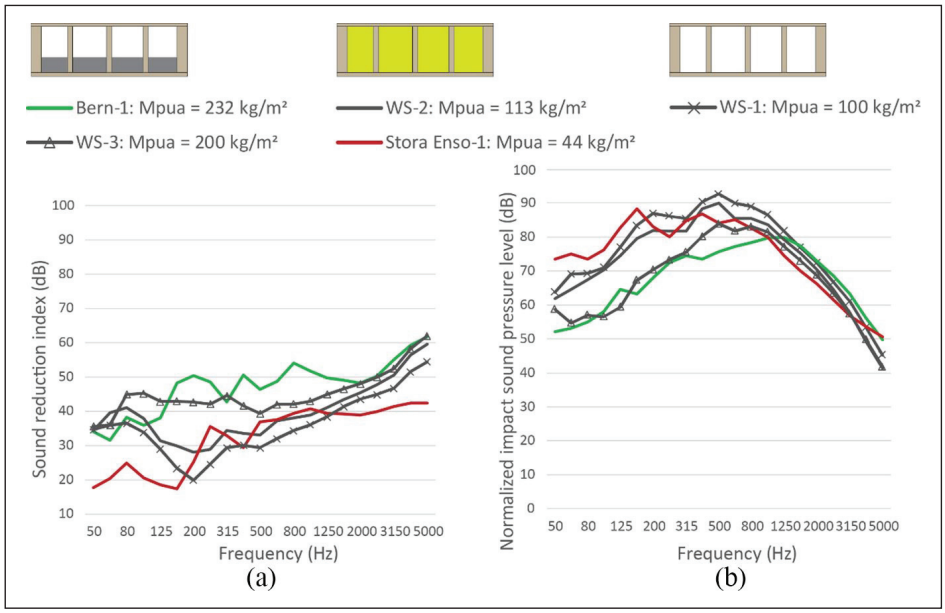

Figure 4. Laboratory measurements of bare timber hollow-box floors, refs.[5,16,17] (a) Left: Airborne sound insulation. (b) Right: Impact sound insulation.

Table 3. Key data, bare timber hollow-box floors.

Object	Mass per unit area (kg/m^2)	Cavity fill (kg/m^2)	R_w (dB)	$R_w + C_{50–5000}$ (dB)	$L_{n,w}$ (dB)	$L_{n,w} + C_{I,50–2500}$ (dB)	Source
SE-1	44	Min.wool, 3	37	36	80	80	Kumer[16]
WS-1	100	–	35	35	85	83	SINTEF[17]
WS-2	113	Wood fibre, 13	39	39	83	80	SINTEF[17]
WS-3	200	Gravel, 100	45	45	79	75	SINTEF[17]
Bern-1	232	Gravel, 195	50	50	80	80	Melián Hernández et al.[5]

details concerning the stiffness properties of this elements and their modal behaviour. For elements with relatively low cross-section stiffness, that is, construction from Bern, the effect of the gravel is significant also at low frequencies.

The result for the impact sound insulation scatter considerably in the frequency below approximately 1250 Hz. Above this frequency, the timber surface hardness of the top plate has the major influence on the impact sound level and the spreading of the results reduces to approximately 5 dB. Below 1250 Hz, the effect of the gravel in the cavity is dominant; $L_{n,w}$ is up to 15 dB lower for the elements with gravel compared to the elements without gravel. Below 400 Hz, the Bern element and the WS-3 element show a very similar behaviour, suggesting that the gravel play a major role in this frequency range. The frequency of maximum impact sound level varies significantly among the different constructions, probably due to sound radiation and critical frequencies of the wooden plate and structural connections. Regarding the airborne sound insulation, the stiffer and heavier elements deliver the best performance also in terms of impact sound insulation.

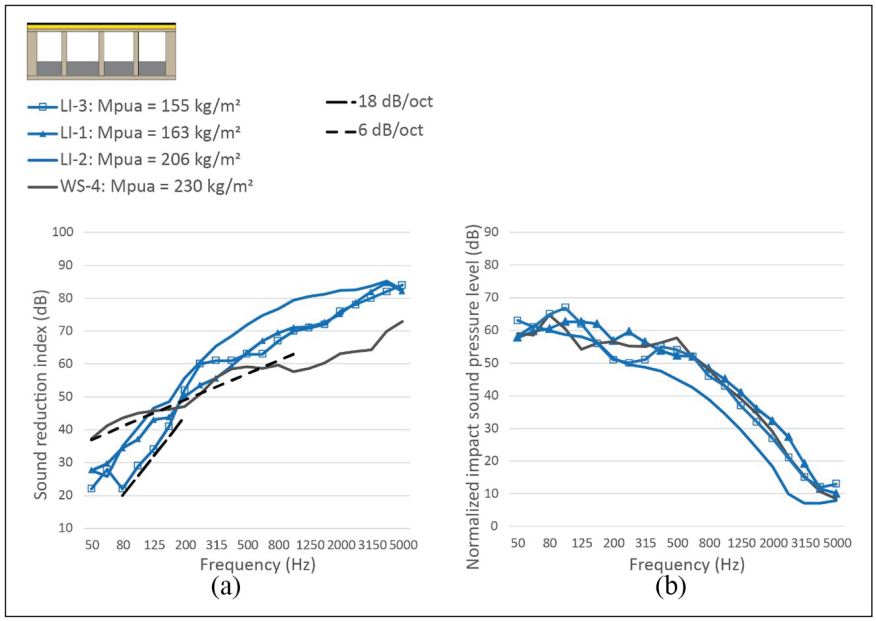

Figure 5. Laboratory measurements of timber hollow-box floors including continuous elastic layer of mineral wool, refs.[7,17] (a) Left: Airborne sound insulation. (b) Right: Impact sound insulation.

Table 4. Key data, timber hollow-box floors with continuously elastic layer of mineral wool.

Object	Mass per unit area (kg/m^2)	Cavity fill (kg/m^2)	R_w (dB)	$R_w + C_{50-5000}$ (dB)	$L_{n,w}$ (dB)	$L_{n,w} + C_{I,50-2500}$ (dB)	Source
LI-3	155	Gravel, 90	61	52	52	57	Lignum[7]
LI-1	163	Gravel, 75	63	59	53	55	Lignum[7]
LI-2	206	Gravel, 75	69	60	47	52	Lignum[7]
WS-4	230	Gravel, 100	60	59	52	54	SINTEF[17]

Lightweight top floor constructions

Continuous elastic layer of mineral wool

The results from the laboratory measurement of the airborne and the impact sound insulation of timber hollow-box floors with lightweight top floor constructions and continuous elastic layer (Figure 2(c)) is presented in Figure 5(a) and (b). Presented results deal with constructions involving continuous elastic layer of mineral wool with dynamic stiffness s' $\leqslant$ 15 MN/m^3 (DS is used in some figures instead of s'). All the objects featured a bare floor with gravel filling. Presented data is an extract of available data with key information given in Table 4.

The results deviate considerably in the whole frequency range among the collected objects. The high cross-section stiffness of WS-4 enhances the sound insulation at low frequencies but limits the sound insulation at higher frequencies. The double-wall resonance is clearly seen for object LI-2 and LI-3 (at 63 and 80 Hz). The slope of approximately 18 dB/octave from these frequencies indicates a very low structural connection below the shift frequency.[18] The slope of 6 dB/octave for the WS-4 object indicates an acoustic behaviour similar to the mass law of a single plate. Regarding

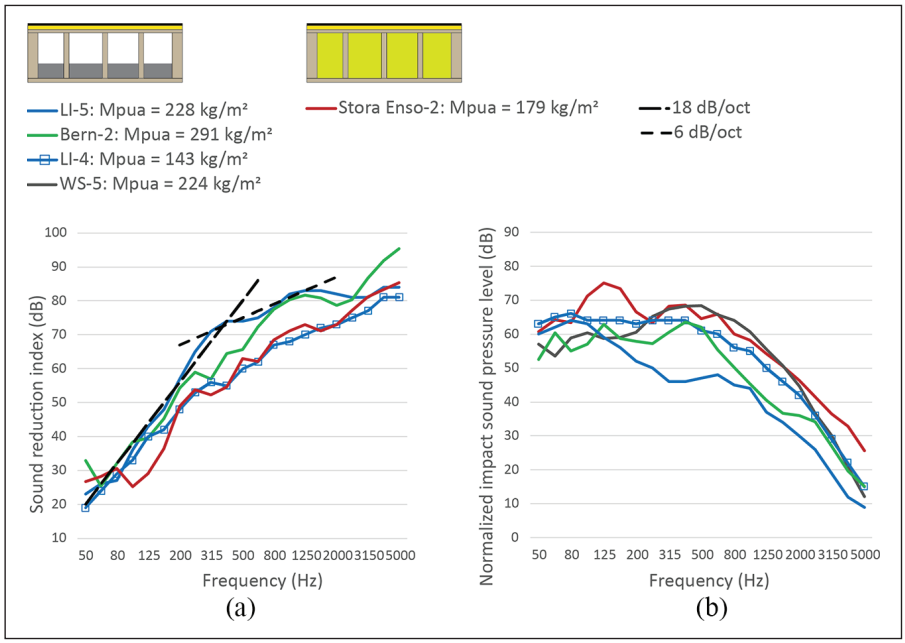

Figure 6. Laboratory measurements of timber hollow-box floors including continuous elastic layer of porous wood fibre, refs.[5,7,16,17] (a) Left: Airborne sound insulation. (b) Right: Impact sound insulation.

single number quantities, the maximum difference between the objects are 8 dB for $R_w + C_{50\text{-}5000}$ and 5 dB for $L_{n,w} + C_{I,50\text{-}2500}$. Object LI-2 have 33% higher mass per unit area compare to LI-3. However, they both show the same high spectrum adaptation terms, both considering airborne and impact sound insulation, due to the resonance frequency of the elastic top floor construction.

Continuous elastic layer of porous wood fibre

The results from the laboratory measurement of the airborne and impact sound insulation of timber hollow-box floors with lightweight top floor constructions and continuous elastic layer (Figure 2(c)) is presented in Figure 6(a) and (b). Figure 6 cover constructions with continuous elastic layer of porous wood fibre with dynamic stiffness s' $\geqslant$ 15 MN/m^3, and is an extract of available data. Key data are given in Table 5.

Airborne sound insulation deviates strongly in the frequency range, especially above 200 Hz, and there is a significant effect on the mass per unit area. The double-wall resonance is clearly seen especially for object LI-4. The slope of 14 to 18 dB/octave above the double wall resonance indicates a limited structural connection below the shift frequency. In the frequency range above the shift frequency, f_d = 55/cavity depth (Hz),[16] the general trend is an increase of the airborne sound insulation of 6 dB/octave.

The results from the impact sound insulation also deviate considerably in most part of the frequency range. Loading with gravel inside the wood box has a significant influence on the impact sound insulation, and in general, the results show a correlation between mass per unit area and the single number quantity $L_{n,w} + C_{I,50\text{-}2500}$. Measurement from object LI-5 deviates considerably at medium and high frequencies, and object from[13] without gravel at lower frequencies. For other constructions loaded with gravel, the limiting frequency range is between 250 and 1250 Hz.

Table 5. Key data, timber hollow-box floors with continuously elastic layer of porous wood fibres.

Object	Mass per unit area (kg/m^2)	Cavity fill (kg/m^2)	R_w (dB)	$R_w + C_{50–5000}$ (dB)	$L_{n,w}$ (dB)	$L_{n,w} + C_{I,50–2500}$ (dB)[a]	Source
LI-4	143	Gravel, 45	61	54	59	60	Lignum[7]
SE-2	179	Min.wool, 3	56	51	64	65	Kumer[16]
WS-5	224	Gravel, 100	–	–	62	62	SINTEF[17]
LI-5	228	Gravel, 90	68	57	49	55	Lignum[7]
Bern-2	291	Gravel, 195	65	58	55	56	Melián Hernández et al.[5]

[a]Negative values of $C_{I,50–2500}$ neglected in the sum according to NS 8175.

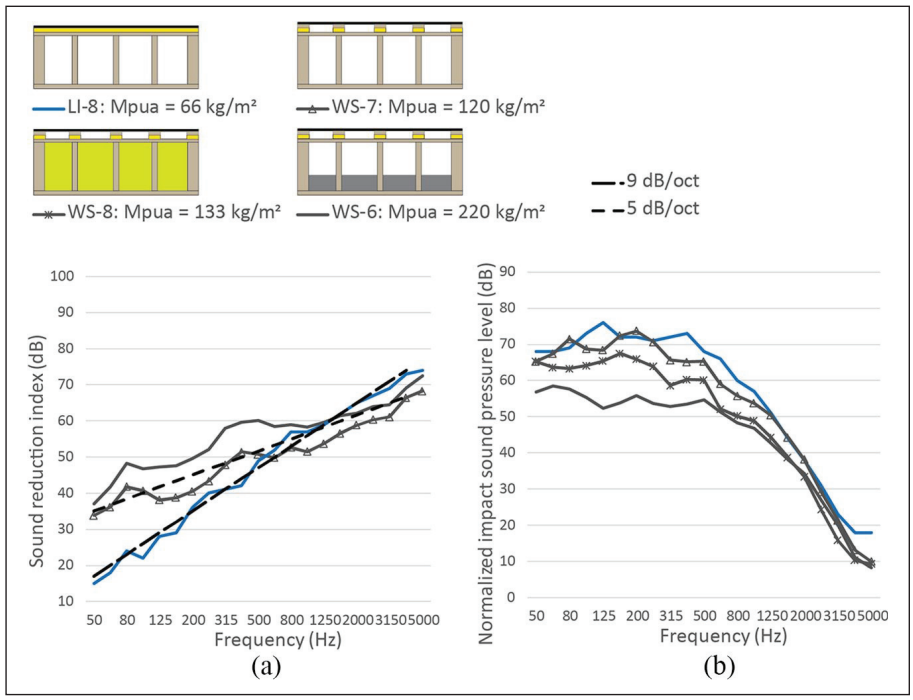

Figure 7. Laboratory measurements of various constructions of timber hollow-box floors, refs.[7,17] (a) Left: Airborne sound insulation. (b) Right: Impact sound insulation.

Lightweight top floor on resilient point supports or floor without gravel

The results from the laboratory measurement of airborne and impact sound insulation of timber hollow-box floors with lightweight top floor on resilient point supports with or without gravel are presented in Figure 7(a) and (b). The results cover constructions with 25 mm Sylodyn elements and centre distances 560 and 600 mm, respectively. Key data for all objects are given in Table 6.

Airborne sound insulation results deviate strongly in the whole frequency range, especially below 1250 Hz and there is a significant effect on the mass per unit area. The object LI-8 shows a general trend with an increase of the airborne sound insulation of 9 dB/octave. For the WS objects, the general trend is an increase of the airborne sound insulation of approximately 6 dB/octave.

Table 6. Key data, various constructions of timber hollow-box floors.

Object	Mass per unit area (kg/m^2)	Cavity fill (kg/m^2)	R_w (dB)	$R_w + C_{50–5000}$ (dB)	$L_{n,w}$ (dB)	$L_{n,w} + C_{I,50–2500}$ (dB)	Source
LI-8	66	0	48	45	67	67	Lignum[7]
WS-7	120	0	53	53	64	65	SINTEF[17]
WS-8	133	13	–	–	58	60	SINTEF[17]
WS-6	220	100	61	60	50	51	SINTEF[17]

The results from the impact sound insulation also deviate considerably except from frequencies above 2000 Hz. Similar to the airborne sound insulation, loading with gravel has a significant influence on the impact sound level. The results show a high correlation between mass per unit area and the single number quantity $L_{n,w} + C_{I,50\text{-}2500}$, but the high cross-section stiffness of the WS-objects play an important role at low frequencies as well (Conta and Homb)[19]. The measurement results of object LI-8 and WS-7 without cavity fill are remarkably comparable even if the construction is quite different.

Hybrid top floor constructions

Objects without additional mass in the cavity

Laboratory measurement result of airborne and impact sound insulation of hybrid timber hollow-box floors without gravel are presented in Figure 8(a) and (b). Key data for all objects are given in Table 7.

Airborne sound insulation deviates strongly in most of the frequency range, and the effect of the mass per unit area is not clearly seen. The objects show a general trend with an increase of the airborne sound insulation of 8 to 10 dB/octave, indicating a larger effect than the mass law for single structures.

Impact sound insulation results show in general comparable trends, but the effect of the mass per unit area is not clearly seen; the lightest and heaviest element show comparable performance. Above 400 Hz, L_n from LI-10 is clearly above the other two objects. This is observed both in the single number ratings and in the frequency dependent properties.

Objects with wet screed, gravel and continuous elastic layer of mineral wool

Laboratory measurement result of the airborne and impact sound insulation of hybrid timber hollow-box floors with wet screed, normally fibre reinforced (typically density 1900 kg/m^3) on continuous elastic layer are presented in Figure 9(a) and (b). The results cover constructions with continuous elastic layer of mineral wool with dynamic stiffness lower than 8 MN/m^3 and gravel in the cavity or gravel directly above the wooden layer (LI-14). Presented results are an extract of available data showing objects with medium performance regarding the mass per unit area. Key information of these objects is given in Table 8.

Except object LI-11, the airborne sound insulation coincides relatively well in the whole frequency range, but the effect of the mass per unit area is not significant. All objects show a slope of approximately 24 db/octave up to a visible shift frequency at 125 Hz. This is significantly higher than the theoretical expected slope of a double wall construction but stops at a frequency far below the theoretical shift frequency based on $f_d = 55/\text{cavity depth (Hz)}$. At higher frequencies, the slope is closer to 5 dB/octave which is far below the expected slope if we compare to an uncoupled double wall.

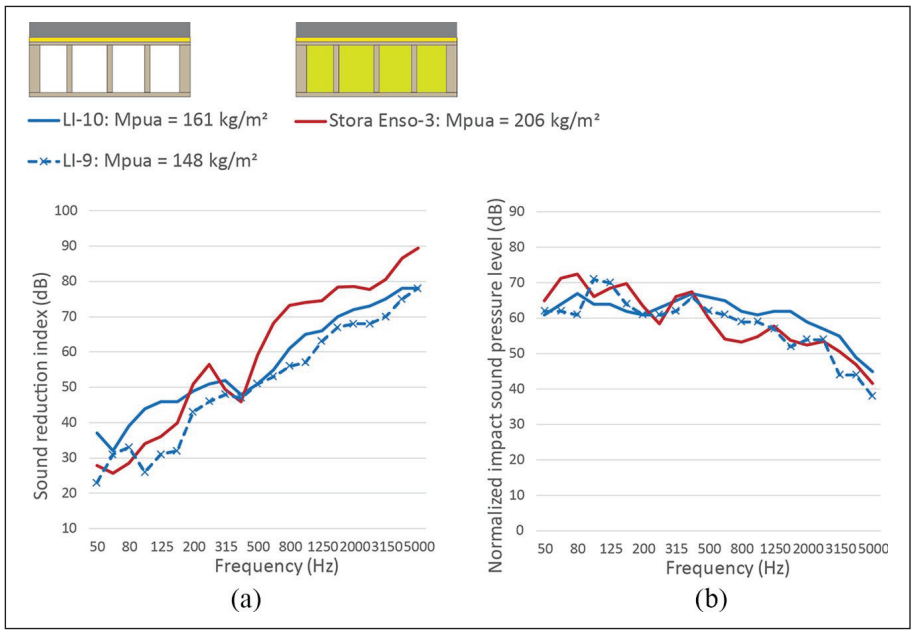

Figure 8. Laboratory measurements of various constructions of timber hollow-box floors, refs.[7,16] (a) Left: Airborne sound insulation. (b) Right: Impact sound insulation.

Table 7. Key data, hybrid timber hollow-box floors without additional mass in the cavity.

Object	Mass per unit area (kg/m^2)	Cavity fill (kg/m^2)	R_w (dB)	$R_w + C_{50–5000}$ (dB)	$L_{n,w}$ (dB)	$L_{n,w} + C_{I,50–2500}$ (dB)[a]	Source
LI-9[b]	148	–	53	50	62	62	Lignum[7]
LI-10[c]	161	–	59	58	66	66	Lignum[7]
SE-3[d]	206	Min.wool, 3	58	55	63	63	Kumer[16]

[a]Negative values of $C_{I,50–2500}$ neglected in the sum according to NS 8175.
[b]Continuously elastic layer, mineral wool s' = 20 MN/m^3.
[c]Continuously elastic layer, mineral wool s' = 6 MN/m^3.
[d]Continuously elastic layer, cell foam.

Impact sound insulation results deviate considerably in major part of the frequency range, but the results show a relatively high correlation between mass per unit area and the single number quantity $L_{n,w} + C_{I,50-2500}$. For objects LI-11 to LI-13, the $L_{n,w}$-value is determined by the high frequency behaviour. The levels are higher compared to the constructions presented in the previous section because of the higher surface hardness of the wet screed compared to floor coverings or a timber surface of the other constructions.

Objects with concrete, gravel and continuous elastic layer of mineral wool

Laboratory measurement result of the airborne and impact sound insulation of hybrid timber hollow-box floors with concrete (typical density 2300 kg/m^3) on continuous elastic layer are presented in Figure 10(a) and (b). The results cover constructions with continuous elastic layer of mineral

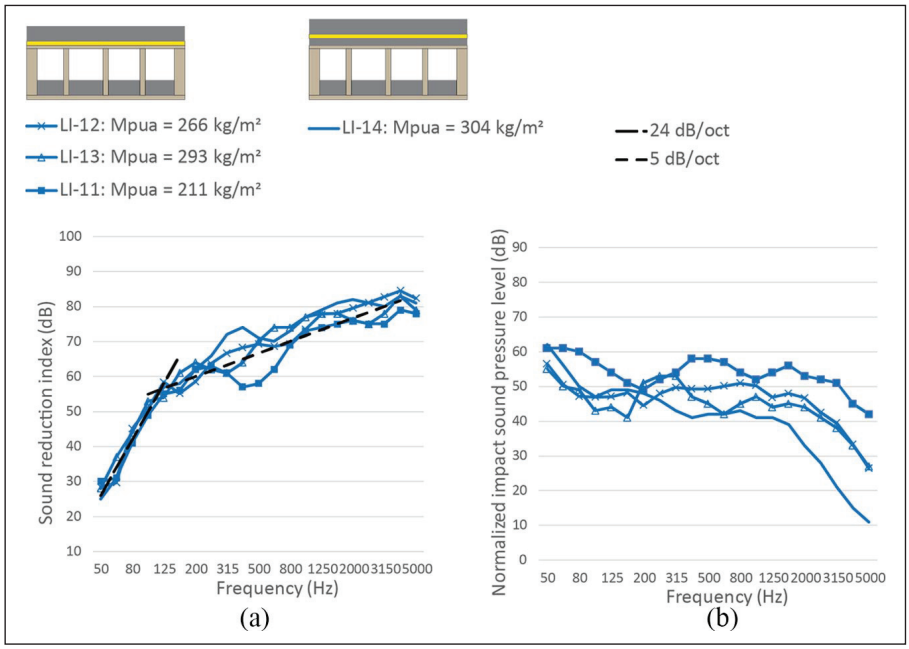

Figure 9. Laboratory measurements of hybrid timber hollow-box floors with wet screed on continuous elastic layer, Lignum.[7] (a) Left: Airborne sound insulation. (b) Right: Impact sound insulation.

Table 8. Key data, hybrid timber hollow-box floors with wet screed on continuous elastic layer.

Object	Mass per unit area (kg/m^2)	Cavity fill (kg/m^2)	R_w (dB)	$R_w + C_{50–5000}$ (dB)	$L_{n,w}$ (dB)	$L_{n,w} + C_{I,50–2500}$ (dB)[a]	Source
LI-11	211	Gravel, 50	68	63	60	60	Lignum[7]
LI-12	266	Gravel, 75	72	64	52	52	Lignum[7]
LI-13	293	Gravel, 123	70	66	50	50	Lignum[7]
LI-14	304	Gravel, 90	70	63	43	49	Lignum[7]

[a]Negative values of $C_{I,50–2500}$ neglected in the sum according to NS 8175.

wool with dynamic stiffness lower than 8 MN/m^3 and gravel in the cavity or alternatively directly above the wood layer (object LI-16 and LI-17). The presented results are a representative extract of available data. Key information of these objects is given in Table 9.

Three of the objects (LI-15 to LI-17) show comparable results in the entire frequency range regarding the airborne sound insulation. The effect of the cavity fill seems to be more important than the total mass per unit area, especially at very low frequencies (object Bern-3). At lower frequencies, the slope varies from 14 to approximately 22 dB/octave and from medium to high frequencies between 4 and 9 dB/octave. The frequency dependent shape of these results shows, ast expected, a behaviour between uncoupled elements (visible at low frequencies, 18 dB/octave) and stiff coupled elements (visible above 200 Hz, 6 dB/octave).

All impact sound insulation results show comparable shape except at high frequencies. Gravel also on top of the timber hollow-box seems to have a significant effect of the impact sound insulation at higher frequencies. The correlation between mass per unit area and the single number quantity $L_{n,w} + C_{I,50-2500}$ is therefore weak.

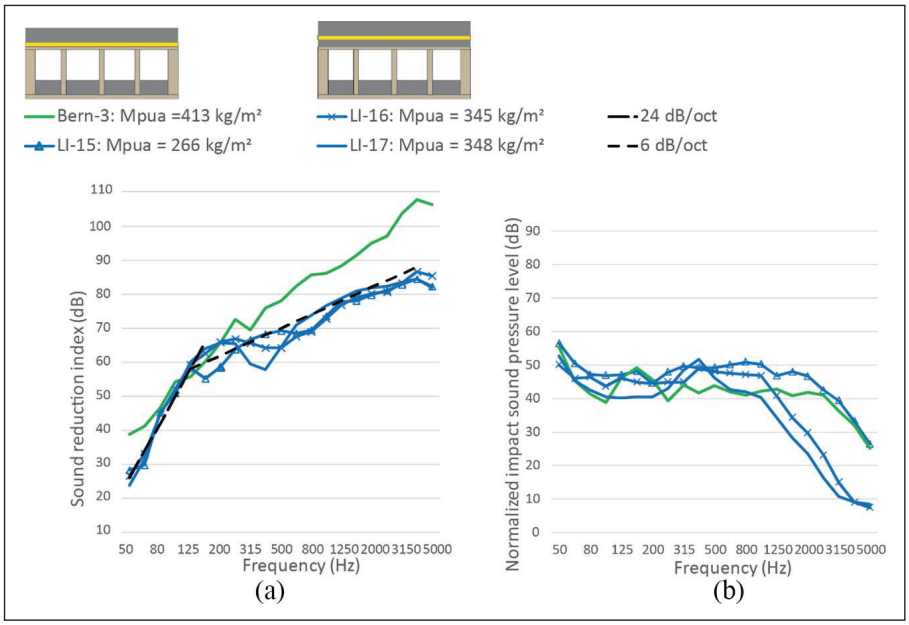

Figure 10. Laboratory measurements of hybrid timber hollow-box floors with concrete on continuous elastic layer, refs.[5,7] (a) Left: Airborne sound insulation. (b) Right: Impact sound insulation.

Table 9. Key data, hybrid timber hollow-box floors with concrete and continuous elastic layer.

Object	Mass per unit area (kg/m^2)	Cavity fill (kg/m^2)	R_w (dB)	$R_w + C_{50–5000}$ (dB)	$L_{n,w}$ (dB)	$L_{n,w} + C_{I,50–2500}$ (dB)[a]	Source
LI-15	266	97	72	64	52	52	Lignum[7]
LI-16	345	40	72	65	44	44	Lignum[7]
LI-17	348	40	71	62	41	43	Lignum[7]
Bern-3	413	195	79	73	47	47	Melián Hernández et al.[5]

[a]Negative values of $C_{I,50–2500}$ neglected in the sum according to NS 8175.

Objects with dry, heavy screed and elastic layer of porous wood fibre

Laboratory measurement result of the airborne and impact sound insulation of timber hollow-box floors with dry, heavy screed (typically gypsum fibre boards or cement-bonded boards) and continuous elastic layer are presented in Figure 11(a) and (b). Figure 11 covers constructions with continuous elastic layer of porous wood fibre with dynamic stiffness between 20 and 30 MN/m^3, and is an extract of available data. Key data are given in Table 10.

All presented results show comparable frequency shape regarding the airborne sound insulation. We observe a proportional ratio between the single number quantity, $R_w + C_{50\text{-}5000}$ and the mass per unit area. At lower frequencies, the slope varies between 14 and approximately 17 dB/octave and at medium to high frequencies only 3 to 5 dB/octave. The fundamental shape of this curves is similar to object type as presented in 'Objects with wet screed, gravel and continuous elastic layer of mineral wool' and 'Objects with concrete, gravel and continuous elastic layer of mineral wool'.

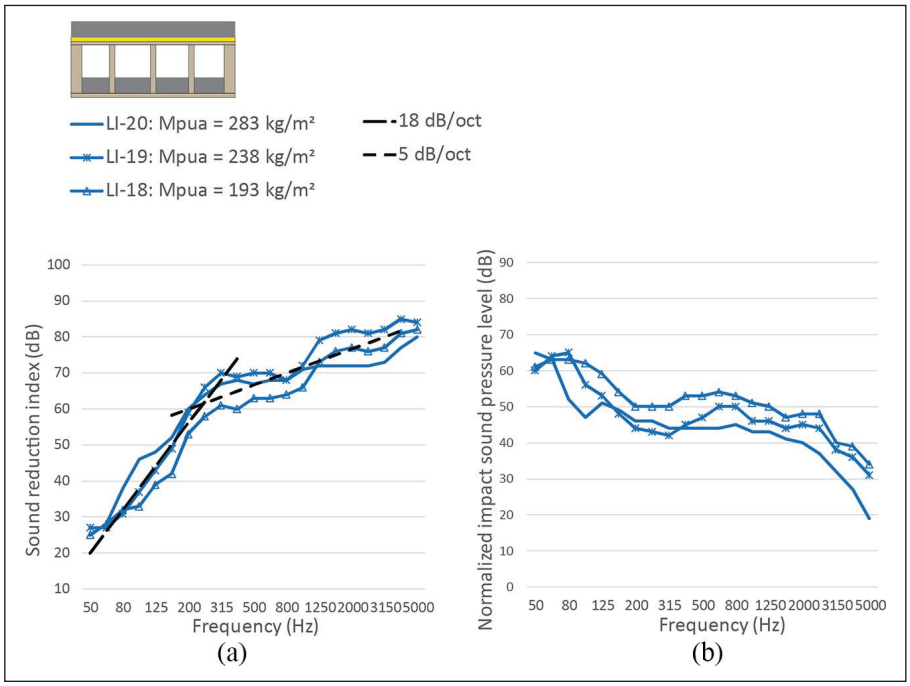

Figure 11. Laboratory measurements of hybrid timber hollow-box floors with dry, heavy screed on continuous elastic layer, Lignum.[7] (a) Left: Airborne sound insulation. (b) Right: Impact sound insulation.

Table 10. Key data, dry, heavy screed and continuous elastic layer.

Object	Mass per unit area (kg/m²)	Cavity fill (kg/m²)	R_w (dB)	$R_w + C_{50–5000}$ (dB)	$L_{n,w}$ (dB)	$L_{n,w} + C_{I,50–2500}$ (dB)	Source
LI-18	193	45	63	57	55	55	Lignum[7]
LI-19	238	90	68	59	51	54	Lignum[7]
LI-20	283	135	69	61	46	53	Lignum[7]

All impact sound insulation results show relatively similar frequency shape regarding the impact sound level with significant increasing levels towards low frequencies. Lack of soft floor covering determines the impact sound level, especially at medium frequencies. The correlation between mass per unit area and the single number quantity $L_{n,w} + C_{I,50\text{-}2500}$ seems weak.

Analysis of the single number ratings

Overall trend related to the mass per unit area

We present here an overall evaluation of the collected measurement results. The focus is now on the single number ratings $R_w + C_{50\text{-}5000}$ and $L_{n,w} + C_{I,50\text{-}2500}$ and their dependence on the mass per unit area. The collection has been grouped into the same categories as presented in the previous sections.

Figures 12 and 13 show $R_w + C_{50\text{-}5000}$ and $L_{n,w} + C_{I,50\text{-}2500}$ as a function of the mpua for objects from all considered categories. The recommended Norwegian requirement level for residential buildings is also included in the figures.

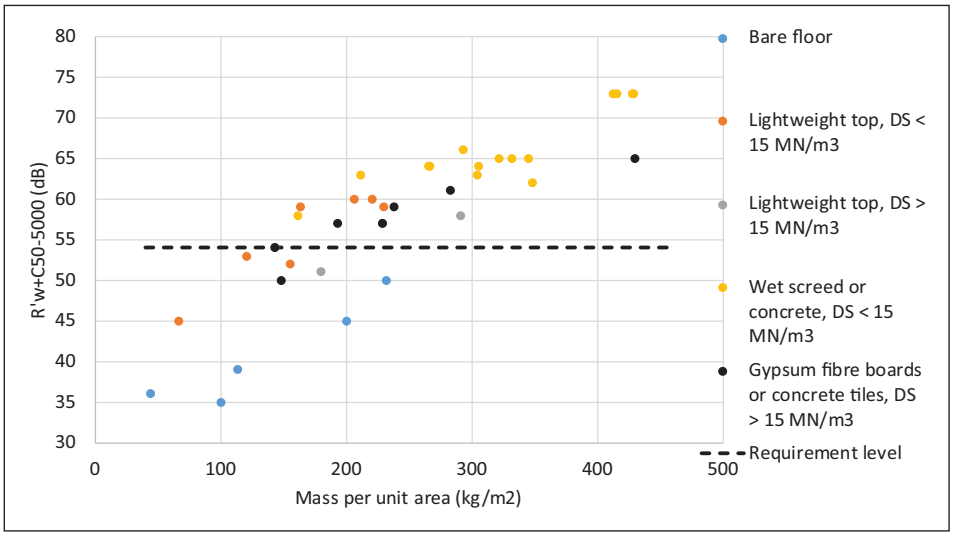

Figure 12. Single number rating, $R_w + C_{50–5000}$ as a function of mass per unit area. Objects from all considered categories.

As expected, the bare floor constructions (also constructions without any additional layer) show poor sound insulation properties, both for the airborne and impact sound insulation. Regarding airborne sound insulation, we see a clear correlation to the mass per unit area, mainly due to cavity fill with gravel. For all other constructions, that is, all top floor construction, there is a significant tendency of improved properties with increased mass per unit area. However, there is a general, very large scattering among the measurement results. The scattering is remarkably narrowed when we separate the results with respect of the dynamic stiffness properties of the resilient layer. Therefore, the data have been grouped into results with dynamic stiffness lower or higher than 15 MN/m^3. This is further analysed in chapter 6.4.

To meet the requirement level of $R'_w + C_{50\text{-}5000} \geqslant 54$ dB, the mass per unit area needs to be above approximately 200 kg/m^2. However, with optimal choice of material properties, slightly lower mass per unit area should be possible. To meet a requirement level of $L'_{n,w} + C_{I,50\text{-}2500} \leqslant 54$ dB, Figure 14 show that the mass per unit area need to be above approximately 260 kg/m^2, and the resilient layers shall have low dynamic stiffness. With respect to impact sound insulation, it should also be possible to optimise the solution and reach the same requirement level with somewhat lower mass per unit area. In the following, a more detailed analysis for the impact sound insulation.

Mass per unit area trend

In this chapter, we further analyse the effect of the mass per unit area. A trend analyses is given regarding the impact sound insulation of the six constructional floor types presented in chapter 6.1. Figures 14 to 16 include a fitting curve with the form

$$L_{n,w} + C_{I,50–2500} = a - N \times log\left(\text{mpua}\right) \tag{1}$$

where *a* and N are fitting parameters and *mpua* is the total mass per unit are in kg/m^2. In the diagrams the curve is indicated omitting the parameter a, which is not necessary for the visualisation.

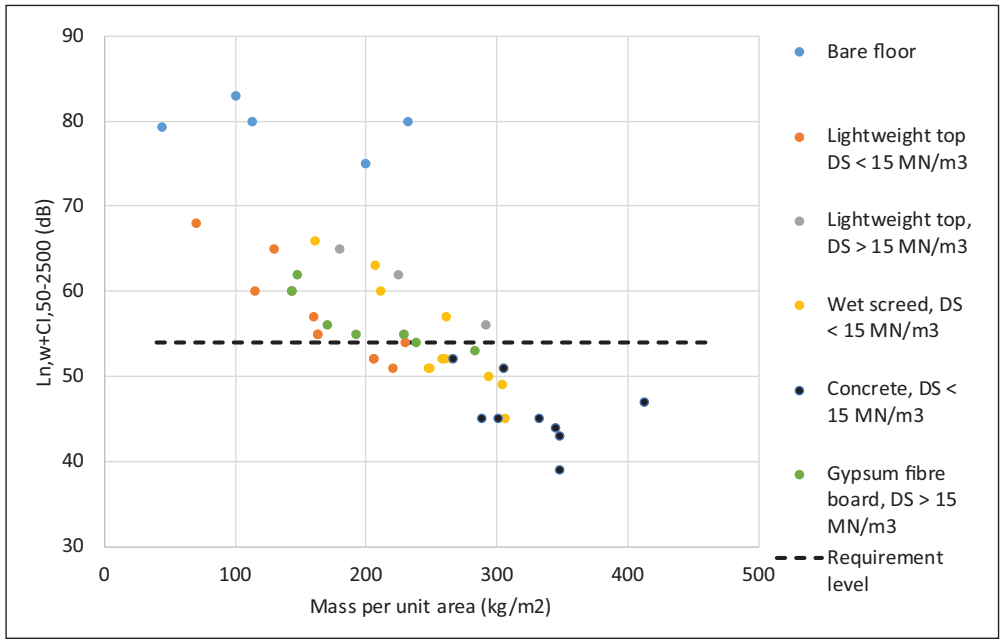

Figure 13. Single number rating, $L_{n,w} + C_{I,50-2500}$ as a function of mass per unit area. Objects from all considered categories.

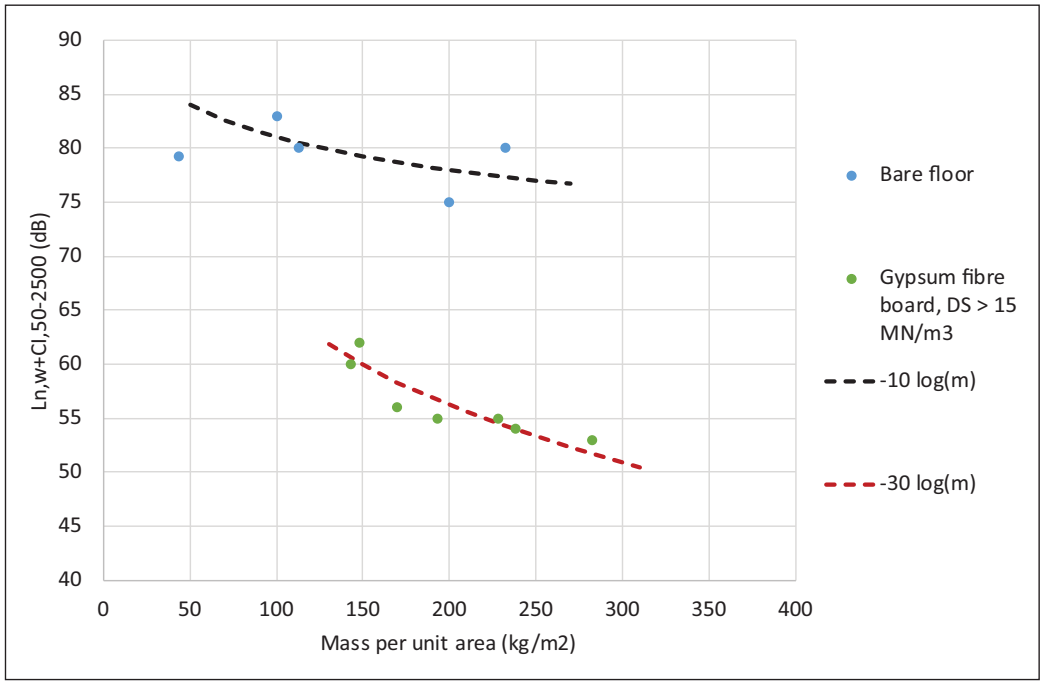

Figure 14. Single number values as a function of mass per unit area, bare floor and Gypsum fibreboard constructions.

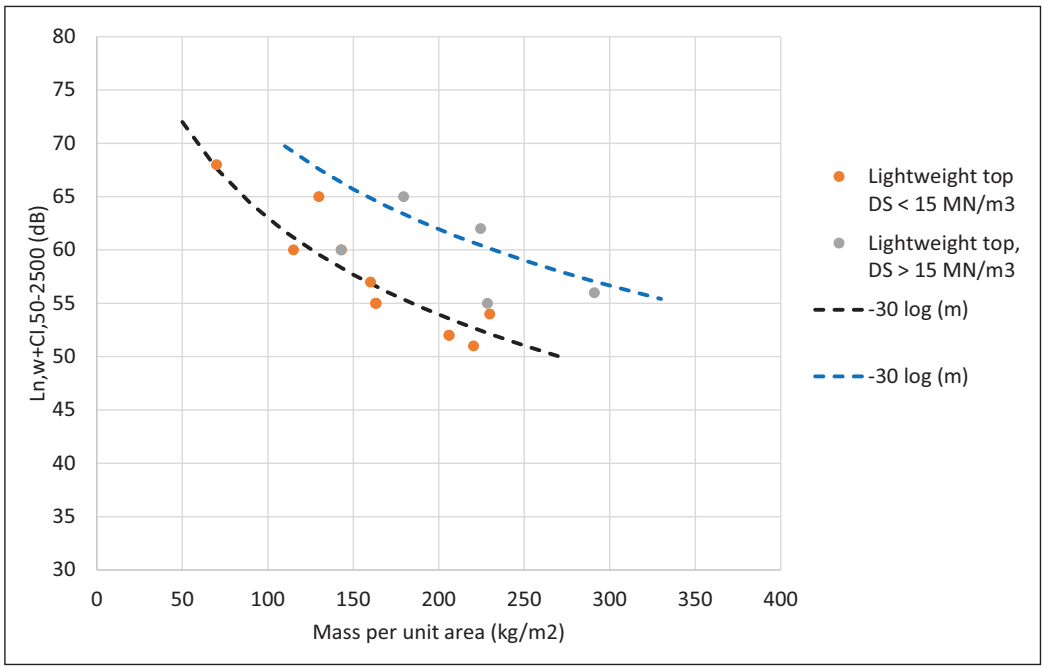

Figure 15. Single number values as a function of mass per unit area, lightweight top floor constructions.

Figure 14 shows the single number quantity as a function of the *mpua* for bare floor constructions and a resilient top floor construction including Gypsum fibre board layers. The figure includes a trend line depending on *mpua* of $N = 10$ and $N = 30$, respectively. The $N = 30$ term corresponds to the general equation of impact sound insulation of homogeneous floors.[16] For the bare floor, the data points are rather scattered and the subjective evaluated relation between the single number quantity and the *mpua* is weak. This means that the mass is not a dominant parameter for the bare floor construction, which is probably dominated by the structural stiffness and the sound radiation from the bottom surface of the element. For the floor construction with Gypsum fibre board on a resilient layer ($s' > 15\,MN/m^3$), the relation between the single number quantity and the *mpua* is relatively high with deviation between the trendline and the data points within $\pm$ 2 dB.

Figure 15 shows the single number quantity as a function of the *mpua* for lightweight floor constructions on a resilient layer (continuous elastic layer). The type of resilient layer is grouped into dynamic stiffness lower or higher than $15\,MN/m^3$. The figure includes a trend line depending on *mpua* based on equation (1). The relation between the single number quantity and the *mpua* is fairly good (within $\pm$ 2 dB) for construction with low dynamic stiffness of the resilient layer, but one outlier does not follow this trend.

The trend line for construction with dynamic stiffness above $15\,MN/m^3$ is set at a conservative level. In this case, deviating results exist, but close to results with low dynamic stiffness of the resilient layer. The reason for these results is not further analysed, but probably dominated by the accuracy of the dynamic stiffness of the involved products. This trend line must therefore be used with caution.

Figure 16 shows the single number quantity as a function of the *mpua* for hybrid floor constructions on a continuous resilient layer with $s' < 15\,MN/m^3$. The measurement objects have been divided into constructions with concrete or constructions with wet screed as floating floor. The figure includes a trend line depending on *mpua* of $N = 65$. It illustrates a significant effect of the added mass, more than the double compared with lightweight top floor constructions. The relation

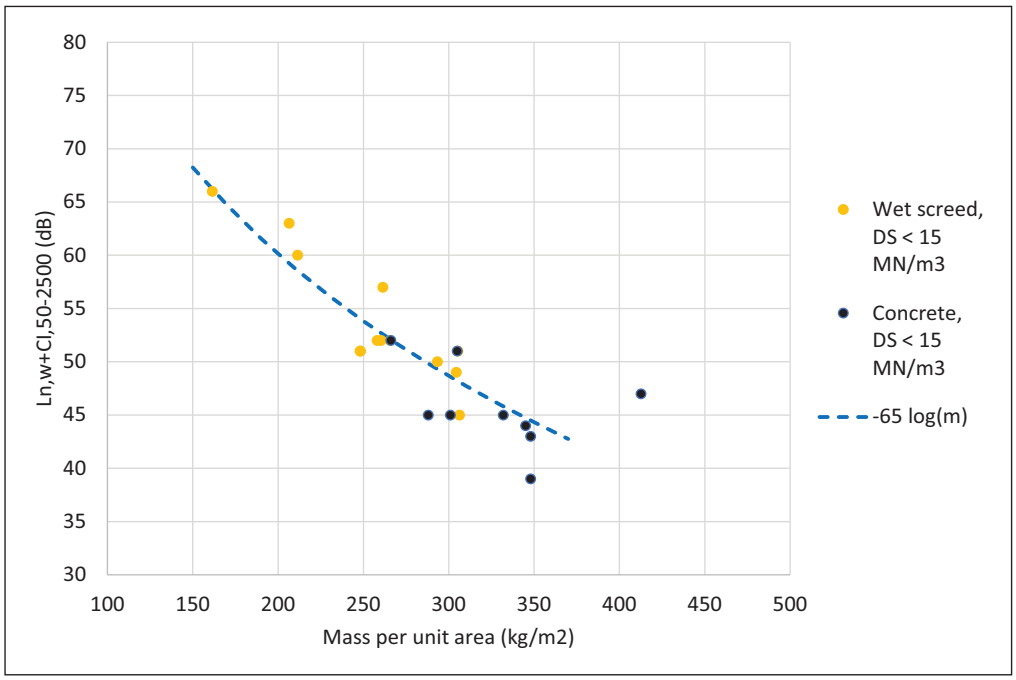

Figure 16. Single number values as a function of mass per unit area, hybrid top floor constructions.

between the single number quantity and the *mpua* is fairly good (within ± 2 dB) for 9 of 18 measurement objects. The other measurement objects show partly large deviation from this trend line, especially for the concrete floor objects. This result must therefore be used with caution.

Effect of gravel

In this section, we analyze the available data focusing on the effect of additional mass by means of gravel. Both gravel inside the wood box or gravel directly on top of the bare floor were considered here. For the six cases shown in Figure 17, data are available for the same construction with and without gravel inside the box. The figure shows the decreased single number quantity $L_{n,w} + C_{I,50\text{-}2500}$ versus increased mass from gravel. The figure also shows a trend line with improved impact sound insulation of + 6 dB per 50 kg/m^2 increased gravel mass.

Results presented in Figure 17 show a significant effect of the gravel inside the box or combined with gravel on top. A rough estimate follows the trend line, but 3 out of 12 objects deviates more than ± 2 dB. However, it is not straightforward to improve the analysis for at least the following reasons:

a) measurement results scatter due to other parameters as for example, the different cross sections and material properties,
b) the effect of the gravel inside the box must relate to the reduced sound radiation and increased damping of the bottom surface of the floor element,
c) the final measurement result depends on the impedance ratio between the separate elements, upper floor structure, elastic interlayer and basic structure. See for instance the improvement difference between the bare floor and point elastic top floor from the Woodsol objects or the effect of adding gravel on top from LI objects.[15]

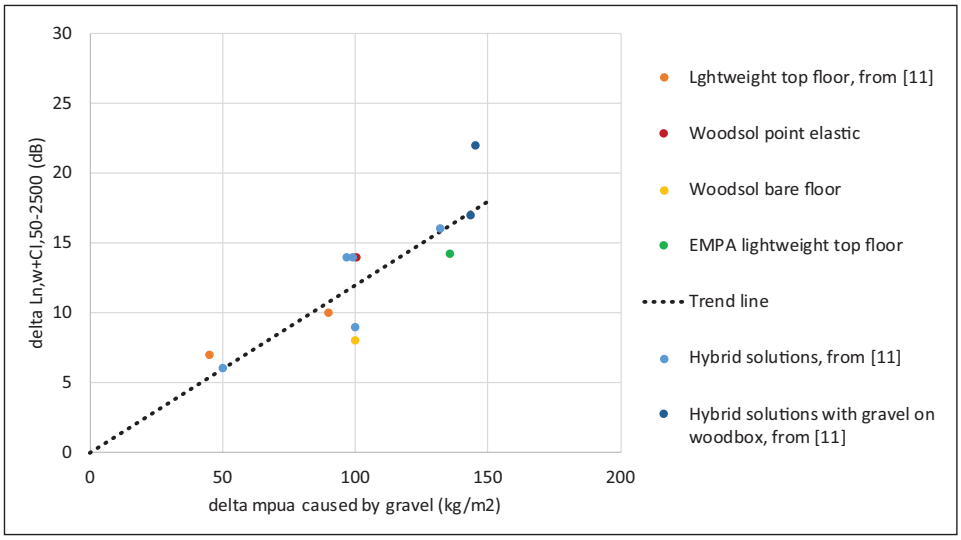

Figure 17. Improved impact sound insulation due to gravel inside the wood box.

Table 11. Sound insulation improvements from Woodsol measurements.

Elastic interlayer	Cavity fill (kg/m^2)	Δ Mass per unit area (kg/m^2)	Δ $R_w + C_{50–5000}$ (dB)	Δ $L_{n,w} + C_{I,50–2500}$ (dB)
Continuous elastic, s' > 15 MN/m^3	Gravel, 100	24	–	14
Continuous elastic, s' < 15 MN/m^3	Gravel, 100	30	14	21
Point elastic Sylodyn, NC Yellow	Gravel, 100	20	15	24
Point elastic Sylodyn, NC Yellow	–	20	18	18
Point elastic Sylodyn, NC Yellow	Wood fibre, 13	20	–	20

Effect of elastic interlayer

A significant effect from the dynamic stiffness of the continuous elastic layer is shown in Figure 15. Except one outlier, the relation between the single number quantity and the *mpua* is fairly good (within ± 2 dB) for construction with low dynamic stiffness of the resilient layer. For constructions including continuous elastic later with s' ≥ 15 MN/m^3 the impact sound level is in average approximately 8 dB higher. However, as mentioned, there are outliers closer to constructions with low dynamic stiffness. For improving the impact sound insulation of floor structures, a well-known limitation is the mass and stiffness of the basic floor structure. As seen from data in chapter 3.1, the basic floor structure varies from 44 to 232 kg/m^2 and so is the structural stiffness and span width. This means that the improvement, due to the resilient construction on top of the floor, at best will achieve numbers according to basic theory, for example[16] An alternative to continuous elastic layer for improving the impact (and airborne) sound insulation, is line elastic or point elastic constructions. Table 11 shows improvements measured in this project[17] with different elastic interlayers and different basic floor structure.

Results presented in Table 11 show a difference on the improvement of the impact sound insulation of 7 dB between continuous elastic layers with s' < 15 MN/m^3 and s' > 15 MN/m^3. This result is close to the estimate of approximately 8 dB as stated above. The results also show a more

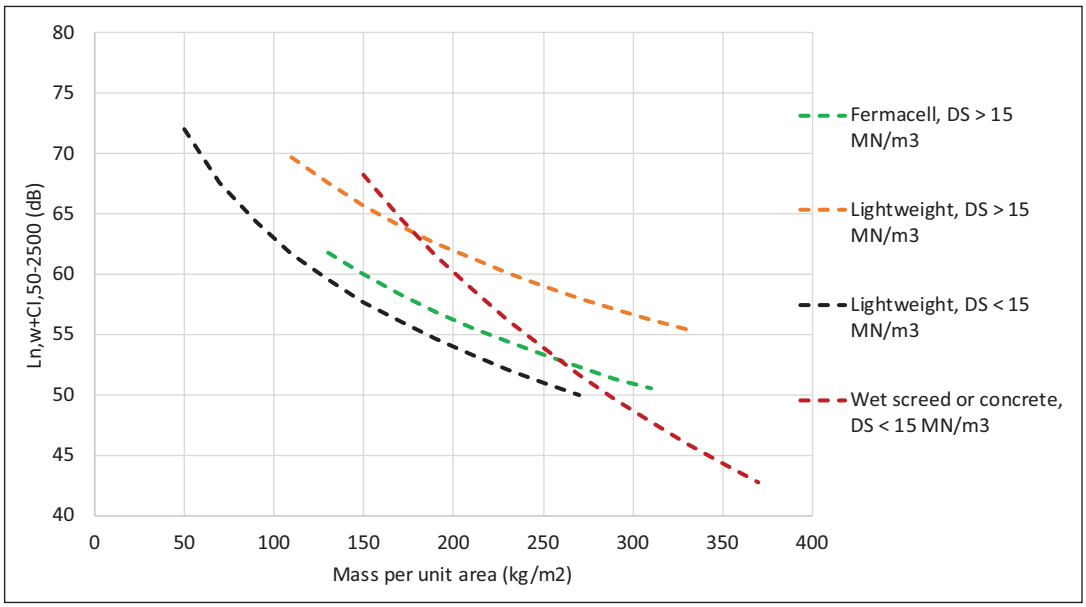

Figure 18. Improved impact sound insulation for different floating floor materials.

efficient improvement with the resilient point support construction compared to the continuous elastic layer; an additional mass of 30 kg/m^2 on a continuous layer delivers approximately the same or even less improvement then an additional mass of 20 kg/m^2 on resilient point supports. Results with Sylodyn point supports show different improvement levels depending on the basic structure, in this case different cavity filling. The improvement is 6 dB higher when the cavity is filled with 100 kg/m^2 gravel and its 2 dB higher when the cavity is dampened with wood fibre.

Global effect of identified parameters

Figure 18 shows a comparison of trend lines from Figures 14 to 16 with grouping similar to chapter 6.2. The type of floating floor material is grouped into lightweight material (dry screed, approximately 680 kg/m^3), gypsum fibreboard (e.g. Fermacell, 1150 kg/m^3) and hybrid screed materials of concrete (2300 kg/m^3) or wet screed, normally fibre reinforced (typically 1900 kg/m^3) constructions. Comparison of trend lines must be used with caution because of the large spreading of data, especially concerning hybrid top floor constructions and lightweight top floor constructions on elastic layers with high dynamic stiffness.

The trend lines are shown in Table 12 in compact form. All trend lines based on lightweight or semi-lightweight top floor construction show the same, overall tendency of −30 log (mpua). Lightweight construction with low dynamic stiffness of the elastic layer shows a trend line in the lower section of available data. To the contrary, lightweight constructions with high dynamic stiffness of the elastic layer show a trend line in upper part of available data, see Figures 15 and 18.

A trend line of approximately −65 log (mpua) is seen with wet screed or concrete materials above the elastic layer, that is, much higher compared to lightweight top floor construction, The mass per unit area needs to be at least 250 kg/m^2 before the trend line from hybrid materials perform better single number quantity than lightweight materials with low dynamic stiffness of the elastic layer. However, it must be kept in mind that the mpua is based on the *total* mass of the floor

Table 12. Overview of the identified trendlines.

Typology	Elastic layer	Trendline, impact sound insulation
Bare floor	–	$L_{n,w} + C_{I,50-2500} = 101 - 10 \cdot log\left(m'\right)$
Lightweight floating floor (dry screed)	$s' < 15\,MN/m^3$	$L_{n,w} + C_{I,50-2500} = 80 - 30 \cdot log\left(m'\right)$
Lightweight floating floor (dry screed)	$s' > 15\,MN/m^3$	$L_{n,w} + C_{I,50-2500} = 87 - 30 \cdot log\left(m'\right)$
Lightweight floating floor (gypsum fibre board)	$s' > 15\,MN/m^3$	$L_{n,w} + C_{I,50-2500} = 82 - 30 \cdot log\left(m'\right)$
Wet screed or concrete	$s' < 15\,MN/m^3$	$L_{n,w} + C_{I,50-2500} = 210 - 65 \cdot log\left(m'\right)$

element. At low mpua, the mass and stiffness of the bare floor may be low, which entirely controls the final results. This highlights that the focus should not only be on the resilient layer and top floor construction but also on the mass and stiffness of the basic structure.

Conclusion

The industrialisation of timber buildings is advancing, and the use of timber hollow-box floor is increasing. We see a need to strengthen the knowledge around the acoustic performance of timber hollow-box floors by establishing the state of the art and identifying its governing factors.

This study covered both airborne and impact sound insulation. We focused on following parameters: floor element total mass and effect of the cavity filling, element stiffness, floating floor construction and effect of the material choice and the dynamic stiffness of the resilient layer. We collected laboratory measurement results for four different objects with cross sectional height varying from 200 mm to 509 mm and total mass varying from 44 kg/m^2 to 413 kg/m^2. The data include the bare floor and its combination with both lightweight floating floors, that is, dry screed or gypsum fibre boards on resilient layer, or hybrid solutions, that is, concrete or fibre reinforced wet screed on resilient layer.

The main governing factor appeared to be the total mass per unit area of the construction. This includes both the bare floor, the cavity filling and the material choice for the floating floor. The dynamic stiffness of the resilient layer has also a major effect. As expected, low dynamic stiffness delivers better sound insulation. The performance can be further enhanced by choosing for example, resilient point support rather than a continuous layer. Depending on the floating floor material different trends for the dependency of $L_{n,w} + C_{I,50\text{-}2500}$ on the total mass were identified. Lightweight floating floor construction has similar slope, with different starting level depending on the resulting total mass of the construction and the dynamic stiffness of the resilient layer. Hybrid solutions have a steeper trend with increasing mass, but they start at unfavourable high levels. High stiffness of the bare floor proved to be favourable to achieve high $R_W + C_{50\text{-}5000}$ and low $L_{n,w} + C_{I,50\text{-}2500}$ at low frequencies. Gravel filling in the cavity has three effects; it increases the total mass of the construction, it enhances the double wall-effect by increasing the impedance of the bare floor, and it reduces sound radiation from the lower surface due to the increased damping.

The identified effects and trends establish a good understanding of the dependency of the acoustic performance of timber hollow-box floors on the investigated parameters. This knowledge can be helpful in the building design process and for the product optimisation as well as it can contribute to more efficient and sustainable buildings.

Declaration of conflicting interests

The author(s) declared no potential conflicts of interest with respect to the research, authorship, and/or publication of this article.

Funding

The author(s) disclosed receipt of the following financial support for the research, authorship, and/or publication of this article: This study has been carried out within the Woodsol project, a project funded by The Research Council of Norway lead by Kjell Arne Malo at NTNU. The project includes research at NTNU and SINTEF Community and the grant for the second author of this paper, which is gratefully acknowledged.

ORCID iD

Anders Homb https://orcid.org/0000-0001-9656-4107

References

1. Malo KA, Stamatopoulos H, Nesheim S, et al. *Requirements, lay-out and design consideration of a building system*. Woodsol: WP2 Report, Draft 110117.
2. Homb A. *Evaluering av lydegenskaper for bærende dekkekonstruksjoner*. Woodsol Notat Nr. 01/17. SINTEF Building & Infrastructure 2017 (in Norwegian).
3. Homb A and Conta S. *Lydisolering til Woodsol dekker for kontorbygg*. Woodsol Notat Nr. 02/20. SINTEF Building & Infrastructure 2020 (in Norwegian).
4. Lattke F and Lehmann S. Multi-storey residential timber construction: current development in Europe. *J Green Build* 2007; 2(1): 119–129.
5. Melián Hernández A, Geyer C, Müller A, et al. Direct and flanking airborne and impact sound insulation of different Swiss timber floor and wall constructions. In: *Proceedings of Forum Acusticum*, Krakow, 7–12 September 2014.
6. Geyer C, Müller A and Melián Hernández A. Flanking sound insulation of timber walls combined with different timber hollow box floors. In: *Proceedings of Euronoise*, Maastricht, 31 May–3 June 2015.
7. Lignum. www.lignumdata.ch. Switzerland 2015.
8. Homb A, Guigou-Carter C, Hagberg K, et al. Impact sound insulation of wooden joist constructions: collection of laboratory measurements and trend analysis. *Build Acoust* 2016; 23(2): 73–91.
9. Homb A, Guigou-Carter C and Rabold A. Impact sound insulation of cross-laminated timber/massive wood floor constructions: collection of laboratory measurements and result evaluation. *Build Acoust* 2017; 24(1): 35–52.
10. ISO 10140-2:2010. Acoustics. Laboratory measurement of sound insulation of building element. *Part 2: Measurement of airborne sound insulation*.
11. ISO 10140-3:2010. Acoustics. Laboratory measurement of sound insulation of building element. *Part 2: Measurement of impact sound insulation*.
12. EN-ISO 717-1:2013. Acoustics. Rating of sound insulation in buildings and of building elements. *Part 1: Airborne sound insulation*.
13. EN-ISO 717-2:2013. Acoustics. Rating of sound insulation in buildings and of building elements. *Part 2: Impact sound insulation*.
14. NS 8175:2012. Acoustic conditions in buildings. *Sound classification of various types of buildings*. Standard Norge 2012.
15. Ljunggren F, Simmons C and Öqvist R. Correlation between sound insulation and occupants' perception – proposal of alternative single number rating of impact sound, part II. *Appl Acoust* 2017; 123: 143–151.
16. Kumer N. *Stora Enso sound insulation measurements of timber hollow-box floor solutions*. EMPA laboratory, Switzerland. Unpublished data, April 2019.
17. SINTEF. *Sound insulation measurements on Woodsol floor elements*. Oslo 2019. Measurements published in this paper.
18. Vigran TE. *Building acoustics*. London: Taylor & Francis, 2008.
19. Conta S and Homb A. Experimental modal analysis on Woodsol timber hollow box floor element. In: *Proceedings of the 26th international congress on sound and vibration*, Montreal, Canada, 7–11 July 2019.

Paper #6

PROCEEDINGS of the
23rd International Congress on Acoustics

9 to 13 September 2019 in Aachen, Germany

Structural reverberation time measurements on WOODSOL prototype

Simone CONTA[1]; Ulrich SIMON[2]; Anders HOMB[3]

[1] NTNU, Department of Civil and Environmental Engineering, Norway

[2] Müller-BBM Acoustic Solutions GmbH, Germany

[3] SINTEF Building & Infrastructure, Norway

ABSTRACT

The WOODSOL research project aims at developing urban timber buildings based on moment resisting frames. One of the key aspects when dealing with the sound insulation in the building system is the flanking sound transmission across the floor elements and through the special connecting elements of the floor to the columns. We build a system prototype to be able to investigate experimentally the vibroacoustic behavior of the floor elements and the vibration transmission to the columns considering in particular impact excitation. In this paper, we focus on the structural reverberation time, which is a key parameter to determine calculation quantities such as e.g. K_{ij} required by the ISO12354. The K_{ij}-index is necessary to estimate flanking sound transmission and therefore a key input to SEA based calculation models. We present the measurement setup used at the Woodsol prototype. We present the measurement procedure designed following the ISO 10848-1 and discuss the measurement program, excitation type and sensor placement. We present the challenges we encountered and discuss the obtained result with particular focus on the comparison of impact hammer excitation and shaker excitation with swept sine.

Keywords: timber, reverberation, measurements

1. INTRODUCTION

As part of the research work within the WOODSOL project, we are investigating experimentally the vibroacoustic behavior of the WOODSOL floor element and the special moment resisting connection between the floor elements and the load bearing columns.

The experimental activities shall deliver the impact noise level for the floor element and an evaluation of the flanking transmission both in vertical and horizontal direction. Both aspects are to be studied considering the principle of the ISO12354 (1). Herein, a key parameter that needs to be investigated is the structural reverberation time. The reference standard for the structural reverberation time is the ISO10848-1 (2). Although the standard refers for the signal processing to the ISO3382 (3), the measurement of the structural reverberation time is more challenging than the room reverberation time. Moreover the standard was mainly developed looking at heavy homogeneous monolithic walls such as masonry or concrete walls (2, 4) and there have been discussions regarding the challenges related to applying the standard to lightweight walls (5) and to inhomogeneous objects (6, 7).

In our specific case, we are dealing with a strongly inhomogeneous lightweight structure, with low damping at low frequencies and highly damped above approximately 60 Hz (8). This calls for a critical approach to the measurement setup and the measurement procedure. In the following we describe our approach, the challenges we encountered and draft some preliminary conclusions.

2. TEST OBJECT

The measurements were performed on the WOODSOL prototype, shown in Figure 1. The prototype consists of two floor elements, mounted on six columns. At each corner of the floor element, one

[1] Simone.Conta@ntnu.no
[2] Ulrich.Simon@mbbm-aso.com
[3] Anders.Homb@sintef.no

WOODSOL connector is used to establish a moment resisting connection between the floor itself and the column. The current version of the connector is shown in Figure 3 along with a schematic of the principle. It is based on metal brackets connected by friction bolts. The brackets are mounted to the timber by means of threaded metal rods (9).

The material for the columns is glulam and they have dimensions of 400 mm x 450 mm x 5200 mm. Their size is given by the structural and fire safety requirement for an eight to ten story building, which is the target building of the WOODSOL project. The floor is mounted with the bottom flange at 2 m above the floor of the lab.

The floor element has dimensions of 4.7 m x 2.4 m x 0.5 m and is of type hollow box. The cross section is shown in Figure 2 and is designed for a 9 m to 10 m span. The top and bottom plates are KERTO-Q plates with thickness of 43 mm and 61 mm respectively. The thickness of the bottom flange was designed to fulfill fire safety requirements when the floor is installed without additional ceiling. The outermost stringers are glulam GL30c, while the inner ones are glulam GL28c (10). The total weight of the floor element is 2.6 tons including the filling of gravel.

Figure 1 – Woodsol prototype installed at Charlottenlund Videregående Skole, Trondheim (Norway)

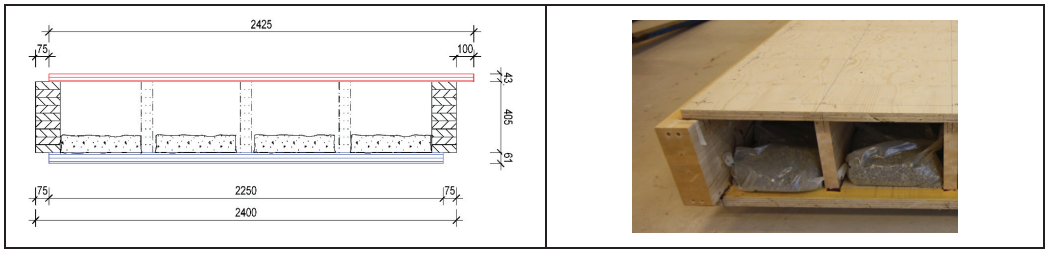

Figure 2 – Floor element cross section (left) and picture showing the gravel bags positioned in the element cavity (right).

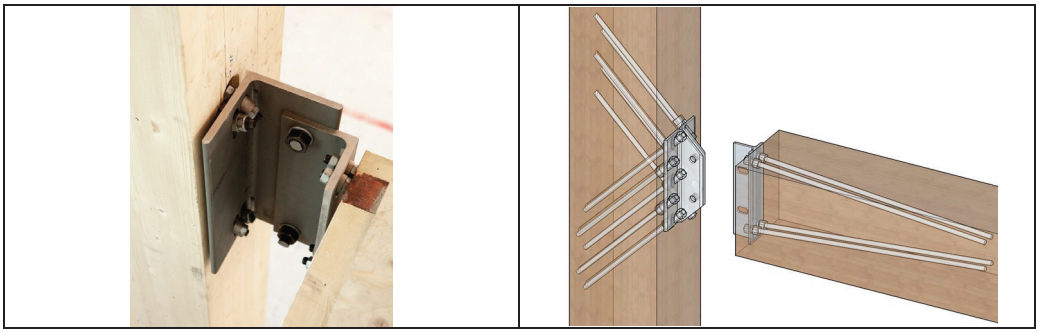

Figure 3 – Picture of the connector installed between the floor element and the column (left) and principle of the connector showing the threaded rods (right).

3. MEASUREMENT SETUP AND ANALYSIS PROCEDURE

3.1 General

The ISO10848 suggests as preferred method to measure the structural reverberation time the one that uses an electrodynamic shaker with an MLS or swept sine signal (2). This method seems to be less prone to excite nonlinearities (11-13), but is more complicated and time consuming compared to the very straightforward excitation with an impact hammer. The ISO10848 also does not exclude the impact excitation provided that the linearity of the system is checked. Other works on timber lightweight structure suggest that impact excitation might provide linear excitation on these type of structures (7). Moreover Hopkins in (14) suggest that it might be more appropriate to use hammer excitation when focusing on impact noise level, since this is usually measured using the ISO standard tapping machine. Considering these different arguments we decided to use both impact and shaker excitation in our investigations. In the measurement program we included preliminary measurements of transfer functions to compare impact with shaker excitation as suggested in the ISO10848 and observe their dependency on the amplitude of the excitation. During these preliminary measurements, we also verified the effect of the sweep length. The test setup for these preliminary measurements is shown in Figure 4.

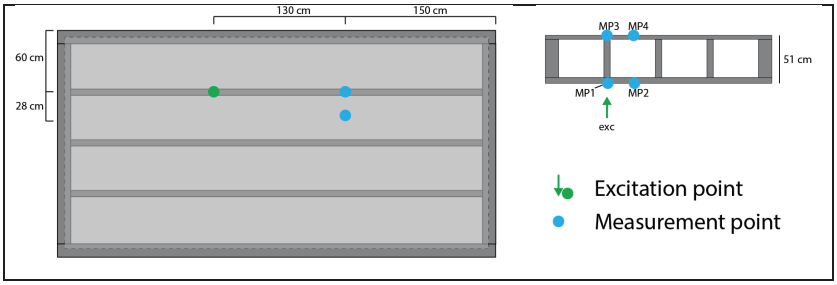

Figure 4 - Test setup for the preliminary measurements

3.2 Measurement program

The measurement program included: a) preliminary measurements: shaker excitation with varying amplitude, shaker excitation with varying sweep length, impact excitation with varying amplitude; b) measurements with impact excitation both on top and bottom of the element with sensors placed on both sides; c) measurements with shaker excitation both on top and bottom of the element with sensors placed on both sides.

3.3 Excitation

We used a B&K impact hammer type 8208 with medium tip (green) for the impact excitation.

The shaker used was a B&K 4808 with approx. 20 kg additional mass. We mounted the shaker on a separate structure by means of metal springs and connected to the excitation point by means of a stinger. Between the stinger and the excitation point we inserted an impedance head to measure force and vibration. The impedance head was fixed to a timber screw inserted in the Kerto plate. The driving signal was a linear sweep from 20 Hz to 1250 Hz. Three different sweep lengths were tested during the preliminary measurements: 12.5 s, 25 s, and 50 s and no differences were observed in the obtained transfer functions. For all further measurements the sweep length was set to 25 s.

Four excitation positions were used on the bottom flange both with shaker and impact excitation. Three excitation position were also placed on the top flange, but used only for the impact excitation.

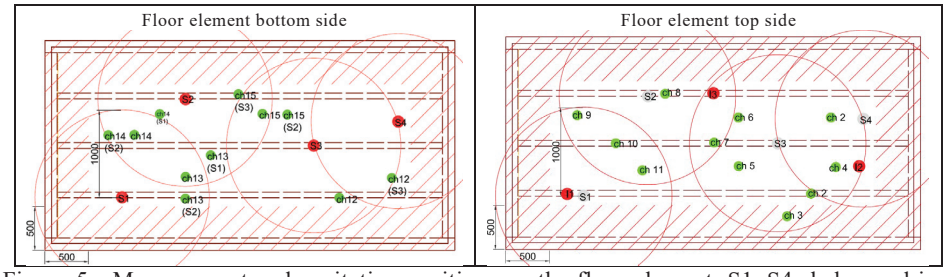

Figure 5 - Measurement and excitation positions on the floor element: S1..S4 shaker and impact positions (only bottom side); I1… I3 impact positions (only top side); ch2… ch15 accelerometer positions; the red hatch and circles mark the ISO requirement on minimum distance from the object boundaries and between source and measurement position.

3.4 Response acquisition

The acceleration was recorded with a multichannel signal analyzer at 10 positions on the top flange of the floor element and 4 on the bottom flange using accelerometers as shown in Figure 5. This corresponds to a total of 56 measurement position for shaker excitation and 98 measurement positions for impact excitation. This largely exceed the requirement from the standard (9 measurement positions). Thick washers were mounted by means of timber screw to the Kerto plates and the accelerometers were applied on the washers by magnetic mounting.

3.5 Impulse response analysis

The measurement with impact excitation delivers directly the impulse response of the system. The transfer function was calculated dividing the acceleration spectrum by the force spectrum.

When using the shaker excitation, the impulse response of the system was calculated from the transfer function in the frequency domain using the inverse fourier transformation. To calculate the transfer function we used the acceleration signal from the accelerometer and the force signal from the impedance head. In this way, we could exclude the effects of the amplifier, the shaker and the stinger.

The impulse responses were processed using the commercial software m|reverb (Müller-BBM GmbH). The software fullfills the requirements of ISO3382 and was mainly designed for room acoustic purposes. We highlight following steps of the processing of the impulse response: 1) the first step in the procedure is the filtering of the impulse responses. The 1/3 octave filters are implemented as reverse filters. They have a shorter inherent reverberation time and allow for analyses of shorter times. The lower limit is given by $BT > 4$, where B is the bandwidth of the filter and T the reverberation time at the frequency of interest (2). 2) The filtered and squared impulse responses are then backwards integrated to compute the Schroeder plots. 3) On the basis of the Schroeder plot the reverberation times are calculated by fitting a regression line and calculating the energy decay over a specific range. Different options were available here: T5 (-5 dB to -10 dB), T10 (-5 dB to -15 dB) and T20 (-5 dB to -25 dB). The reverberation times are calculated for each measurement positions and the aritmetically averaged. When averaging, the reverberation times shorter than $T < 4/B * 0.8$ were excluded. The arbitrary choice of “softening” the $BT > 4$ criteria was made considering the very low reverberation time measured and the discussions presented in (14) and in (7).

4. MEASUREMENT RESULTS AND DISCUSSION

4.1 Linearity of the excitation

During the preliminary measurements, the amplitude of the excitation was varied in three steps denominated “strong”, “normal” and “soft” both for impact and shaker excitation. The results are shown in Figure 6. The left part of the diagram shows the results for impact excitation and the right part for shaker excitation. On both sides, the top diagram shows the force spectrum. The two lower diagrams show the transfer functions recorded at two different measurement positions (MP). MP1 was on the bottom plate of the floor element, in correspondence of a joist. MP2 was on the bottom plate as well, but in between two joists.

The results show a strong dependency of the transfer function amplitude on the excitation amplitude for the impact excitation. Surprisingly two different trends are observed below 80 Hz..100Hz and above: below this frequency the amplitude of the transfer function decreases with increasing amplitude of the excitation. Above this frequency the trend is inverted. The effect is more pronounced for the measurement point between the joists. In the case of shaker excitation the amplitude of the transfer function remains constant changing the amplitude of the excitation. Similar behavior was observed by other authors, e.g. (13) and might be an indication of nonlinearities.

General differences are observed between the transfer functions recorded with impact excitation and shaker excitation, in particular above 100 Hz, but clearly evident also between 50 Hz and 100 Hz. A possible reason is the slightly different excitation position between the shaker position – fixed by a screw – and the hammer hits, which impact a few centimeters (ca. 5 cm) next to it. We assume an effect from this on the differences between the excitation methods. A further explanation could be a more dominant reverberant field with impact excitation compared to shaker excitation.

Both aspects described above need further investigations for better clarification.

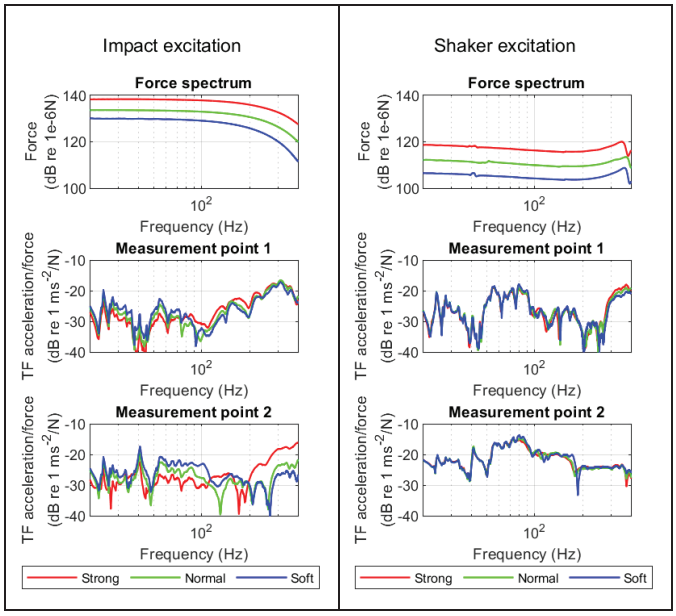

Figure 6 - Results from the preliminary measurements to determine linearity of the system; Left: impact excitation; Right: shaker excitation

4.2 Schroeder plots

Figure 7 shows the Schroeder plots obtained for all channels on the top flange of the floor element by shaker excitation on the bottom side, for the 1/3 octave bands 100 Hz, 250 Hz and 500 Hz. They are representative for all results obtained and show following features: a) there is a strong variability

between measurement points. The variability has a maximum at about 250 Hz; b) the decay range with a linear trend is between -4 dB… -5 dB and -10 dB. At -10 dB some of the curves already deviate strongly from a linear decay; c) the number of points in the curves decreases with the frequency due to the increase of the wavelength and makes the fitting process at low frequencies over short decay ranges particularly challenging.

Based on the evaluation of the Schroeder plots, we decided to use T5 (reverberation time calculated on the decay between -5dB and -10dB) for the further analysis.

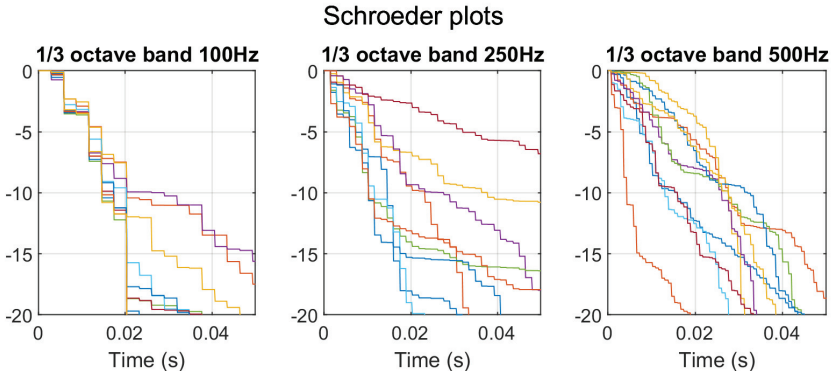

Figure 7 - Schroder plot for one of the shaker measurements. Displayed are several accelerometer positions and three 1/3 octave bands.

4.3 Excitation and response position

In Figure 8, we show the average reverberation times (T5) obtained for different excitation and receiver positions. The different combinations are shown in Table 1, where we also indicate which excitation type was used. These results investigate the variability of the reverberation time based on the spatial choice of the excitation and the receiver positions.

Table 1 – Combinations of excitation and receiver position

	Receiver: top	Receiver: bottom
Excitation: top	impact	impact
Excitation: bottom	shaker, impact	shaker, impact

The results obtained show a clear dependency between the reverberation time and the excitation / receiver locations. Similar results are obtained for both shaker and impact excitation. Shorter reverberation times are recorded on the highly damped bottom flange of the element, which is covered with gravel. Longer reverberation times are recorded on the top flange, which is not damped by the gravel. The longest reverberation time is recorded when both excitation and response are on the top flange. It should be pointed out that the evaluation of the reverberation times from acceleration on the bottom plate was particularly challenging due to the very short reverberation times, falling often below the lower limit (BT>4). For this reason the respective line in the diagram with the data from impact excitation is dotted and the line in the diagram with the data from shaker excitation is not continuous.

The standard deviation is not shown in these diagrams for practical reasons. Nevertheless it should be noted that the order of magnitude of the standard deviation is similar to the one shown in Figure 9.

4.4 Floor element reverberation time

In Figure 9, we show the reverberation time (T5) calculated as an average over all available measurement positions. To make the results comparable, for the impact excitation only the bottom excitation positions are considered.

The recorded reverberation times are very short above 100 Hz quicly decreasing from about 0.3 s at 100 Hz to less than 0.1 s at about 800 Hz. Below 100 Hz the dynamic of the undamped modes dominates the reverberation time that becomes much longer exceeding 1 s at 50 Hz. This trend meet

the expectations from the experimental modal analysis previously performed on the same setup (8).

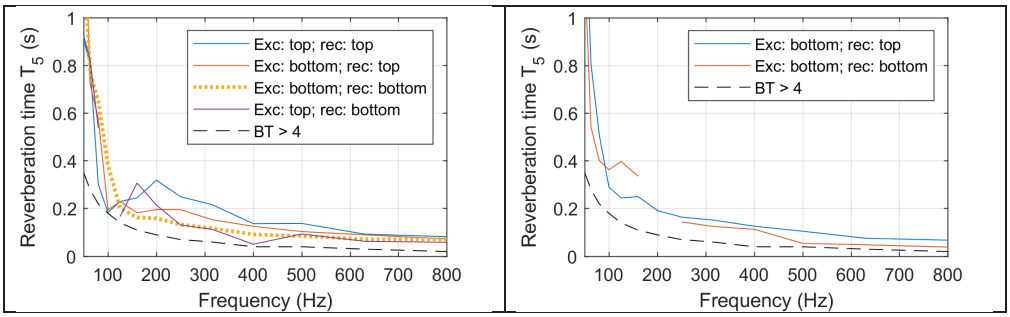

Figure 8 - Reverberation times obtained with impact (left) and shaker (right) excitation for different combinations of excitation (Exc) and sensor position (rec).

Impact and shaker excitation deliver results that are comparable and well within one standard deviation. This confirms the thesis from (6) that both methods are suitable for measurements on lightweight structures. The trend that impact excitation would deliver higher reverberation times than shaker observed by other authors (11, 13) on heavier structures was not observed here.

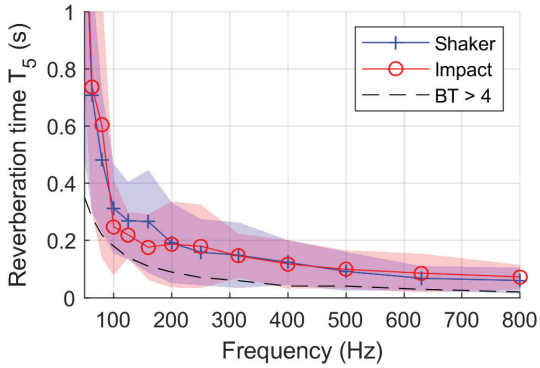

Figure 9 Reverberation time (T5) measured with impact excitation and shaker excitation. The average over all available receiver positions for bottom excitation is shown along with the standard deviation.

5. CONCLUSION

We performed reverberation times measurements on a strongly inhomogeneous lightweight structure, built with several different orthotropic materials. We followed the procedures suggested be the ISO10848-1 and encountered several challenges, which we highlight below: a) the spreading of the measurement results is high and b) a dependency of the results on both the excitation and sensors position was observed. Higher reverberation times were recorded on the upper lightly damped part of the structure and lower reverberation times were recorded on the lower highly damped flange. This raises the question of which position should be considered and if the in the standard suggested minimum 9 positions are enough for this kind of structures. c) The analysis of the data with commercial room acoustic software turned out to be very challenging, requiring enhance features (T5) evaluate very short linear decays. More flexibility (e.g. regression line starting at -3dB, evaluation range -3 dB to -8 dB as suggested in (4)) in the analysis would have been an advantage but makes the results rather used dependent. The evaluation at low frequencies was particularly difficult, since very few points are available to fit the regression line for the evaluation of the reverberation time from the Schroeder plot. d) Shaker and impact excitation delivered comparable results. Impact excitation had the clear advantage of being faster and more flexible but the frequency range is of course limited. e) The results found were nevertheless in agreement with the findings of other authors and the expectations from a previously performed experimental analysis. f) We observed differences in the

measured transfer function between shaker and impact excitation that are not fully understood yet. Further investigations are needed here.

ACKNOWLEDGEMENTS

This project has been carried out within the Woodsol project (http://www.Woodsol.no), which is funded by the Norwegian Research Council. The colleagues at NTNU S. Nesheim and A. Vilguts were involved in the design and construction of the WOODSOL prototype and L. J. Lassesen supported us during the construction of the prototype at Charlottenlund videregaende skole in Trondheim (NO).

REFERENCES

1. ISO12354-1:2017. Building acoustics -- Estimation of acoustic performance of buildings from the performance of elements -- Part 1: Airborne sound insulation between rooms.

2. ISO10848-1:2017. Acoustics - Laboratory and field measurement of flanking transmission for airborne, impact and building service equipment sound between adjoining rooms Part 1: Frame document.

3. ISO3382-1:2009. Acoustics -- Measurement of room acoustic parameters -- Part 1: Performance spaces.

4. Hopkins C, Robinson M. On the Evaluation of Decay Curves to Determine Structural Reverberation Times for Building Elements. Acta Acustica united with Acustica. 2013;99(2):226-44.

5. Mecking S, Völtl R, Winter C, M B, Schanda U, Müller G, editors. Methodenvergleich zur Bestimmung von Verlustfaktoren von Massivholzelementen. DEGA eV (ed), Fortschritte der Akustik - DAGA; 2014.

6. Mecking S, Mayr AR, Schanda UJPoD, Darmstadt. Messung von Körperschall-Nachhallzeiten inhomogener Strukturen am Beispiel einer Holzbalkendecke. 2012.

7. Mecking S. Messung von Körperschall - Nachhallzeiten an Holzbalkendecken. Rosenheim: Hochschule Rosenheim; 2012.

8. Conta S, Homb A. Experimental modal analysis on Woodsol hollow box floor elements. Accepted for 26th International Congress on Sound and Vibration, ICSV26, 7-11 July 2019, Montreal, Canada. 2019.

9. Vilguts A, Malo KA, Stamatopoulos H. MOMENT RESISTING FRAMES AND CONNECTIONS USING THREADED RODS IN BEAM–TO-COLUMN TIMBER JOINTS.

10. Halstedt H. Woodsol prototype element production drawings. SINTEF Byggforsk, Trondheim, NO; 2018.

11. Meier A. Die Bedeutung des Verlusfaktors bei der Bestimmung der Schalldämmung im Prüfstand. Aachen: RWTH Aachen; 2000.

12. Murta B, Höller C, Sabourin I, Zeitler BJS. MEASUREMENT OF STRUCTURAL REVERBERATION TIMES FOR CALCULATION OF ASTC IN UPCOMING NBCC.1:2.

13. Bietz H, Stange-Kölling S, Schmelzer M, Wittstock V. Loss factor measurement and indications for nonlinearities in sound insulation. 2019;26(1):21-34.

14. Hopkins C. Sound Insulation: Elsevier / Butterworth-Heinemann; 2007.

ISBN 978-82-326-5076-7 (printed ver.)
ISBN 978-82-326-5077-4 (electronic ver.)
ISSN 1503-8181

NTNU

Norwegian University of
Science and Technology